Design of nanostructured bulk steels

J. Millan, D. Ponge, L. Yuan, S. Sandlöbes, S. Goto, Y. Li, P. Choi, S. Zaefferer, A. Nematollahi, M. Herbig, R. Kirchheim, J. Neugebauer, D. Raabe

Max-Planck-Institut für Eisenforschung GmbH
Düsseldorf, Germany
WWW.MPIE.DE
d.raabe@mpie.de

shortened version

Max-Planck Institut für Eisenforschung GmbH, Düsseldorf

Foundation: 1917 as Kaiser-Wilhelm-Institut für Eisenforschung

Since 1971: Basic corporate budget financed by Max-Planck-Society (50%) and VDEh (50%)

Total budget 2012: 19 Mio Euros
(41% MPG, 38% VDEh, 21% third party funds)

Personnel: 250

100 years public-private partnership

MPIE structure and departments

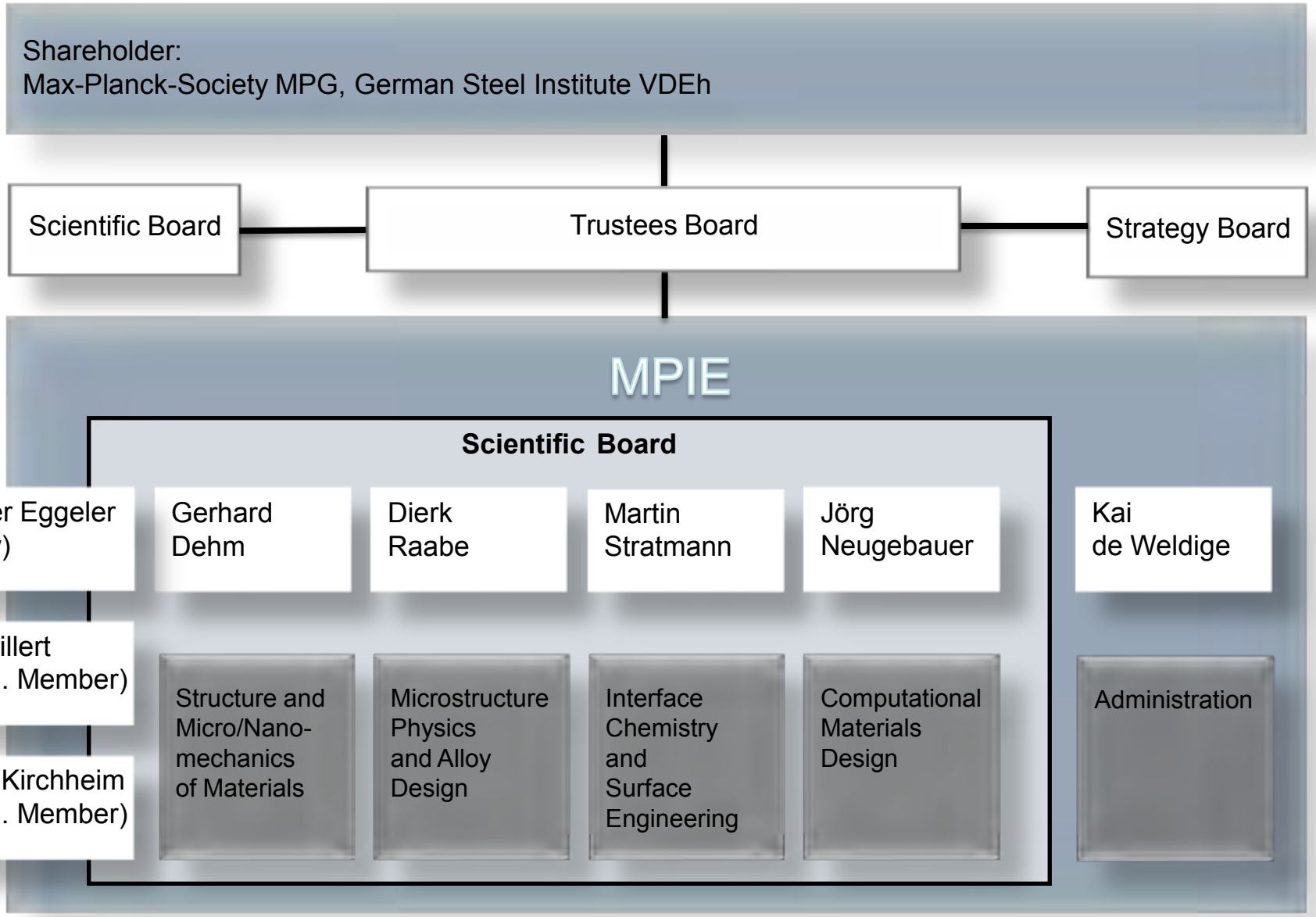

MPIE research focus: areas of high expertise

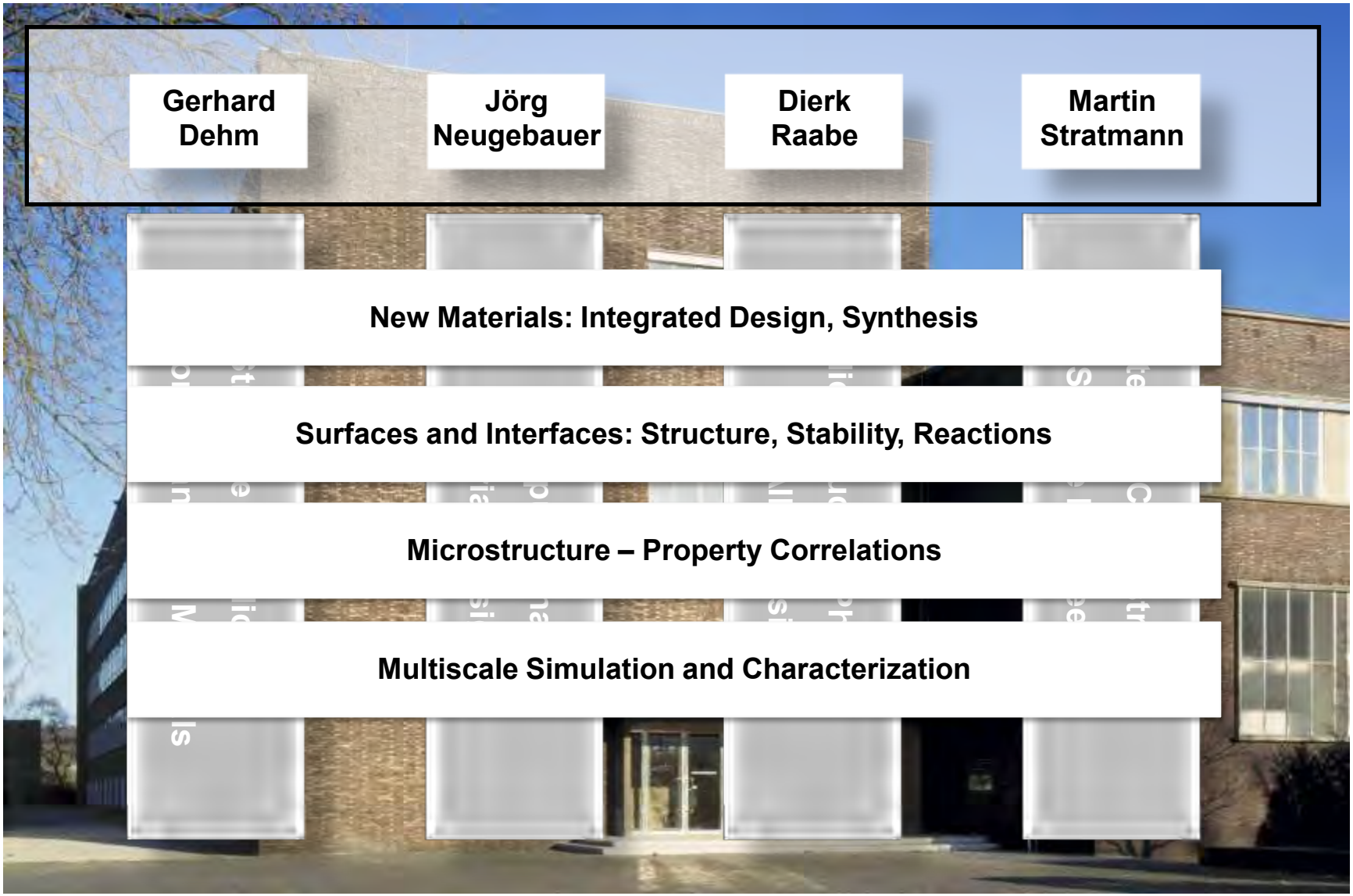

MPIE research focus: areas of high expertise

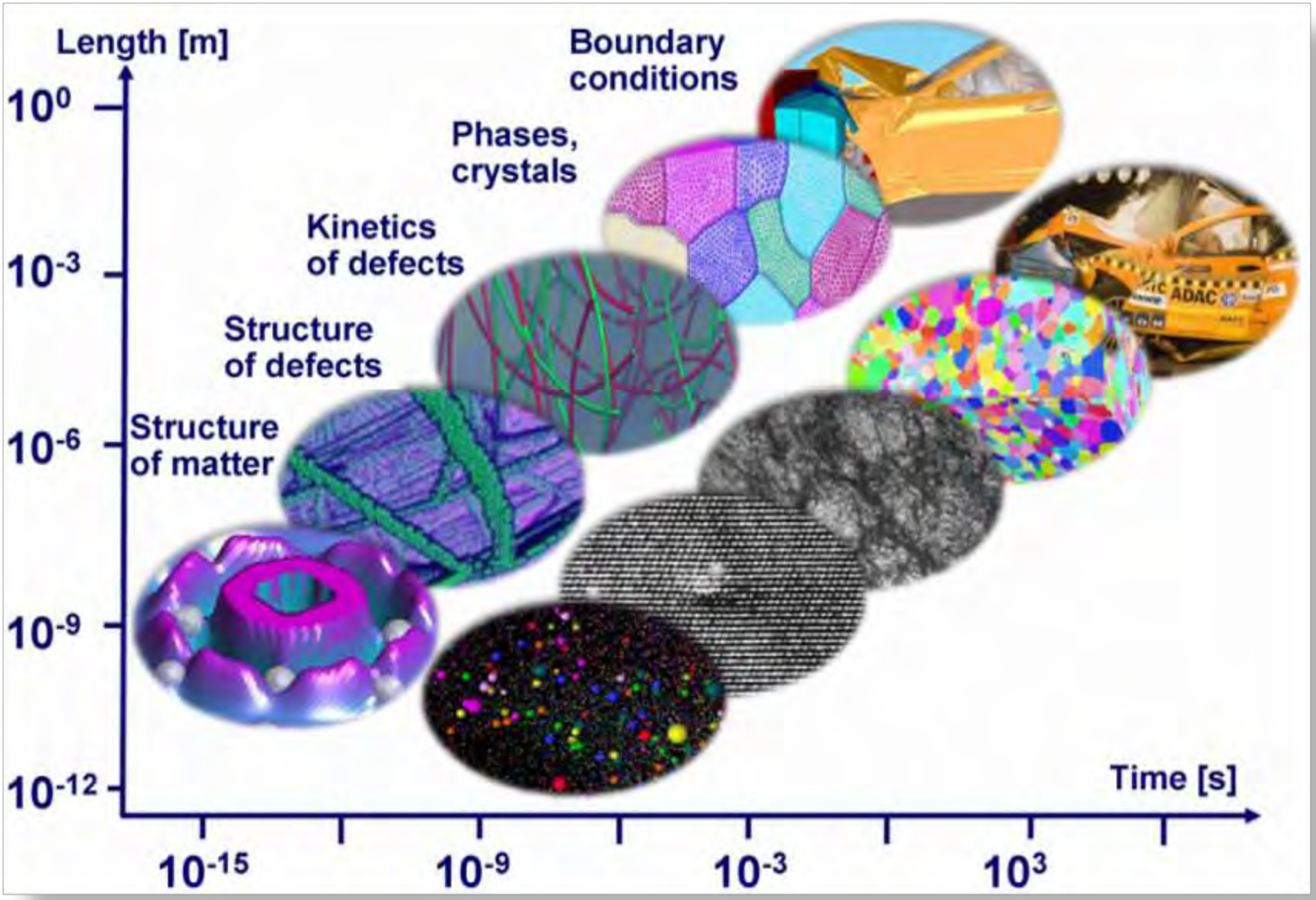

Answering societies' grand challenges with complex alloys

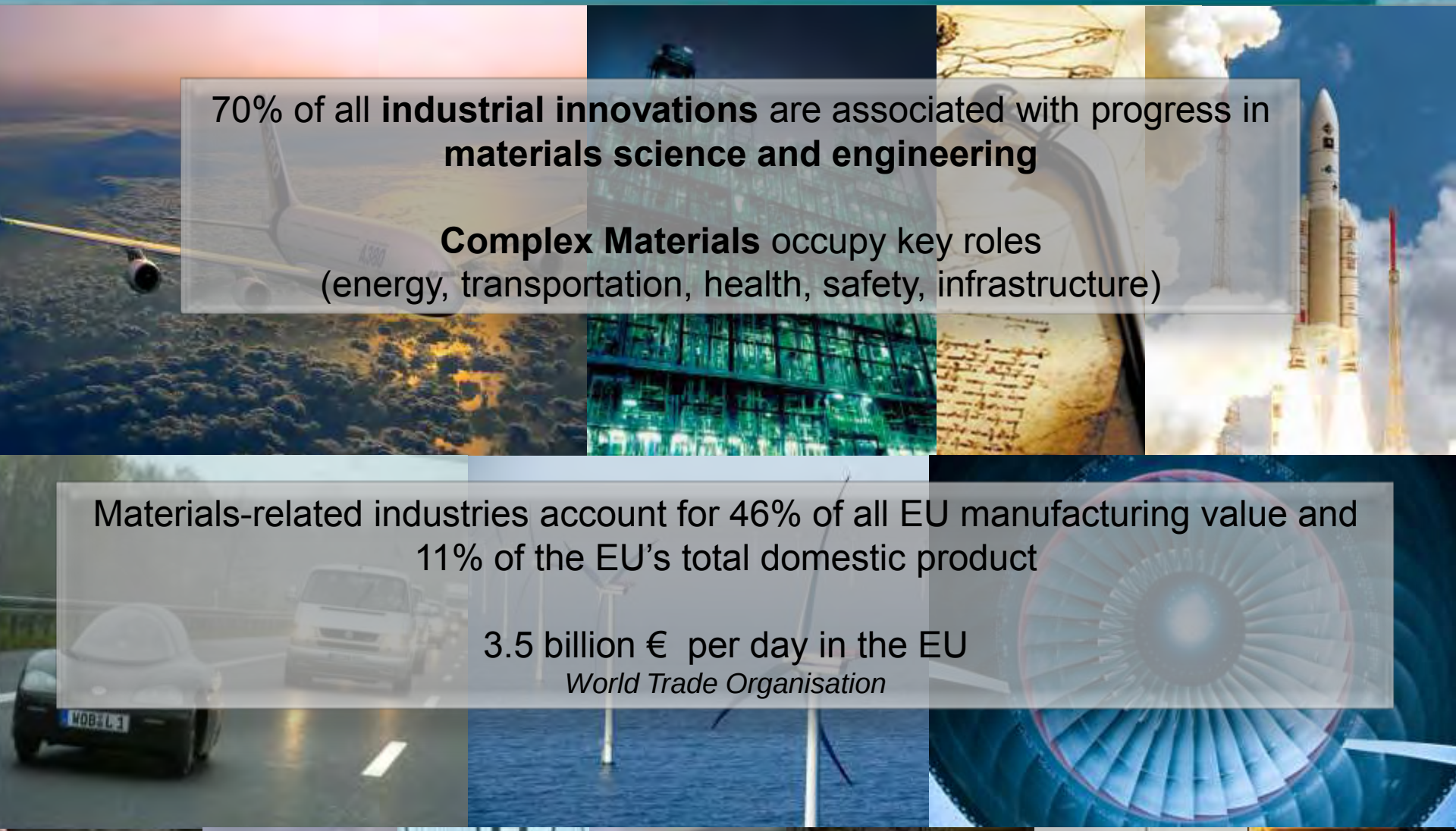

70% of all **industrial innovations** are associated with progress in **materials science and engineering**

Complex Materials occupy key roles
(energy, transportation, health, safety, infrastructure)

Materials-related industries account for 46% of all EU manufacturing value and 11% of the EU's total domestic product

3.5 billion € per day in the EU
World Trade Organisation

Local phase transformations enable high strength of bulk metals

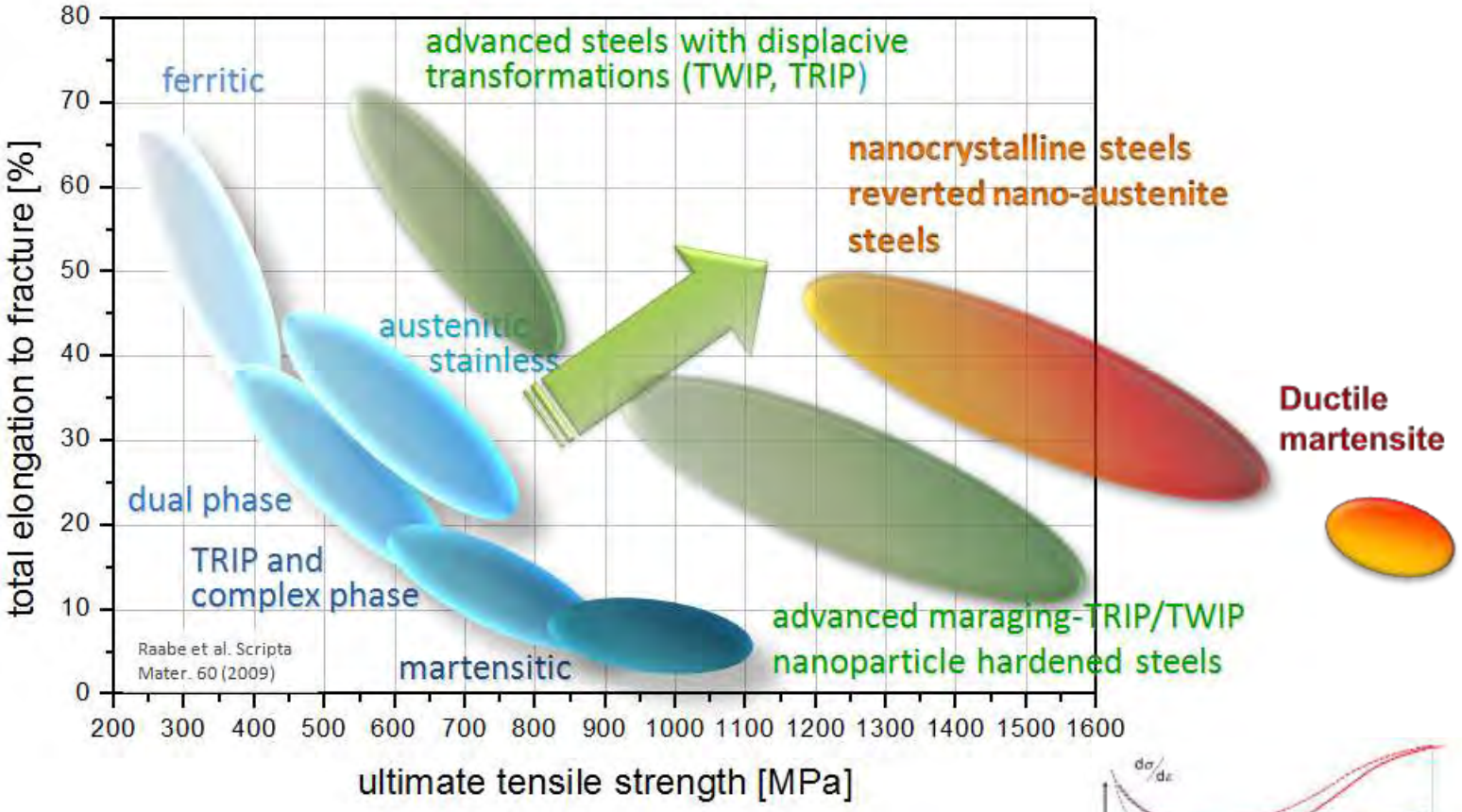

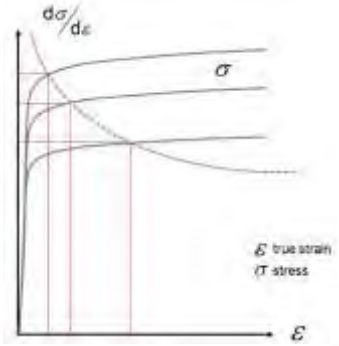

Inverse strength-ductility relation

Design strain hardening only where needed

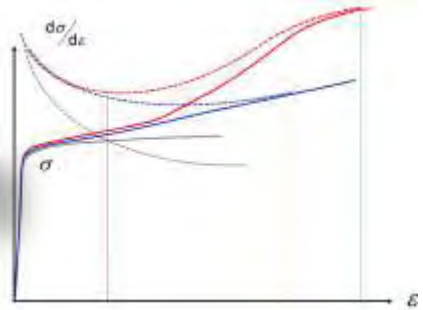

Understanding the nanoscopic length scales and their effects

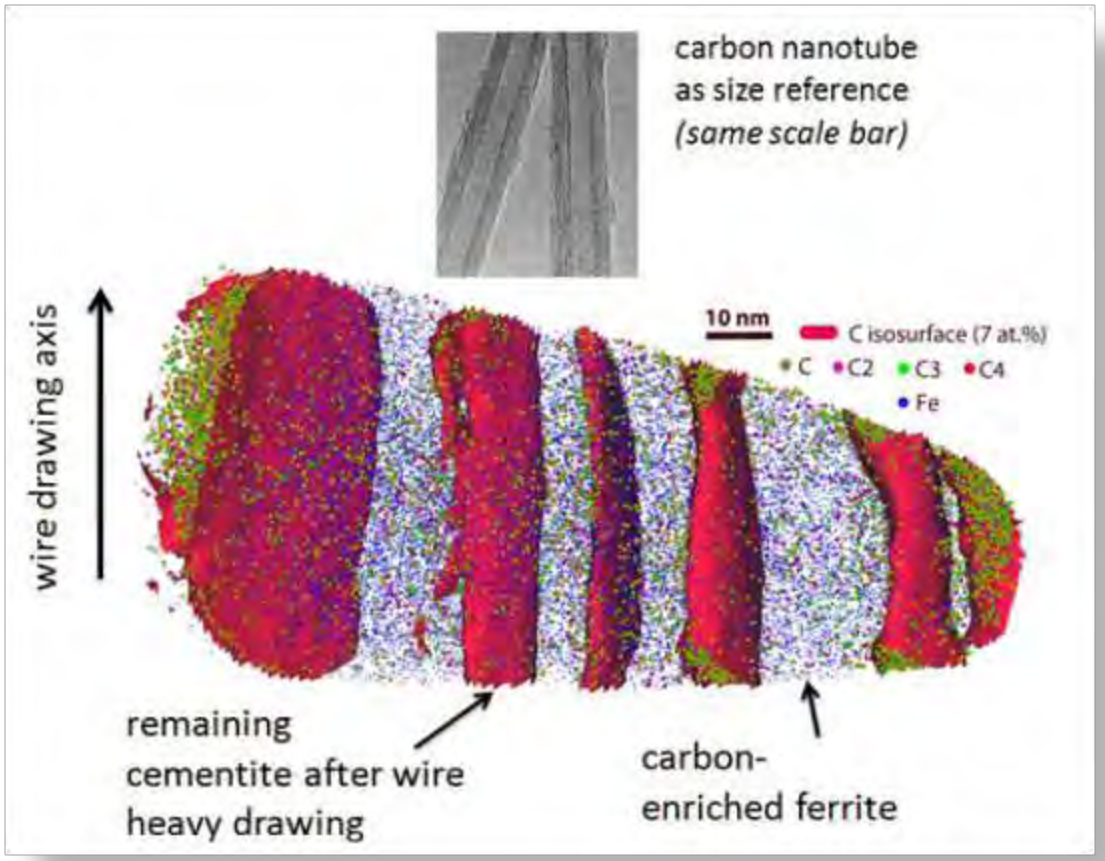

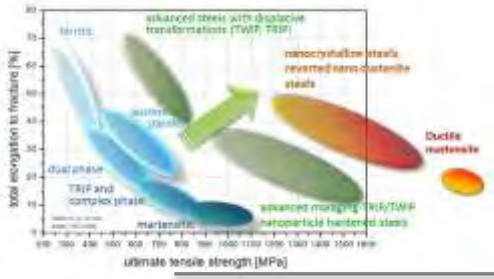

Nano-
pearlite

> 6 GPa

Atom probe tomography – principle

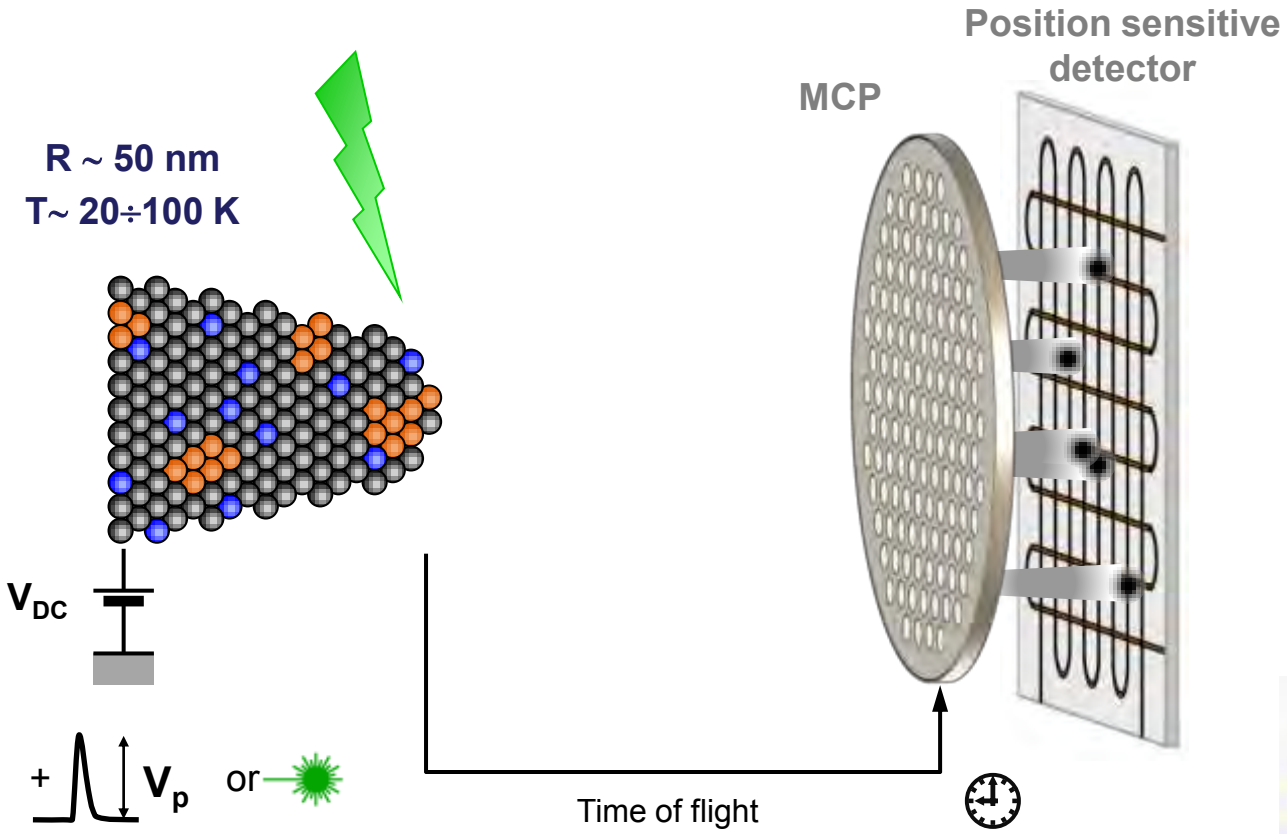

Ion sequence:

X_1, Y_1, ToF_1

X_2, Y_2, ToF_2

X_3, Y_3, ToF_3

X_4, Y_4, ToF_4

X_5, Y_5, ToF_5

……..

Position of the hit	→	X-Y coordinates
Evaporation sequence	→	Z coordinate
Time of flight	→	chemical identity

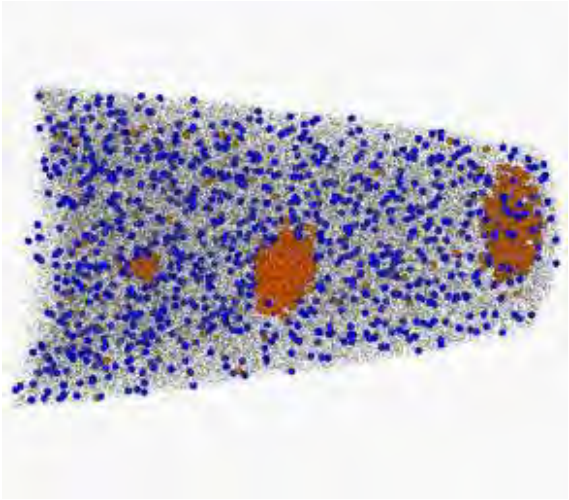

Field desorption image

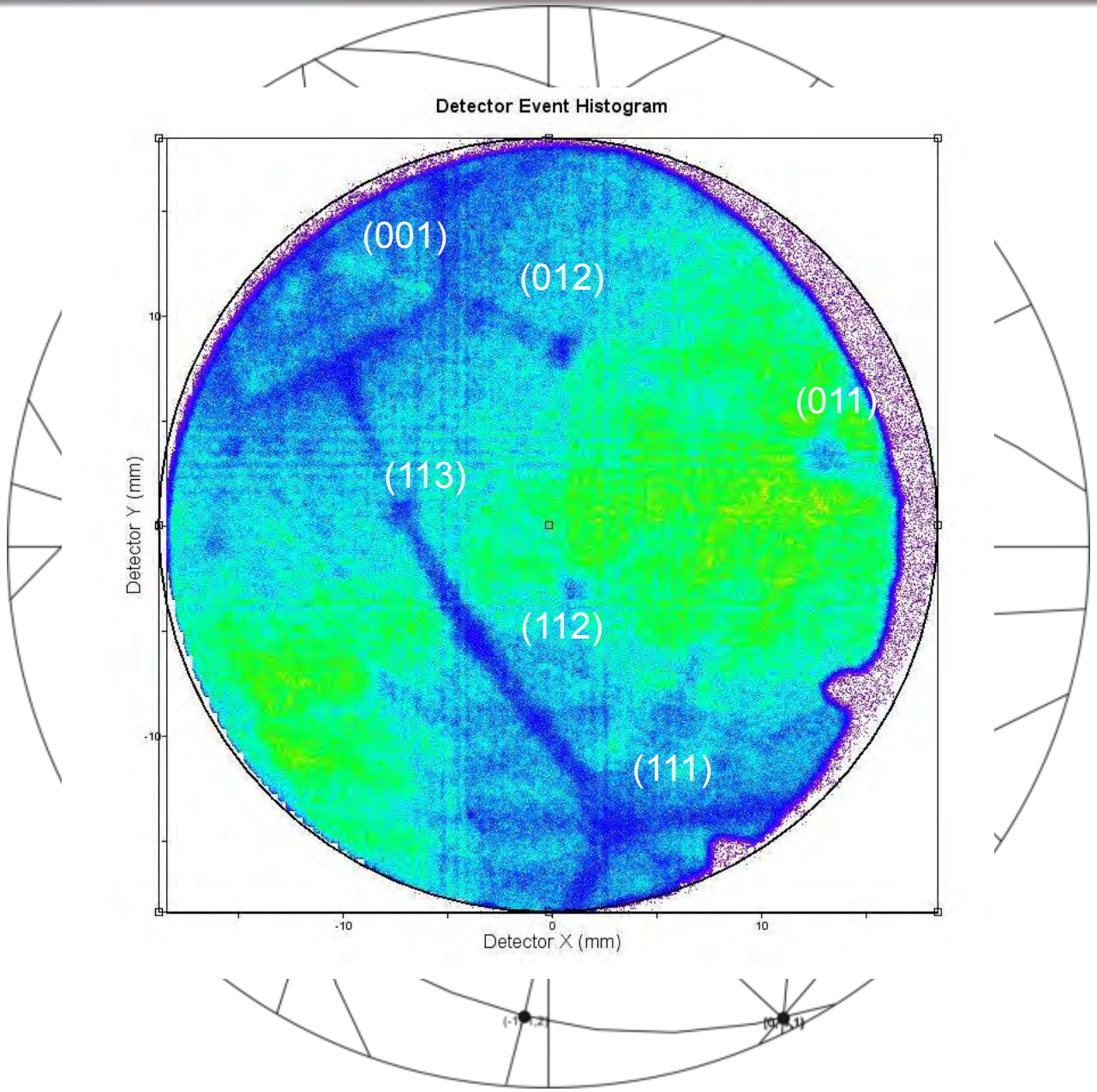

Lattice plane reconstruction

Fe_3Al ordered phase (only Al displayed)

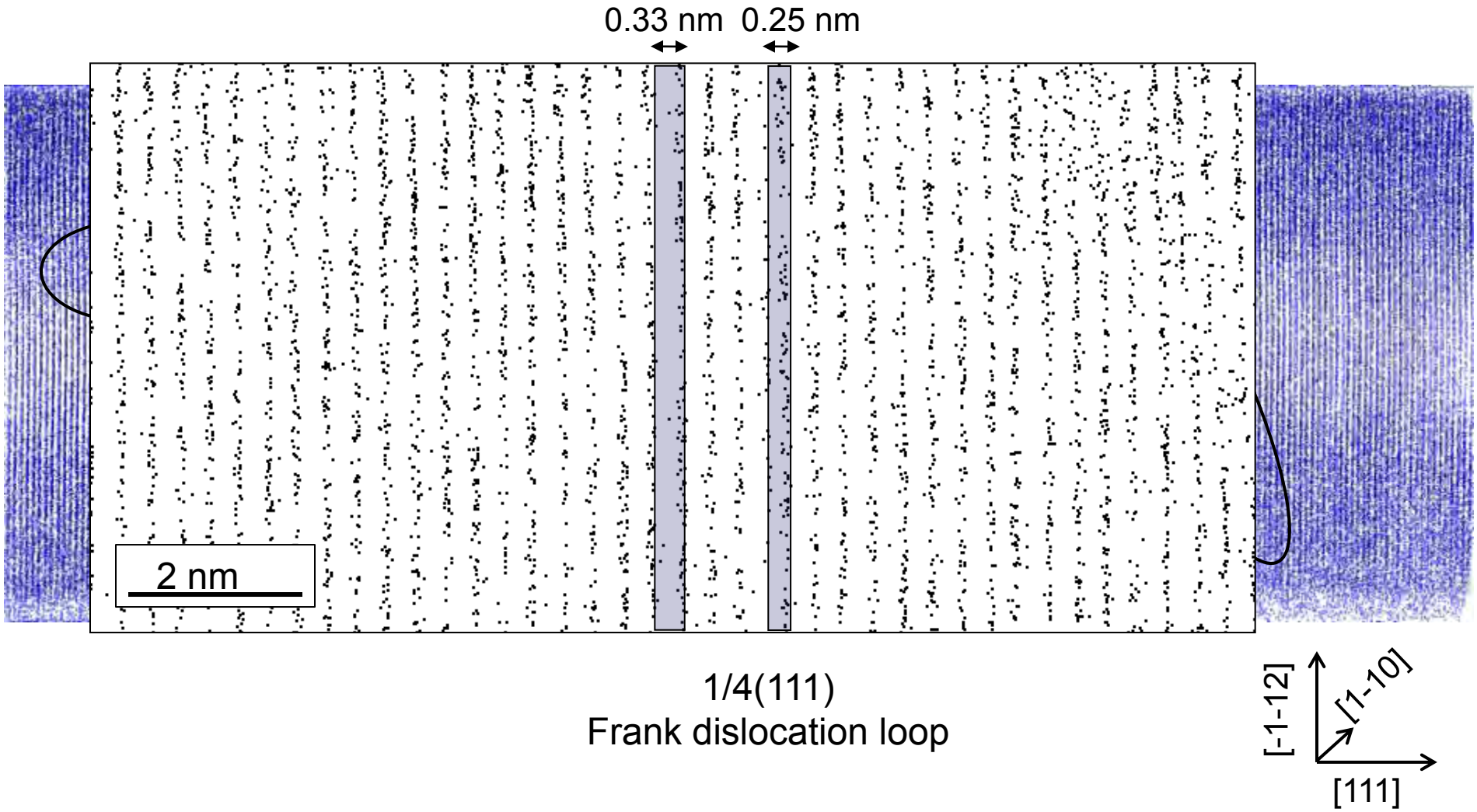

Atom probe tomography – application examples at MPIE

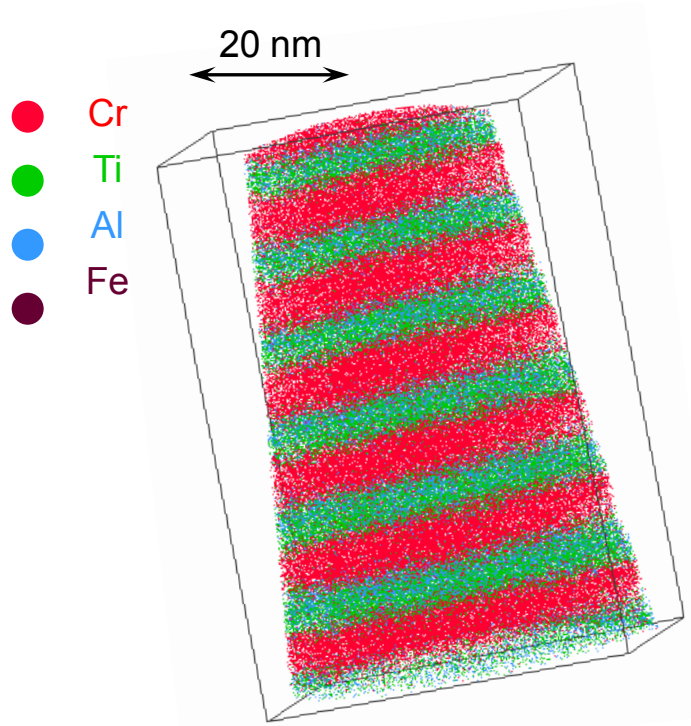

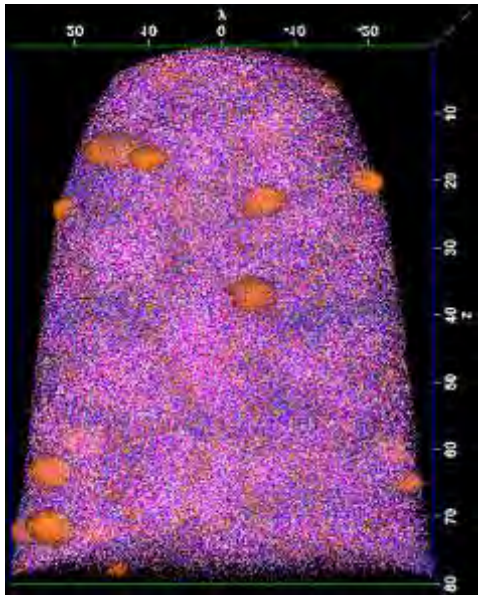

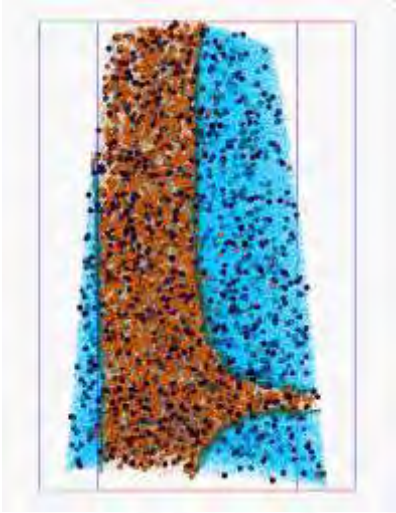

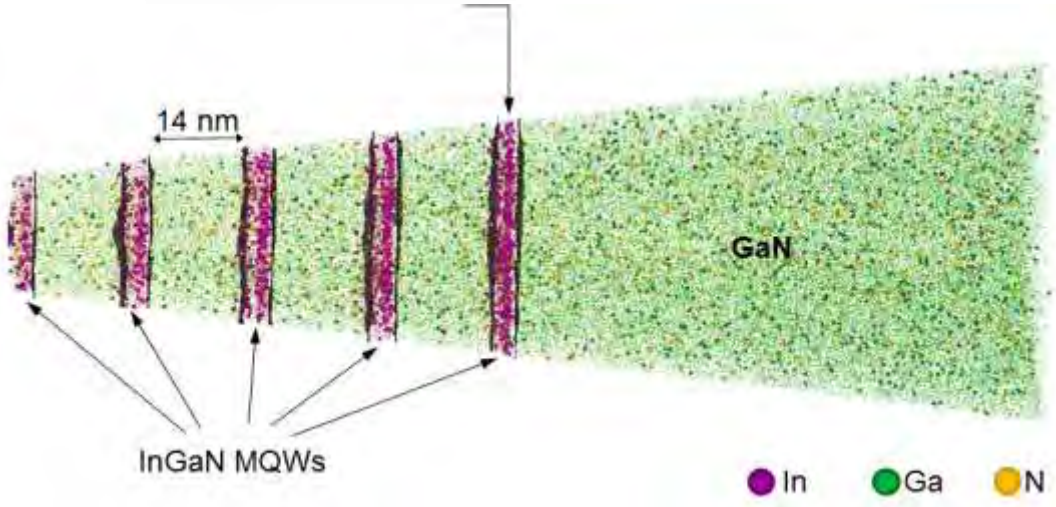

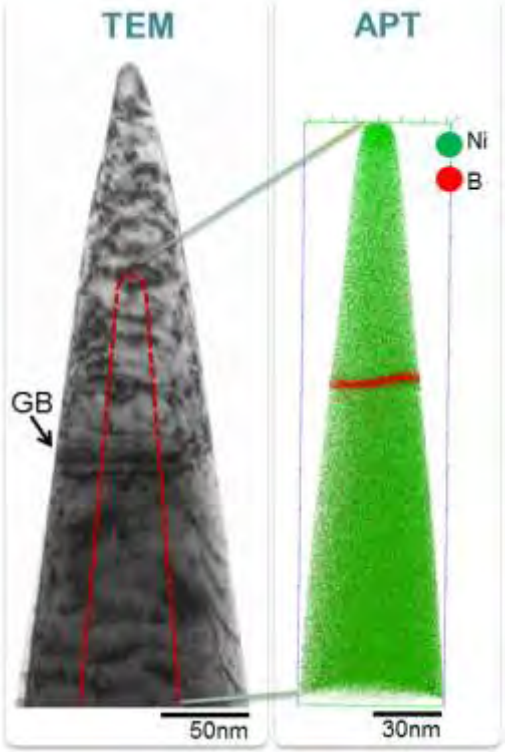

Examples

Fe-Mn-C TWIP steels

Pearlite: the limits of strength

Nano-austenite reversion

Fe-based ‘superalloy‘

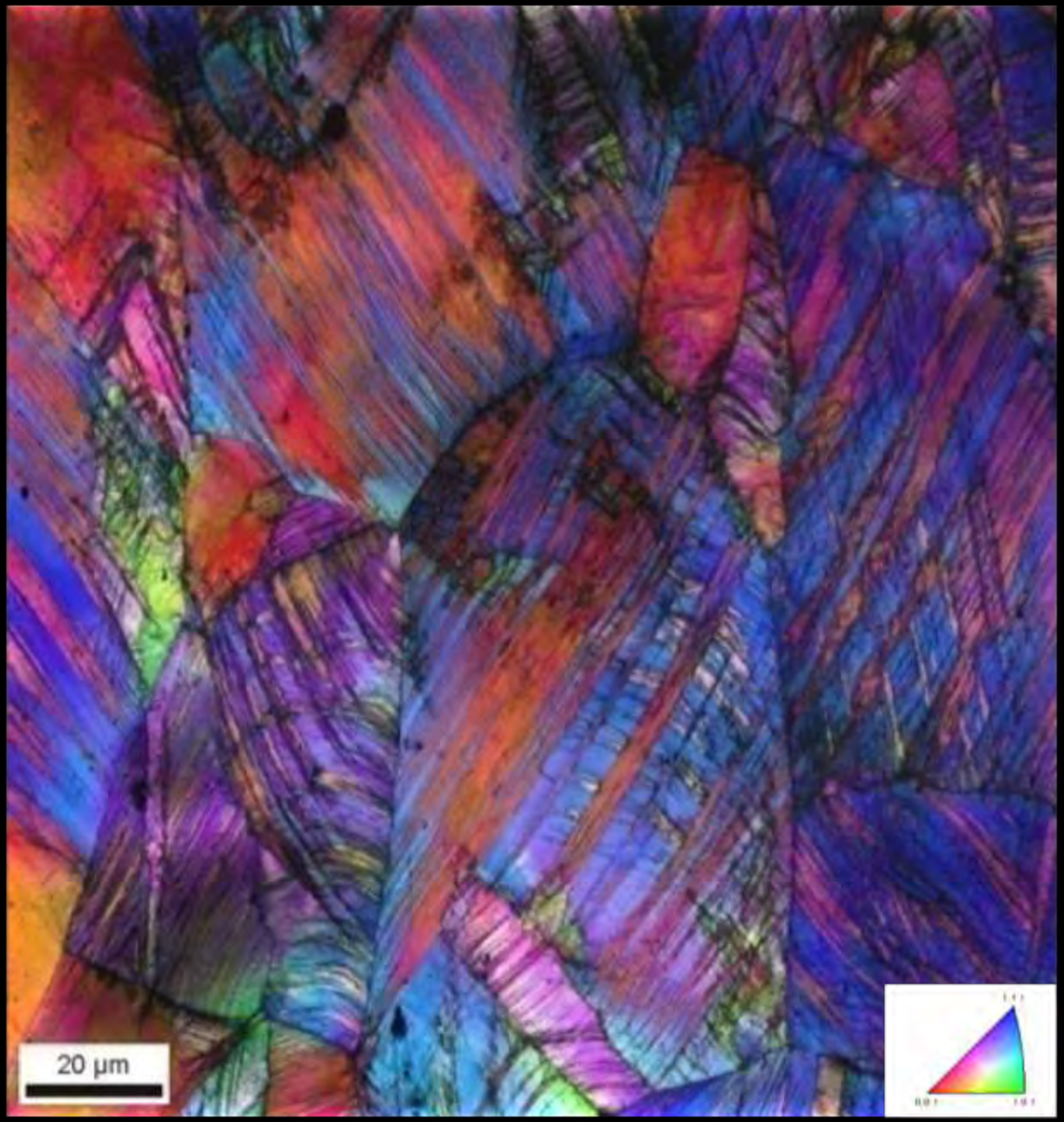

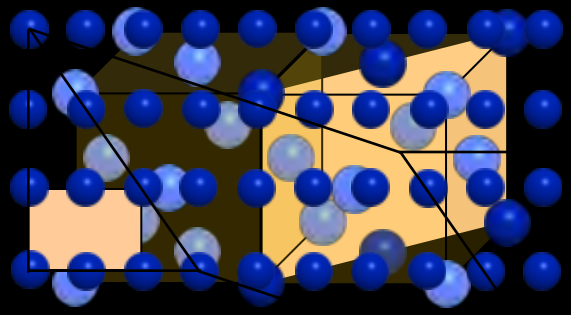

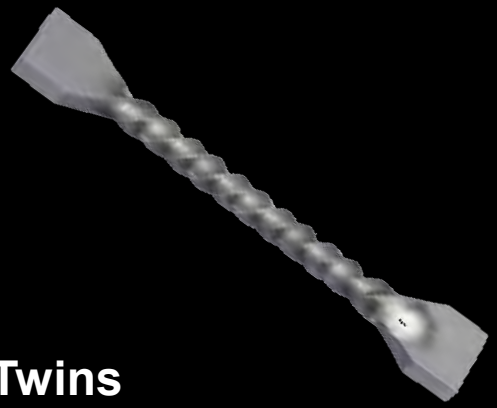

Twins
Double cross slip

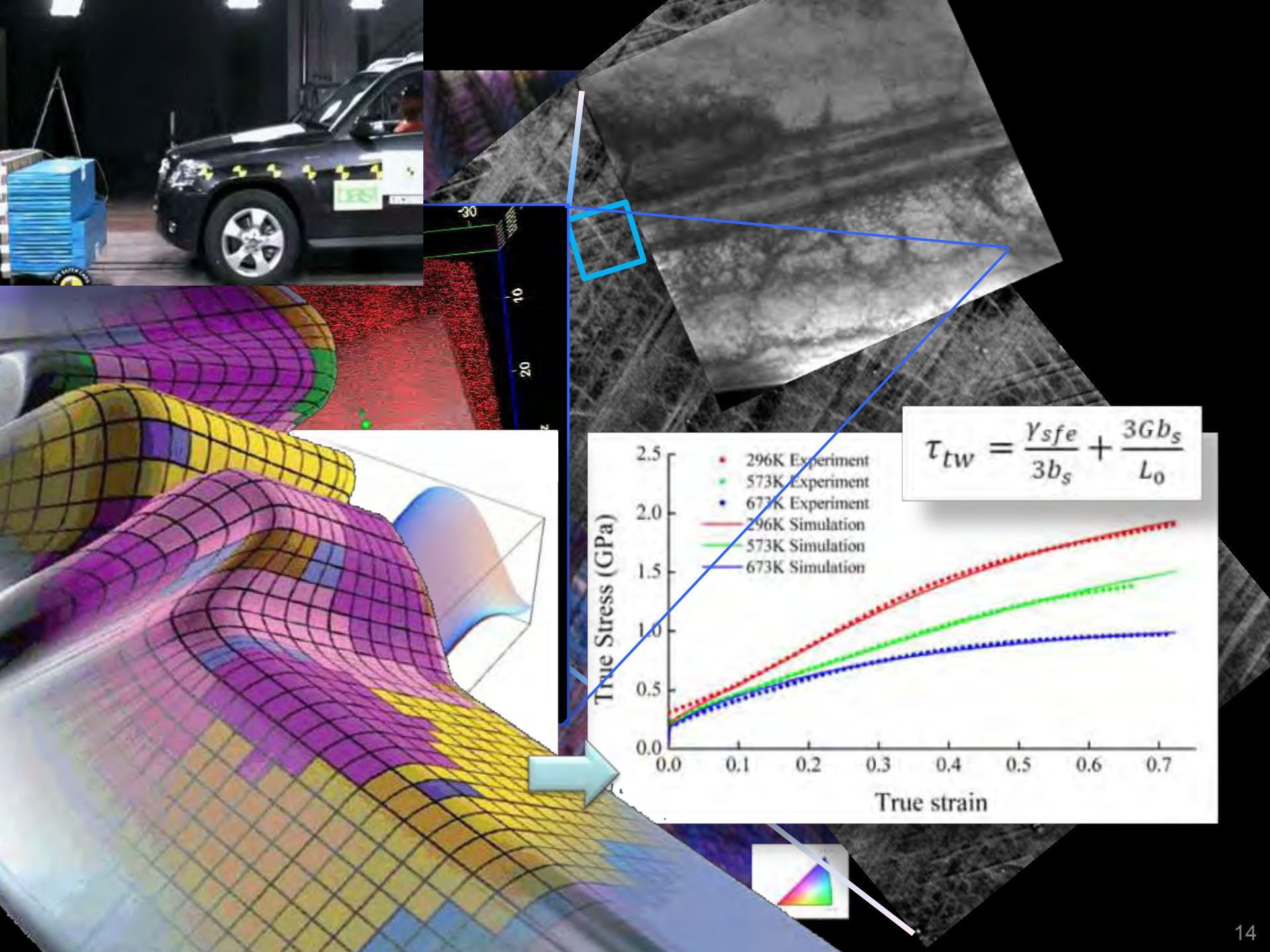
-30
-10
-20
$\tau_{tw} = \frac{\gamma_{sfe}}{3b_s} + \frac{3Gb_s}{L_0}$
296K Experiment
573K Experiment
673K Experiment
296K Simulation
573K Simulation
673K Simulation
True Stress (GPa)
True strain
2.5
2.0
1.5
1.0
0.5
0.0
0.0
0.1
0.2
0.3
0.4
0.5
0.6
0.7

Examples

Fe-Mn-C TWIP steels

Pearlite: the limits of strength

Nano-austenite reversion

Fe-based ‘superalloy‘

Towards the limits of strength and strain hardening

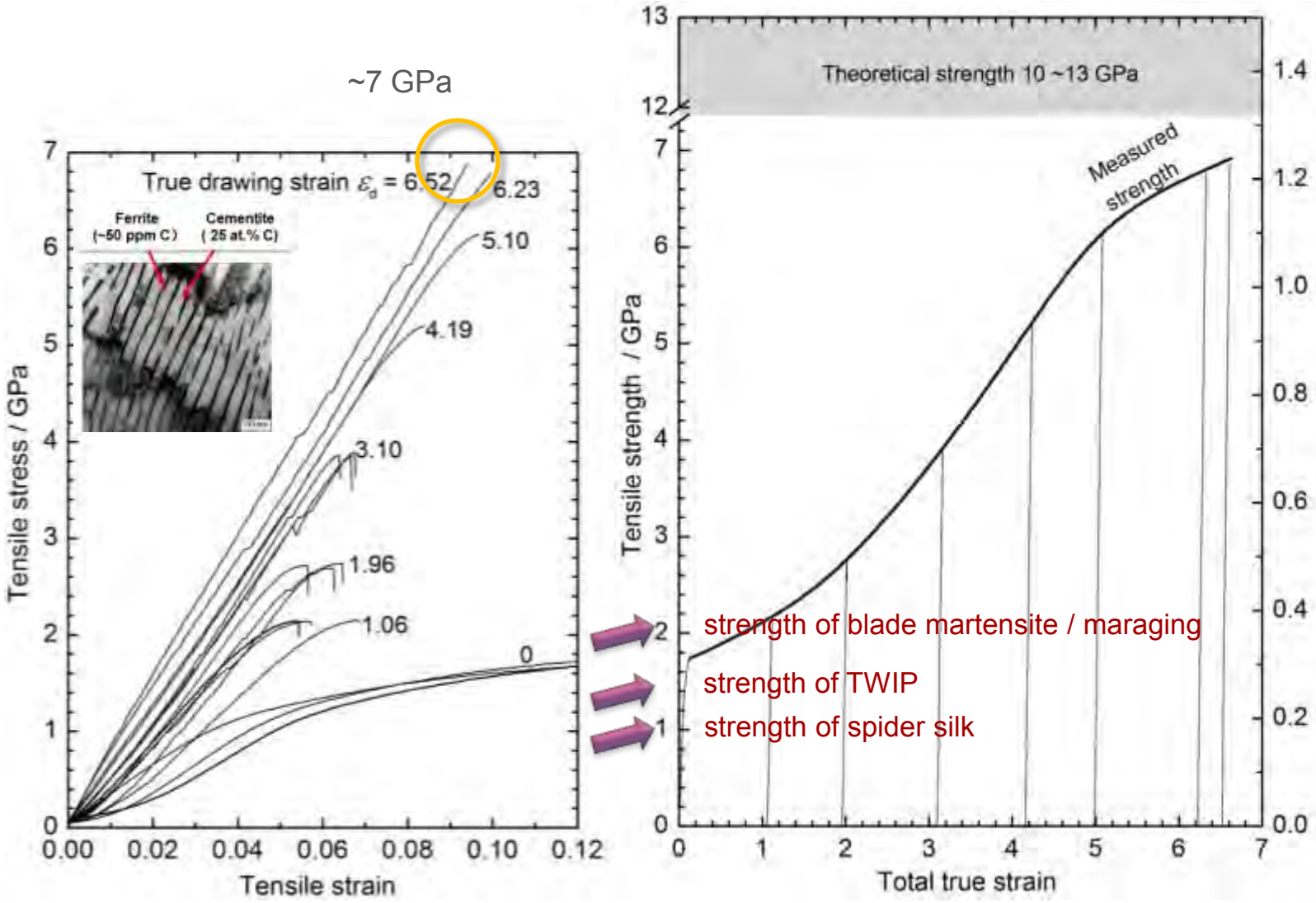

Towards the limits of strength: cold-drawn pearlitic steel

Ferrite (~50 ppm C) **Cementite (25 at.% C)**

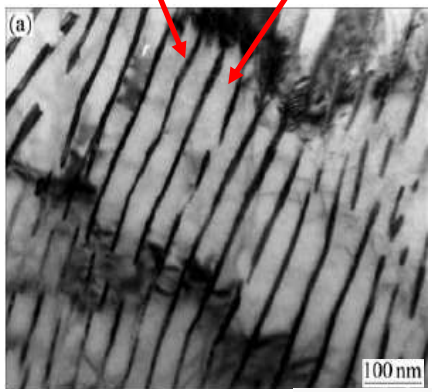

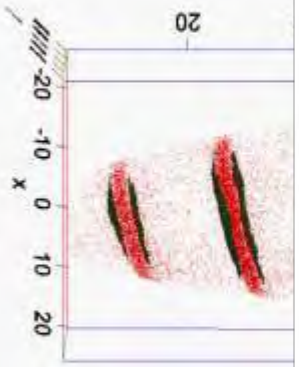

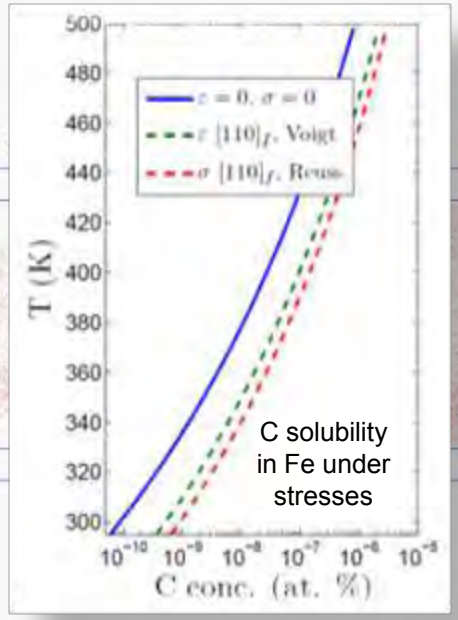

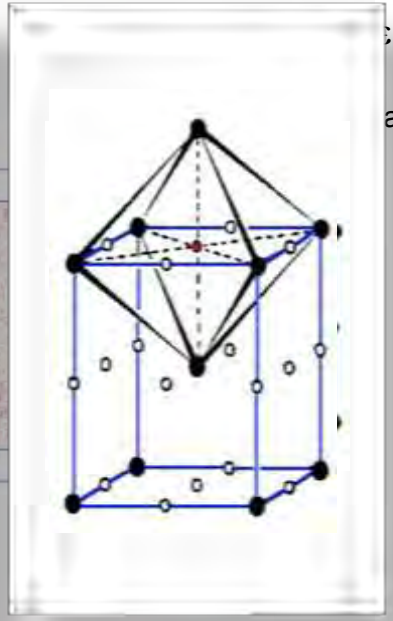

(ε = 2)

ale: nm

C iso-concentration (7 at.%)

• C

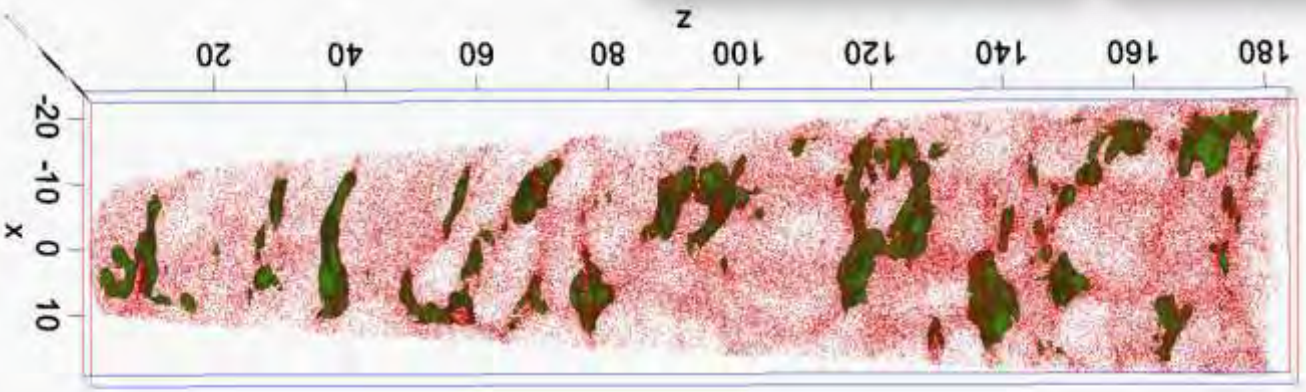

(ε = 6.5)

Examples

Fe-Mn-C TWIP steels

Pearlite: the limits of strength

Nano-austenite reversion

Fe-based ‘superalloy‘

Segregation Engineering: nanostructuring by transformation

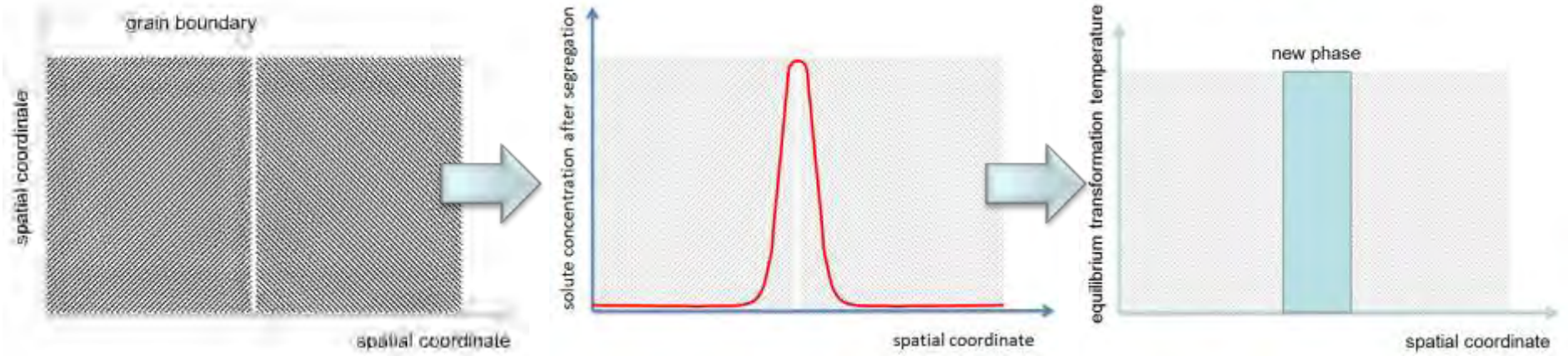

Solute segregation to martensite grain boundaries

Local phase transformation at grain boundary
(martensite-to-austenite reversion confined to GB)

Self-organized nanostructuring by selective phase transformation

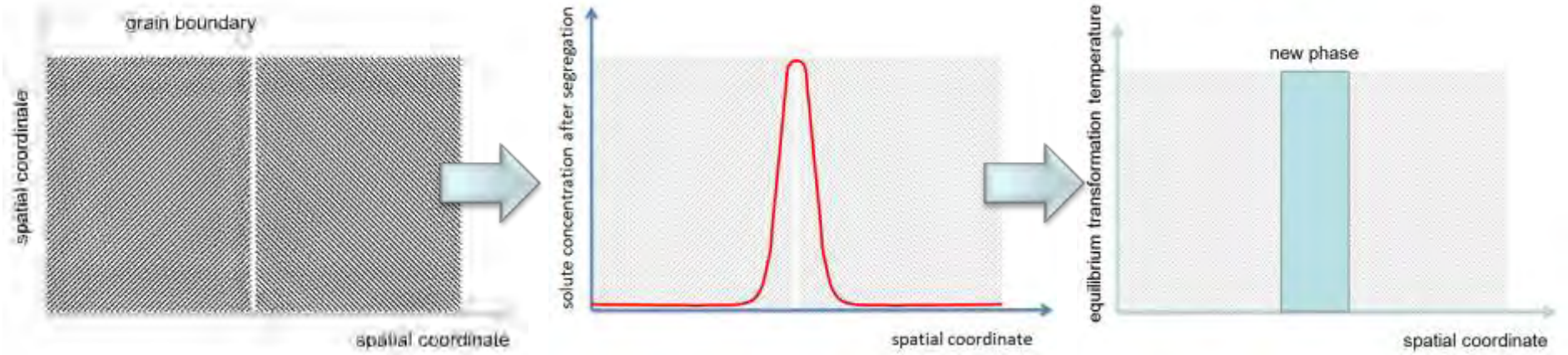

Solute segregation to martensite grain boundaries

- Element with high segregation tendency
- Reduce transformation temperature (e.g. from martensite to austenite)
- Prefer segregation over bulk precipitation (e.g. carbide)

Local phase transformation at grain boundary
(martensite-to-austenite reversion confined to GB)

Mn segregation at grain boundary, (450°C/65h)

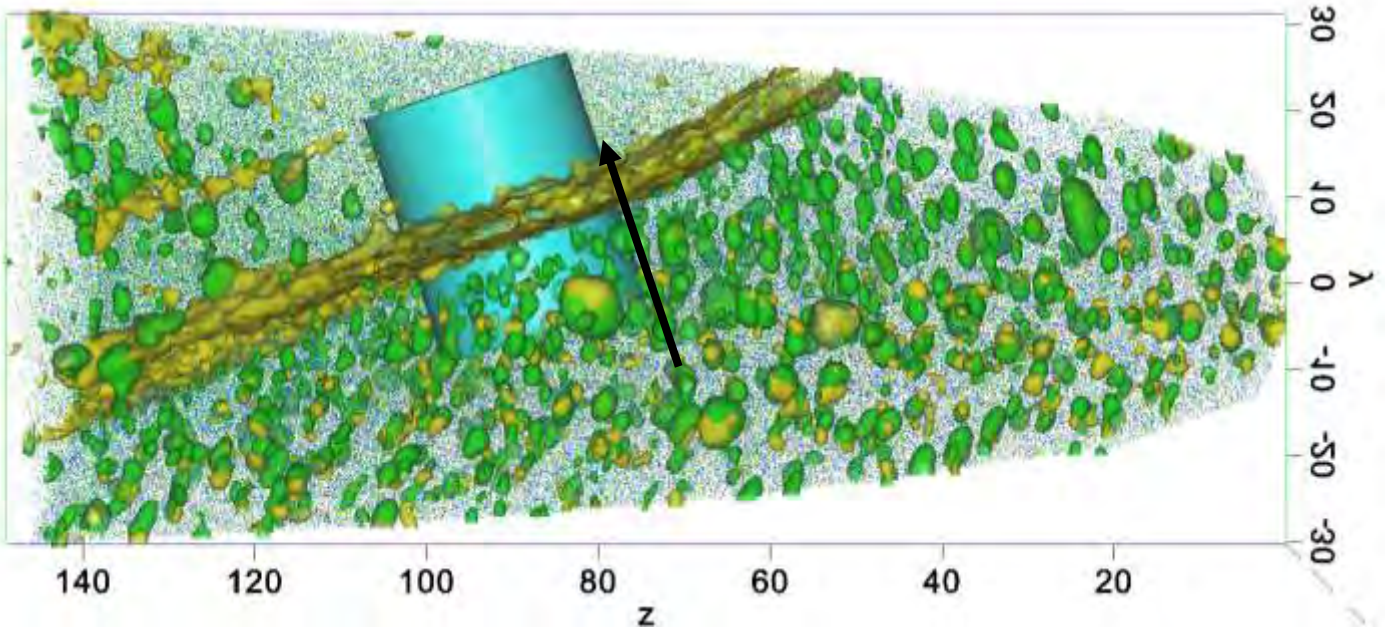

20 nm

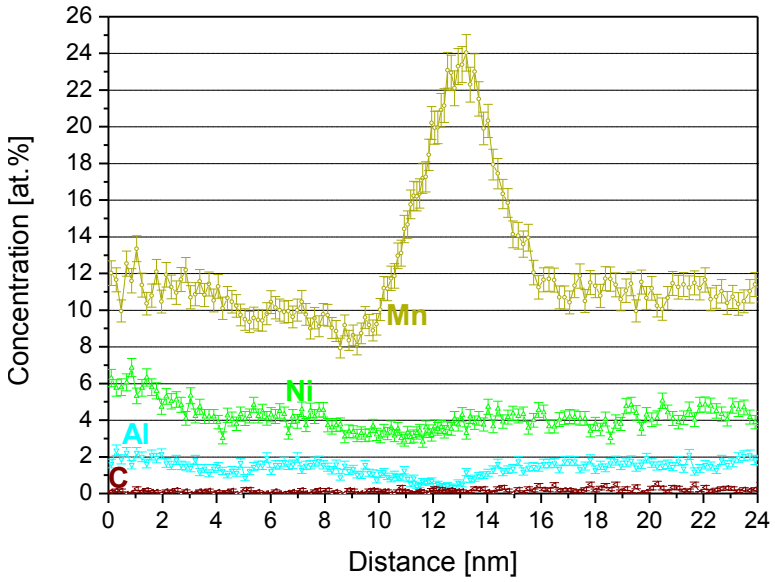

9Mn-2Ni-0.15Al-1Ti-1Mo (wt.%)

9Mn-2Ni-0.15Al-1Ti-1Mo (wt.%), aged 450°C/65h

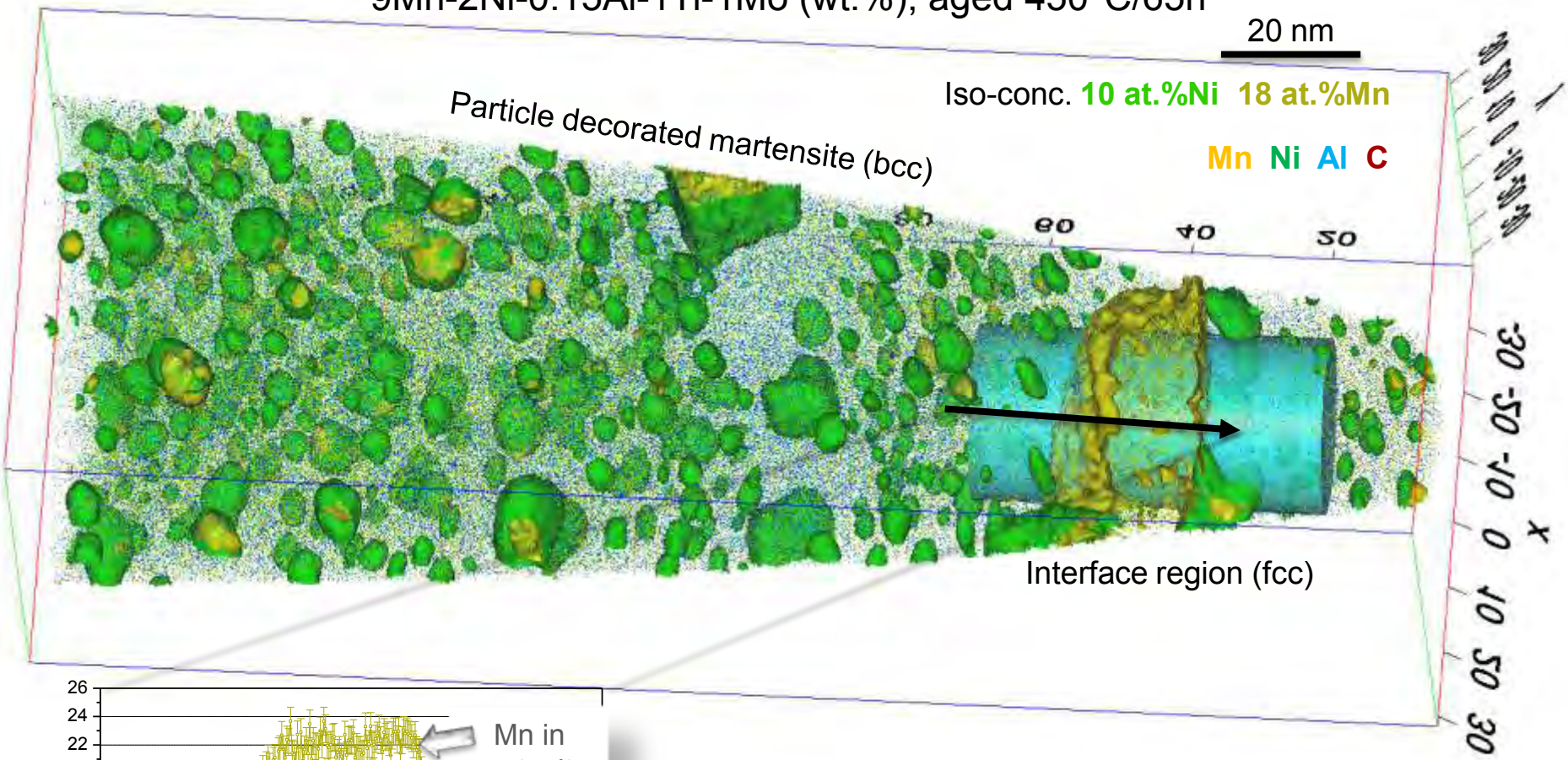

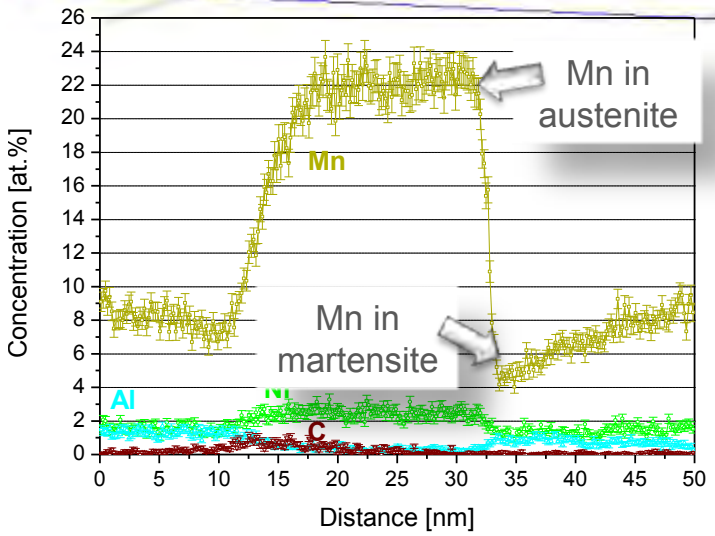

Phase formation at martensite interface
Near-equilibrium partitioning at interface

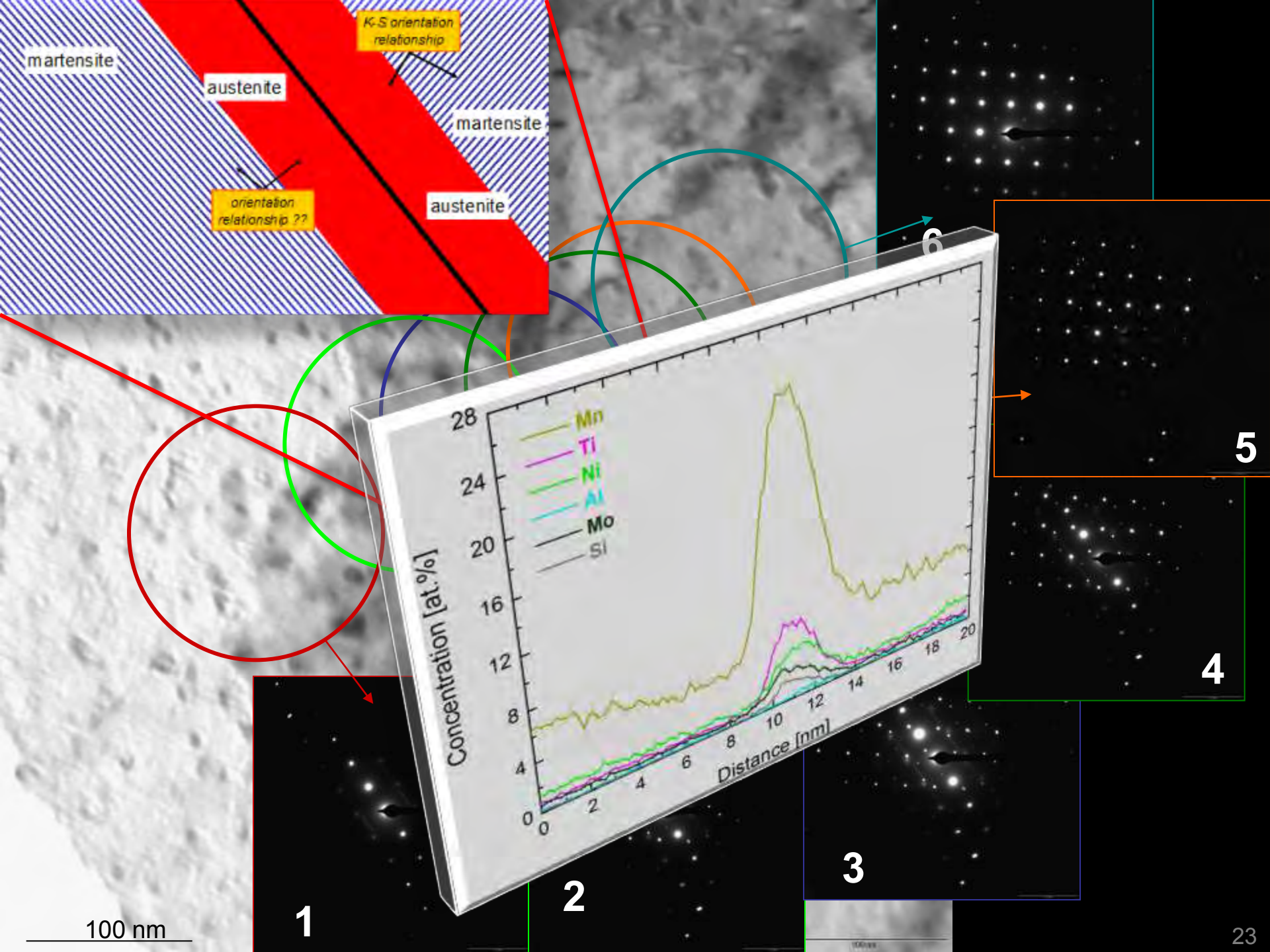
martensite
austenite
K-S orientation relationship
martensite
orientation relationship ??
austenite
6
5
4
3
2
1
Mn
Ti
Ni
Al
Mo
Si
Concentration [at.%]
Distance [nm]
0
4
8
12
16
20
24
28
0
2
4
6
8
10
12
14
16
18
20
100 nm

Martensite relaxation & aging & nanoscale austenite reversion

650 MPa to 2 GPa

Making martensite ductile

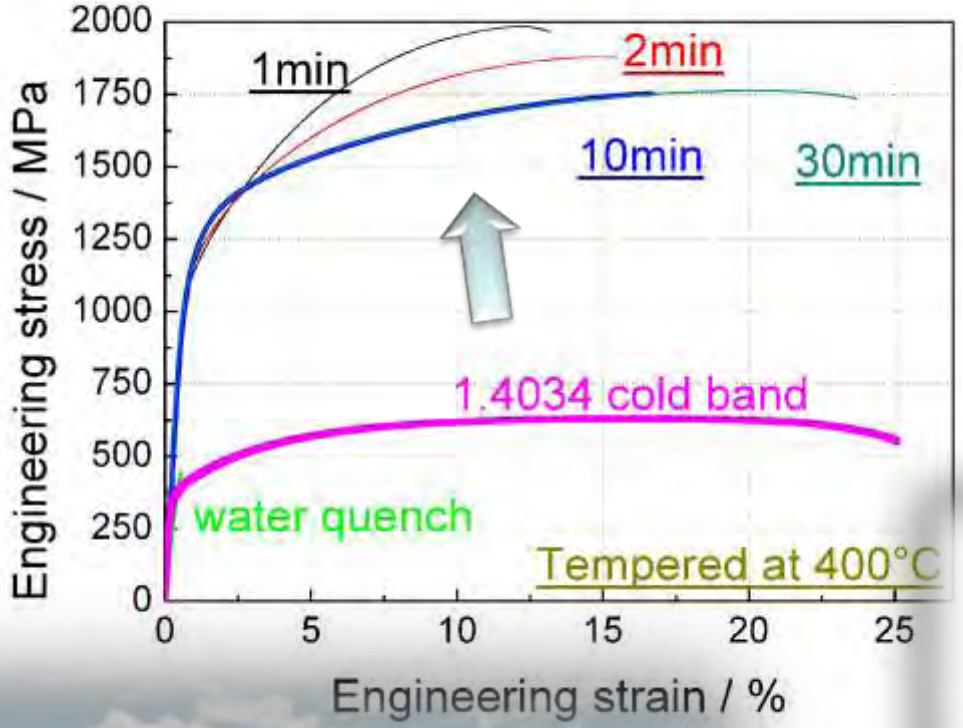

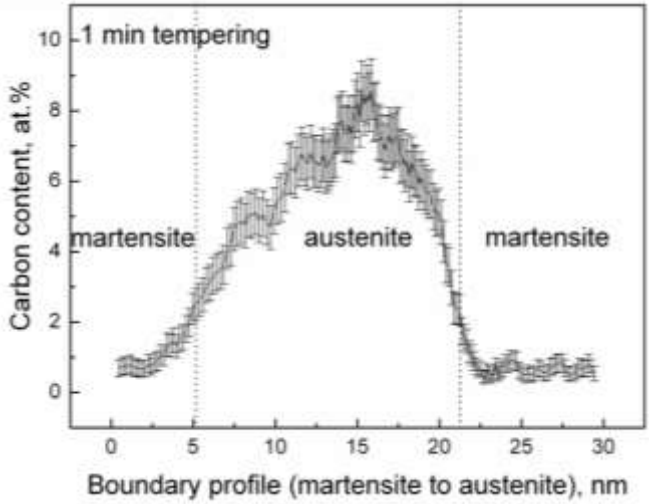

Fe-13.6Cr-0.44C (wt.%)

Examples

Fe-Mn-C TWIP steels

Pearlite: the limits of strength

Nano-austenite reversion

Fe-based ‘superalloy‘

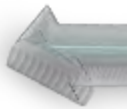

Fe-Mn-Al-C weight reduced alloys (10% less mass density)

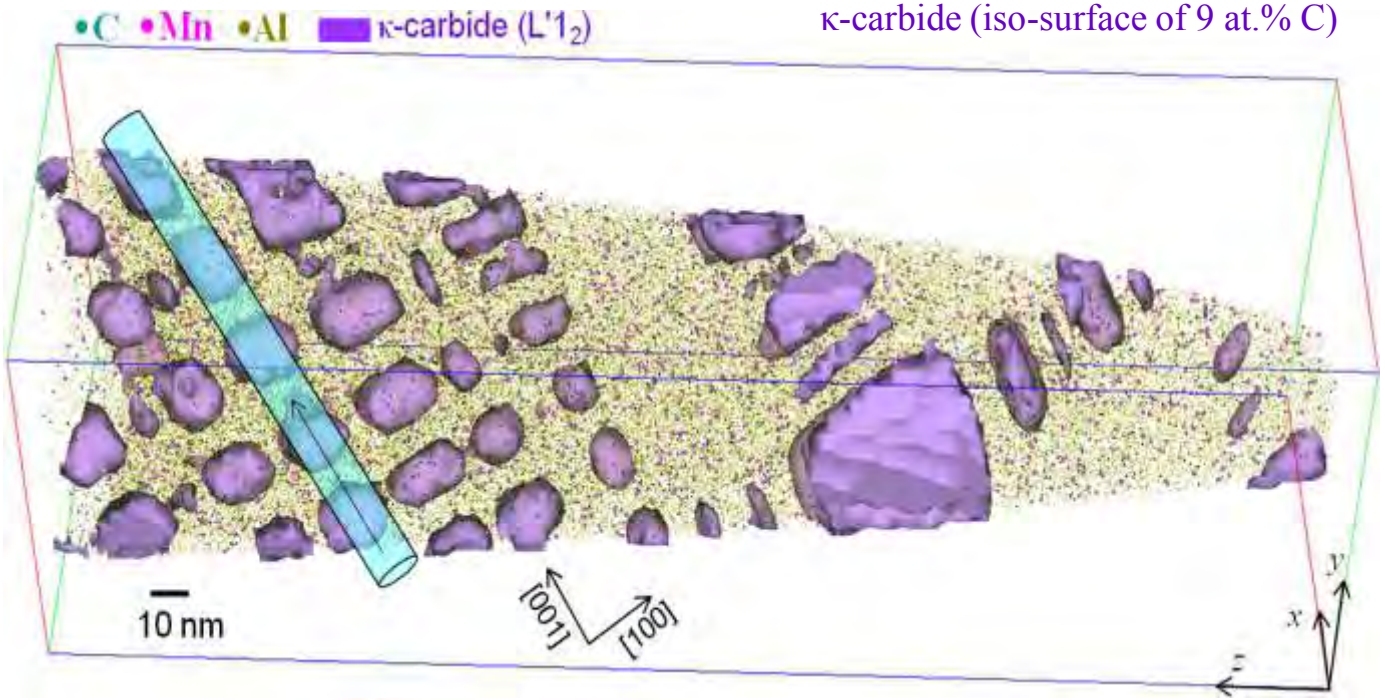

κ-carbide (iso-surface of 9 at.% C)

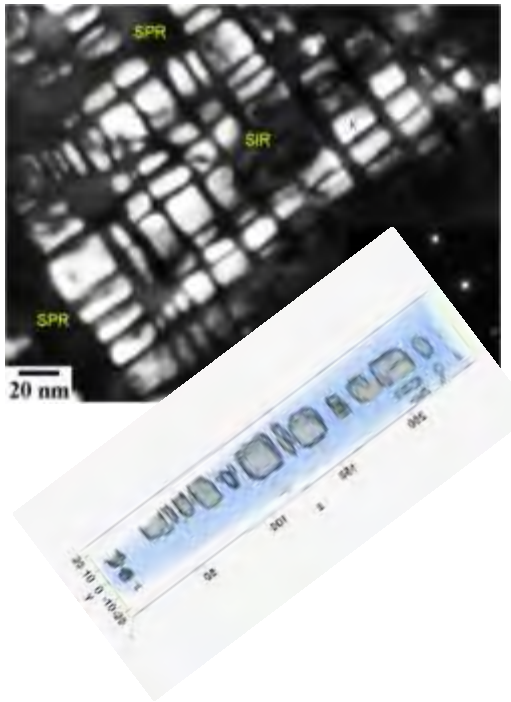

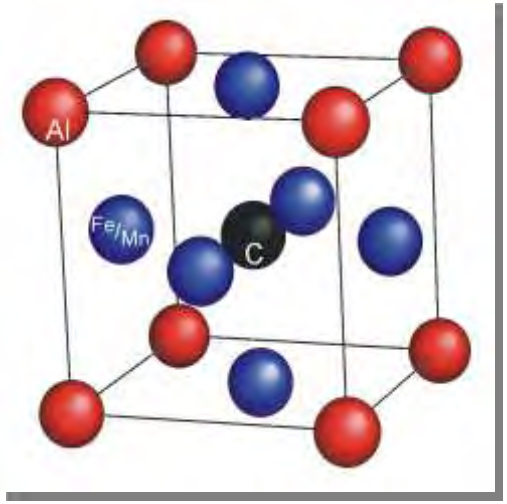

Lattice structure
of κ-Carbides,
Perowskite type

Fe-Mn-Al-C weight reduced alloys (10% less mass densit…)

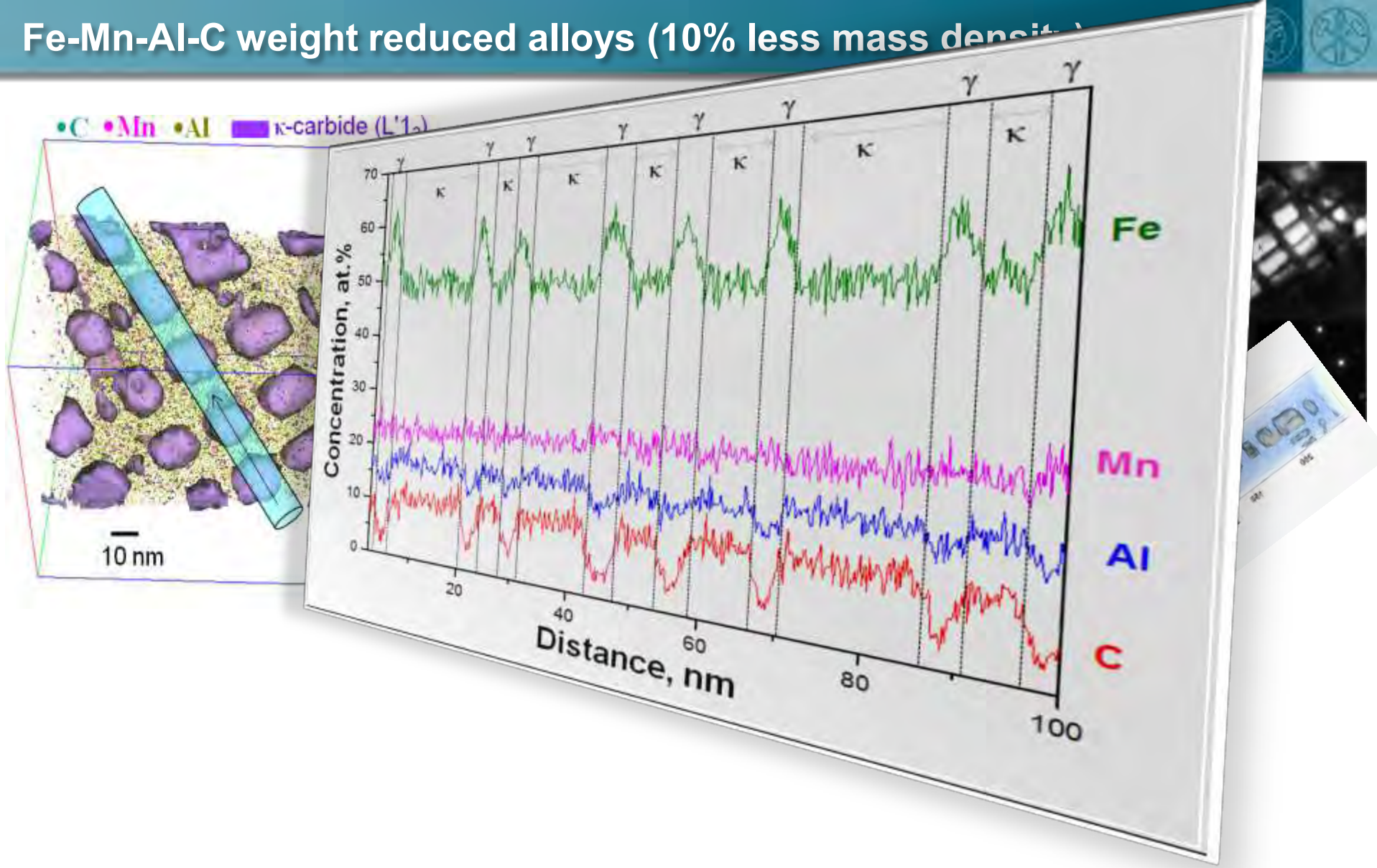

Rapid alloy prototyping: other alloy systems

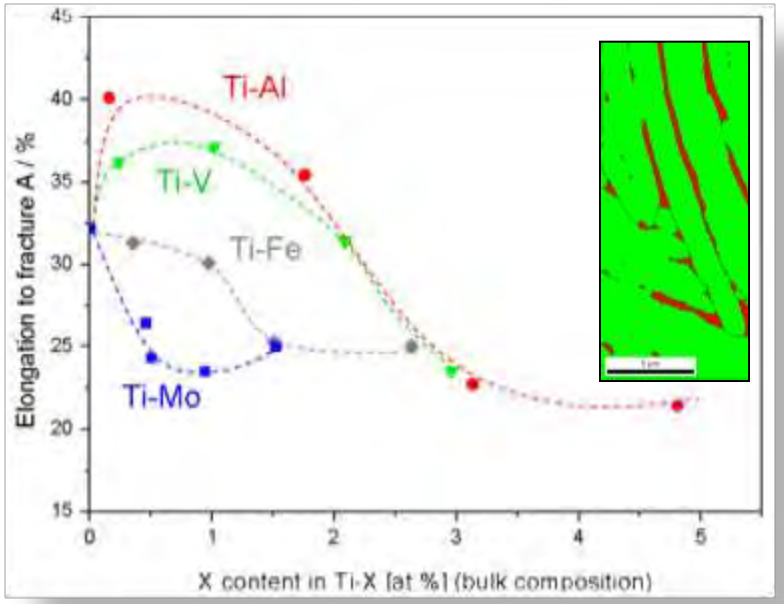

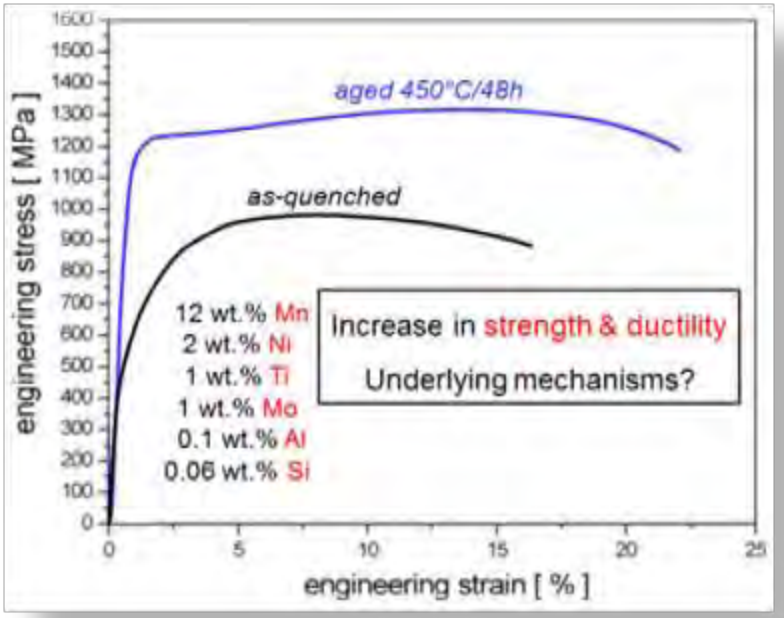

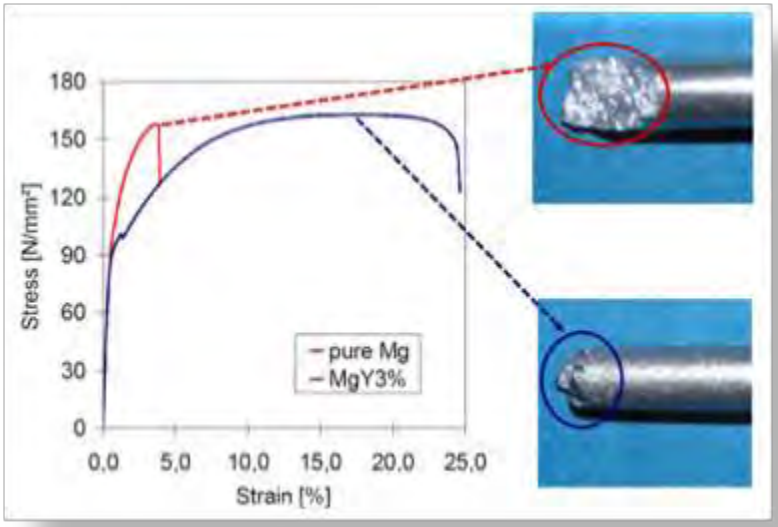

Conclusions

- Design alloys by self-organized nanostructuring
- Segregation plus confined phase transformation at defects
- Mechanical alloying leads to non-equilibrium phases approaching the theoretical limits of strength
- Designing stable nanocarbides enables weight-reduced ultra-ductile and thermally stable materials

The Düsseldorf Max-Planck Team

References

D. R. Steinmetz, T. Jäpel, B. Wietbrock, P. Eisenlohr, I. Gutierrez-Urrutia, A. Saeed-Akbari, T. Hickel, F. Roters, D. Raabe: Acta Materialia 61 (2013) 494-510
Revealing the strain-hardening behavior of twinning-induced plasticity steels: Theory, simulations, experiments

J.-B. Seol, D. Raabe. P. Choi, Y.-R Im, C.-G. Park: Acta Materialia 60 (2012) 6183-6199
Atomic scale effects of alloying, partitioning, solute drag and austempering on the mechanical properties of high-carbon bainitic–austenitic TRIP steels

S. Reeh, D. Music, T. Gebhardt, M. Kasprzak, T. Jäpel, S. Zaefferer, D. Raabe, S. Richter, A. Schwedt, J. Mayer, B. Wietbrock, G. Hirt, J.M. Schneider: Acta Materialia 60 (2012) 6025–6032
Elastic properties of face-centred cubic Fe–Mn–C studied by nanoindentation and ab initio calculations

O. Dmitrieva, D. Ponge, G. Inden, J. Millán, P. Choi, J. Sietsma, D. Raabe: Acta Materialia 59 (2011) 364-374, DOI: 10.1016/j.actamat.2010.09.042
Chemical gradients across phase boundaries between martensite and austenite in steel studied by atom probe tomography and simulation

Available online at www.sciencedirect.com

SciVerse ScienceDirect

Acta Materialia 60 (2012) 6025–6032

Acta MATERIALIA

www.elsevier.com/locate/actamat

Elastic properties of face-centred cubic Fe–Mn–C studied by nanoindentation and ab initio calculations

S. Reeh [a,*], D. Music [a], T. Gebhardt [a], M. Kasprzak [a], T. Jäpel [b], S. Zaefferer [b], D. Raabe [b], S. Richter [c], A. Schwedt [c], J. Mayer [c], B. Wietbrock [d], G. Hirt [d], J.M. Schneider [a]

[a] Materials Chemistry, RWTH Aachen University, D-52056 Aachen, Germany
[b] Max-Planck-Institut für Eisenforschung GmbH, D-40237 Düsseldorf, Germany
[c] Central Facility for Electron Microscopy, RWTH Aachen University, D-52056 Aachen, Germany
[d] Institute of Metal Forming, RWTH Aachen University, D-52056 Aachen, Germany

Received 22 March 2012; received in revised form 10 July 2012; accepted 11 July 2012
Available online 16 August 2012

Abstract

We have studied experimentally and theoretically the influence of C and Mn content on the Young's modulus of Fe–Mn–C alloys. Combinatorial thin film and bulk samples were characterized regarding their structure, texture and Young's modulus. The following chemical composition range was investigated: 1.5–3.0 at.% C, 28.0–37.5 at.% Mn and 60.6–69.8 at.% Fe. The experimental lattice parameters change marginally within 3.597–3.614 Å with the addition of C and are consistent with ab initio calculations. The Young's modulus data are in the range of 185 ± 12–251 ± 59 GPa for the bulk samples and the thin film, respectively. C has no significant effect on the Young's modulus of these alloys within the composition range studied here. The ab initio calculations are 15–22% larger than the average Young's modulus values of the as-deposited and polished thin film at 3 at.% C. The comparison of thin film and bulk samples results reveals similar elastic properties for equivalent compositions, indicating that the applied research strategy consisting of the combinatorial thin film approach in conjunction with ab initio calculations is useful to study the composition dependence of the structure and elastic properties of Fe–Mn–C alloys. The very good agreement between the presented calculations and the experimentally determined lattice parameters and Young's modulus values implies that the here-adopted simulation strategy yields a reliable description of carbon in Fe–Mn alloys, important for future alloy design.

Keywords: Iron alloys; Sputtering; Elastic behaviour; Ab initio electron theory; Nanoindentation

1. Introduction

Mn-rich transformation-induced plasticity/twinning-induced plasticity (TRIP/TWIP) steels reveal outstanding mechanical properties combining high strength (>1000 MPa) and superior ductility (elongation to failure of >50%) [1,2]. These exceptional properties are due to dislocation glide, mechanical twinning and strain-induced ε- and α-martensitic transformations [1]. The formation of twins (TWIP effect) or multiple martensitic transformations (TRIP effect) under mechanical load is affected by the stacking fault energy (SFE), which is dependent on temperature and chemical composition [3,4]. The influence of SFE [4], temperature [4,5] and strain rate [5] on the deformation mechanisms and the interactions among the various deformation mechanisms of face-centred cubic (fcc) Fe–Mn–C steels has been studied in a number of papers [6,7].

In contrast the C-induced changes on the elastic properties of high Mn steels have not been studied systematically before.

* Corresponding author. Tel.: +49 241 80 25984; fax: +49 241 80 22295.
E-mail address: reeh@mch.rwth-aachen.de (S. Reeh).

1359-6454/$36.00 © 2012 Acta Materialia Inc. Published by Elsevier Ltd. All rights reserved.
http://dx.doi.org/10.1016/j.actamat.2012.07.038

For the binary fcc Fe–Mn random alloys elastic properties have been reported by Music et al. [8], Gebhardt et al. [9] and Cankurtaran et al. [10]. Even though these alloys are antiferromagnetic (AFM) with Néel temperatures well above room temperature, their elastic properties are well predicted using the disordered local moment (DLM) approach [8,9] to describe the magnetic configuration. With magnetically ordered configurations, such as AFM, the stiffness of these random alloys is overestimated due to lack of lattice softening [9]. However, there are no systematic data on the dependence of the Young's modulus values on the C concentration in ternary fcc Fe–Mn–C alloys.

In this paper, the influence of the C and Mn content on the Young's modulus of fcc Fe–Mn–C steel thin film synthesized by combinatorial sputter deposition is systematically investigated and compared to the same data obtained from bulk samples. Ab initio calculations are carried out to determine the Young's modulus of selected Fe–Mn–C alloys and to correlate these with the electronic structure.

2. Experimental section

2.1. Thin film samples

The Fe–Mn–C thin films were grown by DC combinatorial magnetron sputtering. The depositions were carried out in a high vacuum chamber with a base pressure of 1.1×10^{-5} Pa using a system described in Ref. [9]. Fe, $Fe_{50}Mn_{50}$ and C targets, with 99.95% purity for Fe and $Fe_{50}Mn_{50}$ and 99.999% purity for C, were placed on three magnetrons. Magnetron power densities of 2.0, 3.2 and 0.5 W cm^{-2} were applied, respectively. The sputtering gas was Ar (99.9999% purity) and the pressure during deposition was 0.8 Pa. The substrate was a 2 in. sapphire wafer with a (0 0 0 1) orientation, which was heated to 450 °C during deposition. The substrate-to-target distance was ~10 cm. The Young's modulus values were determined in the as-deposited state with a root mean square roughness (R_q) of 57 nm; after polishing the R_q value was 15 nm, measured on an area of 94.2 μm × 70.7 μm.

2.2. Bulk samples

Two different types of bulk samples were produced: sample type A (A1, A2 and A3) and sample type B (B1, B2 and B3). The differences between these specimen sets are that the samples were produced in different ways (see below) and that samples B contain impurities of Al, S, P, Si, Cr, Ni, Mo, Cu, Co, Nb, V, Sn and N, which are typically introduced during large scale steel processing, while the samples A contain no detectable amounts of these impurities. The compositions of all bulk samples are given in Table 1. This experimental strategy allows for a direct comparison of the data obtained from bulk and thin film samples with results from ab initio calculations. Furthermore, the comparison between bulk specimens with and without impurities may shed light on the role of impurities for the Young's modulus and structure evolution.

For samples A, Fe (99.998% purity), Mn (99.99% purity) and C powders (99.9999% purity) were mixed and inductively melted. The melting was done in an inert atmosphere with a heating rate of 6 K s^{-1} from room temperature up to 1520 °C. The dwelling time at this temperature was 4 min, followed by cooling at a rate of 50 K s^{-1}. Samples with a diameter of 5 mm were mounted in conductive resin and subsequently polished to a roughness R_q of 19 nm for A1, 14 nm for A2 and 32 nm for A3 measured on an area of 94.2 μm × 70.7 μm.

The three samples, B, B1, B2 and B3, were cast in a vacuum induction melter at 1550 °C and solidified as slabs with a 140 × 140 mm^2 cross-section and a weight up to 100 kg. These samples were then processed into hot strips, starting with forging at 1150 °C with 60% thickness reduction, followed by rolling down at 1150 °C to ~3 mm thickness within 12 passes and an overall thickness reduction of 95%. The samples were cut into dimensions of 10 mm × 10 mm × 3 mm, mounted in conductive resin and polished to a roughness R_q of 16 nm for B1 and B2 as well as 20 nm for B3 measured on an area of 94.2 μm × 70.7 μm.

2.3. Analysis

2.3.1. Chemical composition

The chemical composition of the thin film and the bulk samples was measured using wavelength-dispersive spectroscopy (WDS) in a CAMEBAX SX 50 electron probe microanalyser. A focused electron beam of 15 keV with a current of 80 nA was used. The dwell time for each measured position was 10 s. The characteristic X-ray intensities were calibrated by using the following standards: Fe_3C, Mn and Fe. The calibrated intensities (k-ratios) were transferred into elemental concentrations with the help of a matrix correction procedure based on a special PHI (rhoz)-method, the so-called PAP correction procedure. Under the chosen conditions the sensitivity of the measurement is 0.23 at.% for C, 0.02 at.% for Mn and 0.03 at.% for Fe.

2.3.2. Structure and crystallographic texture analysis

The structure of the thin films was determined by X-ray diffraction in a Bruker D8 with a general area detection diffraction system (GADDS) with Cu Kα radiation at a constant angle of incidence of 15° with a 0.5 mm collimator covering a 2θ range of 35–85°. The structure of the bulk samples was measured by using a Siemens D5000 diffractometer using line-focused Cu Kα radiation in Bragg–Brentano beam geometry.

The electron backscatter diffraction (EBSD) technique was employed to analyse the local crystallographic texture in conjunction with the microstructure. In this study, EBSD for the bulk samples was carried out in a high-resolution, high-beam current field emission scanning electron

Table 1
Chemical composition of the bulk samples in at.%.

Sample	Fe	C	Mn	Si	P	S	Cr	Ni	Mo	Al	Cu	Co	Nb	V	Sn	N
A1	74.4	1.5	24.1	–	–	–	–	–	–	–	–	–	–	–	–	–
A2	74.0	1.2	24.8	–	–	–	–	–	–	–	–	–	–	–	–	–
A3	76.1	0.6	23.3	–	–	–	–	–	–	–	–	–	–	–	–	–
B1	75.4	2.4	21.8	0.219	0.013	0.005	0.018	0.032	0.011	0.015	0.009	0.007	0.013	0.017	<0.0002	0.058
B2	69.7	1.3	27.8	0.200	0.015	<0.001	0.017	0.034	0.011	0.011	0.008	0.010	0.016	0.022	<0.0002	0.062
B3	74.8	1.4	22.6	0.128	0.013	0.002	0.017	0.034	0.008	0.011	0.009	0.009	0.015	0.012	<0.0002	0.043

microscopy (SEM) instrument (JEOL JSM 6500F). Pattern acquisition was done using a DigiView II CCD camera by TSL and the TSL OIM data collection software. Orientation information was acquired on a hexagonal grid, using a step size in the range of 50–100 μm. EBSD maps were measured at 15 kV acceleration voltage and a working distance of 15 mm.

The EBSD measurement for the thin film was performed using a DigiView III camera by EDAX-TSL attached to a JSM 7000F FEG-SEM by JEOL operating at a beam current of ~10 nA and a beam energy of 20 keV.

The measured diffraction patterns were evaluated using the software OIM Data Collection V 6.1.3 indexing the patterns as fcc, body-centred cubic (bcc) or hexagonal-close-packed (hcp) Fe. In total, a field of 20 μm × 30 μm was mapped at an EBSD step size of 50 nm at a position with 64.7 at.% Fe, 33.7 at.% Mn and 1.6 at.% C.

2.3.3. Young's modulus

The Young's modulus was investigated with a depth-sensing nanoindenter (Hysitron TriboIndenter™) equipped with a Berkovich tip. The Young's modulus values were evaluated according to the Oliver and Pharr method [11] using a Poisson ratio of 0.25 [9]. The tip was calibrated on fused silica.

For the as-deposited thin film, measurements at 22 different positions with 12 indents per position and a maximum load of 1500 μN were performed. The maximum penetration depth was less than 10% of the film thickness. After polishing of the thin film, nine positions were measured again to evaluate the influence of roughness on the measurements, with 16 indents per position with indentation depth less than 100 nm at a film thickness of 1.2 μm.

The elastic properties of samples A1, A2 and A3 were measured using 72 indents per sample and samples B1, B2 and B3 were subjected to 32 indents per sample, using the same maximum load as for the thin films.

3. Theoretical section

The theoretical work was carried out using density functional theory [12], as implemented in the Vienna ab initio simulation program (VASP) [13,14]. The VASP code was applied to four chemically disordered alloys with AFM 3Q configurations with 24.2 at.% and 36.4 at.% Mn for ternary Fe–Mn–C with 3 at.% C, respectively as well as 25.0 at.% and 37.5 at.% Mn for binary Fe–Mn. This non-collinear AFM configuration is one of the ground state configurations proposed for Mn-rich steels [15,16] and provides a reliable description of the magnetic state to determine the elastic properties of these materials [9]. Even though the DLM approach gives rise to the best description of elasticity of Fe–Mn, it is not straightforward to apply it to alloys which contain interstitial elements. For the VASP simulations the projector augmented wavepotentials in conjunction with the generalized gradient approximation were employed [17]. The following parameters were applied: convergence criterion for the total energy of 0.01 meV, Blöchl corrections [18] for the total energy cut-off of 300 eV, and integration in the Brillouin zone according to Monkhorst-Pack [19] with 5 × 5 × 5 k-points. 2 × 2 × 2 supercells containing 32 atoms were created with randomly arranged positions of Fe and Mn following the special quasi-random structure (SQS) approach [20]. One C atom (3.0 at.%) was placed in the vicinity of Mn atoms at an interstitial position for Fe–Mn–C alloys, thus maximizing the number of Mn–C nearest neighbours, since this is reported to be the preferred lattice position [21]. The SQS implementation via the short-range order (SRO) parameter is available within the locally self-consistent Green's function (LSGF) software package [22,23]. The LSGF code was used to generate SQS supercells. The Warren–Cowley SRO parameter [24] was applied to account for randomness (less than 0.08 within five coordination shells). Electron density distributions were used to study the electronic structure of these AFM random alloys.

4. Results and discussion

The chemical composition of the thin film was analysed along line scans as illustrated in Figs. 1 and 2. The actual positions of the measurements are visualized as black dots. Based on these data the chemical composition was interpolated for the entire composition range. A compositional spread from 1.5 at.% up to 3.0 at.% C is observed in Fig. 1. In Fig. 2 the chemical composition for Fe and Mn is shown. The Fe content varies between 60.7 at.% and 69.8 at.%, while the Mn content lies between 28.0 at.% and 37.5 at.%.

The chemical composition of the bulk samples is given in Table 1.

We continue with discussing the structure. In Fig. 3a the X-ray diffractograms for compositions varying between 1.5 at.% and 2.8 at.% C at a Fe/Mn ratio of ~2.2 are

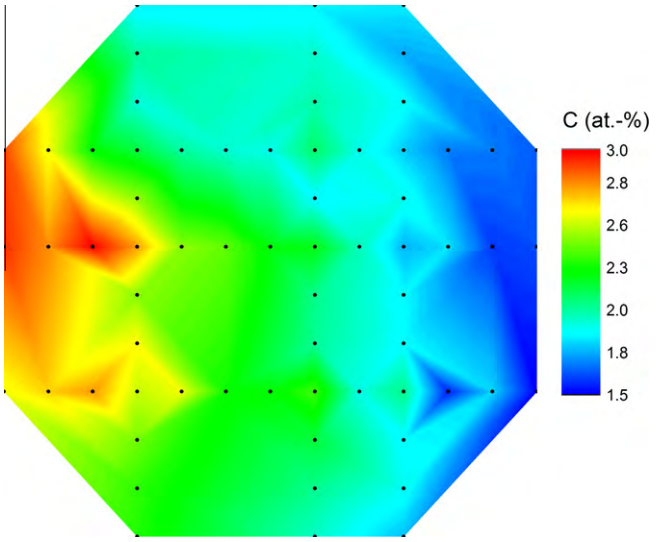

Fig. 1. C content of the thin film with the measured line scans (black dots); sample size is 51 mm diameter.

shown. For comparison the diffractograms reported by Gebhardt et al. [9] are shown in Fig. 3b. These earlier films from Gebhardt et al. [9] were grown without C, covering a Fe/Mn ratio of ~2.3. All peaks can be attributed to fcc structure austenite, indicating that the film is phase pure.

The lattice parameter was evaluated based on three peaks: (1 1 1), (2 0 0) and (2 2 0). Different positions on the combinatorial wafer with 28 at.%, 30 at.%, 33 at.% and 35 at.% Mn were chosen to determine the influence of C on the lattice parameter values. A comparison between the lattice parameter of thin film and bulk samples on the one hand and the VASP calculations on the other hand is shown in Fig. 4. The error bars display the standard deviation of the lattice parameter values. Experimental data for fcc Fe–Mn from Marinelli et al. [25] and for fcc $Fe_{57}Cr_{18}Ni_{15}Mn_{10}$ with additions of C from Gavriljuk et al. [26] as well as calculated data for fcc binary Fe–Mn alloys (DLM configuration) from Music et al. [8] are plotted for comparison. For the thin film the maximum C-induced lattice parameter change is 0.012 Å, corresponding to a 0.33% change in lattice parameter. The lattice parameter of the bulk samples is 3.600 ± 0.005 Å to 3.614 ± 0.001 Å, in the same range as those observed for the thin film, corresponding to a 0.39% change in lattice parameter, even though the Mn content differs. If one compares the average lattice parameter for the fcc ternary Fe–Mn–C thin film with the binary Fe–Mn data of Marinelli et al. [25] and Music et al. [8] the change in lattice parameter is 0.1% and 0.06%, respectively. For both bulk samples and thin film the effect of C on the lattice parameter is marginal. An influence of impurities (sum of all impurity elements is 0.4 at.%, see Table 1) on the lattice parameter of the bulk samples could not be observed for the composition range investigated here.

Ledbetter and Austin [27], Gavriljuk et al. [26], Shanina et al. [28] and von Appen and Dronskowski [21] reported a

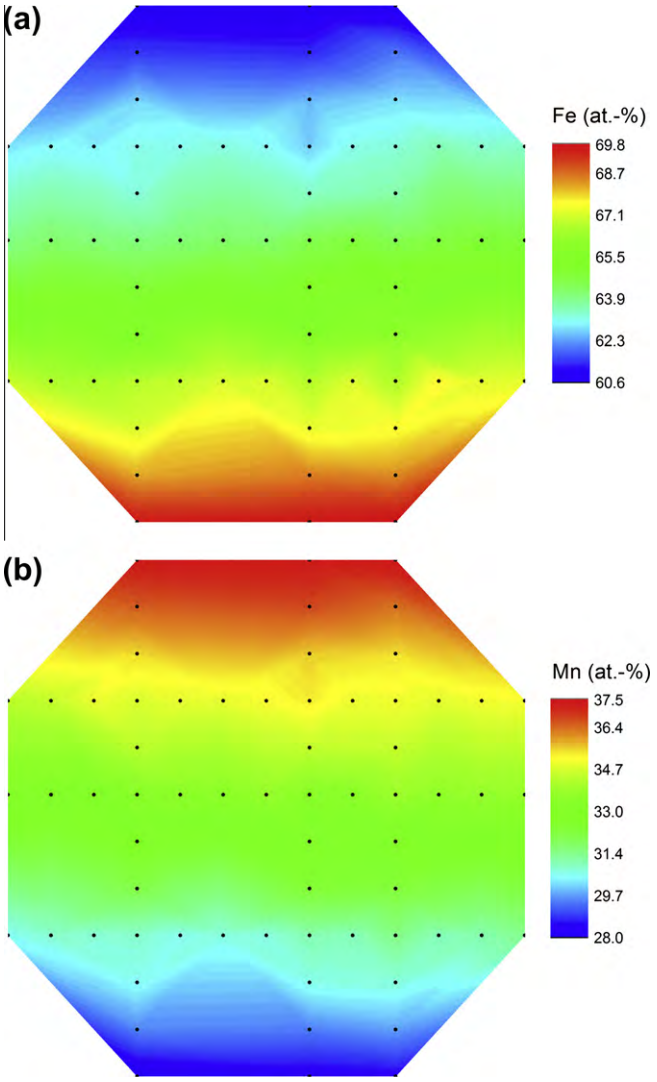

Fig. 2. Compositional spread of the thin film with the measured line scans (black dots) for (a) iron and (b) manganese content; sample size is 51 mm diameter.

lattice expansion caused by the incorporation of C into fcc iron-based alloys, but in each case only a small effect could be ascertained. Gavriljuk et al. [26] detected a lattice expansion of 0.008 Å, corresponding to a 0.22% change in lattice parameter with 2.1 at.% C in $Fe_{57}Cr_{18}Ni_{15}Mn_{10}$. Shanina et al. [28] reported an increase in the lattice parameter of 0.2% with 3.7 at.% C in $Fe_{56}Cr_{18}Ni_{16}Mn_{10}$, while the other authors did not quantify the reported increase in lattice parameter. Hence, the data reported here are consistent with the literature.

The ab initio calculations were carried out using the VASP code (AFM 3Q) for two different Fe/Mn ratios with a C content in the range between 0 and 3 at.%. The calculated data predict a small lattice expansion of 0.016 Å for 25 at.% Mn and 0.015 Å for 37.5 at.% Mn due to the addition of 3 at.% C. The lattice parameters predicted by the ab initio data underestimate the experimental data by $\leqslant 2\%$. For calculation results for configurations that are void of

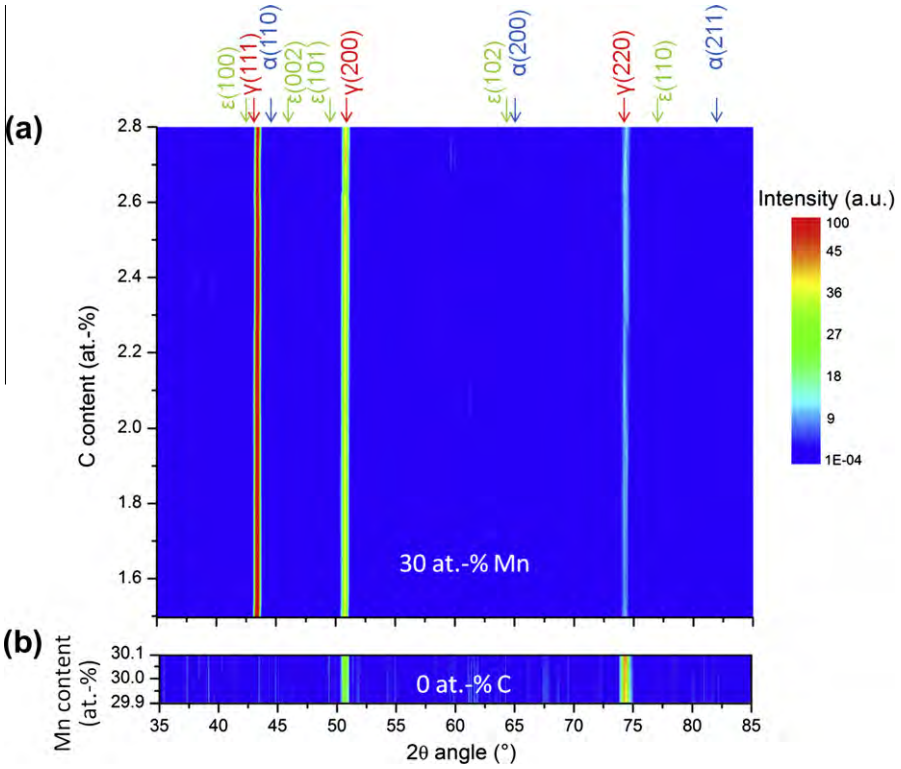

Fig. 3. Phase evolution of thin films vs. (a) C content for Fe/Mn of ~2.2 from this work and (b) Mn content for 0 at.% C taken from the data of Gebhardt et al. [9].

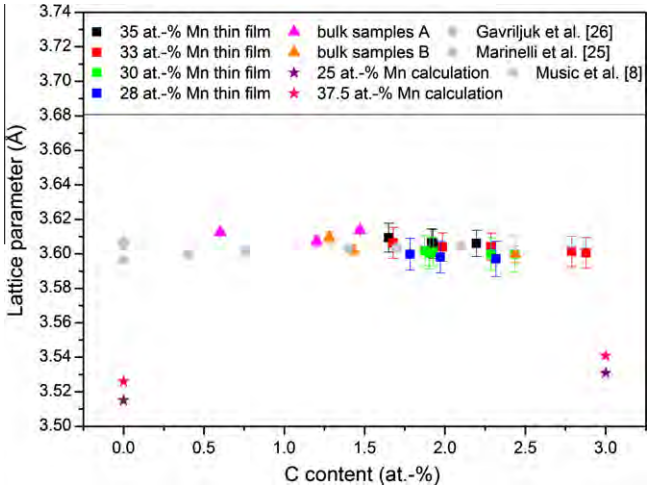

Fig. 4. Lattice parameter as a function of the C content for thin film (rectangles), bulk samples (triangles) and calculations (stars).

interstitial C the DLM method employed by Music et al. [8] yields good agreement with the experiments. It is evident that for the ternary system Fe–Mn–C, the experimental data are consistent with the theoretical predictions.

The crystallographic texture was analysed for the bulk and thin film samples. The EBSD measurements imply that the major phase is austenite for all samples. The microstructure of the samples A consists only of a few large grains: A1 exhibits an average grain size of ~2 mm, sample A2 of ~3 mm and sample A3 of ~5 mm. Most grains exhibit a subgrain structure stemming from solidification. The crystal orientations do not show any preference. The polished surfaces which were later used for modulus determination by nanoindentation show a large variety of different crystallographic surface normals. The samples of type B show average grain sizes which are much smaller than those of samples of type A: 106 μm for B1 and 70 μm and 60 μm for B2 and B3, respectively. They reveal a weak mixed copper-brass-type hot rolling texture with a maximum orientation density of about three times random (calculated via harmonic series expansion to a maximum rank of 34). This texture leads to a very slight preference of the [0 1 1] crystal direction parallel to the surface normal on the longitudinal cross-sections. These sections have been used to perform nanoindentation tests. This very weak preferred crystal direction should not significantly bias the results obtained from the nanoindentation on these surfaces. Sample A1 exhibits, besides the prevalent austenite phase, also hexagonal ε-martensite and tetragonal α′-martensite at the outer rim. Sample B3 shows ε-martensite at the outer rim. The martensite formation is in the current case caused by plastic deformation during manufacturing [29]. All experiments of the bulk samples were performed in the sample centre, where only the austenite phase was present. This ensures a meaningful comparison of the results obtained from the different bulk samples and those from the thin film. The grain scale texture information may be required for the correct interpretation of the nanoindentation results, especially for comparing the bulk data to the thin

film load–displacement indentation results in addition to the consideration of the chemical composition. Due to the small grain size of ~200 nm on average only 43% of the measured area on the thin film could be quantified with sufficient fidelity by EBSD. 99.8% of these indexable patterns indicate the presence of the austenitic phase; only 0.2% correspond to ε-martensite. The texture of the thin film has a slight preference in [0 0 1] and [1 0 2] crystal direction parallel to the surface normal. This very weak preferred crystal direction is expected not to influence the results obtained from the nanoindentation measurements.

The mechanical properties of the thin film and bulk samples were measured by nanoindentation. The resulting Young's modulus values for the thin films, bulk samples and calculations are plotted in Fig. 5 vs. the C concentration. The error bars show the standard deviation of the Young's modulus values. In Fig. 5a the measurements of the as-deposited thin film are shown, while in Fig. 5b the experimental data of the polished thin film are plotted. The average Young's modulus values of the as-deposited and polished thin films are in the same range, while the error bars are drastically reduced due to polishing. Calculated data (DLM configuration) of fcc Fe–Mn with an Fe/Mn ratio of 2.33 from Gebhardt [30] and experimental fcc $Fe_{60}Mn_{40}$ single-crystal data from Cankurtaran et al. [10] are plotted for comparison and are in a good agreement with both the experimental and theoretical data discussed here. For the thin films the Young's modulus values are between 188 and 251 GPa, while for the bulk samples these values range from 185 to 220 GPa. Both bulk sample types have similar Young's modulus values, even though samples B contain different levels of impurities. Thus, the impurities do not affect the Young's modulus within the compositional range based on the nanoindentation measurements. The Young's modulus values for the as-deposited thin films scatter by 24.6%. This is caused by the higher roughness value of the as-deposited thin film in comparison with the roughness of the polished bulk samples. Even though there are large error bars for the as-deposited thin film, the average Young's modulus values for thin film and bulk samples appear to agree rather well.

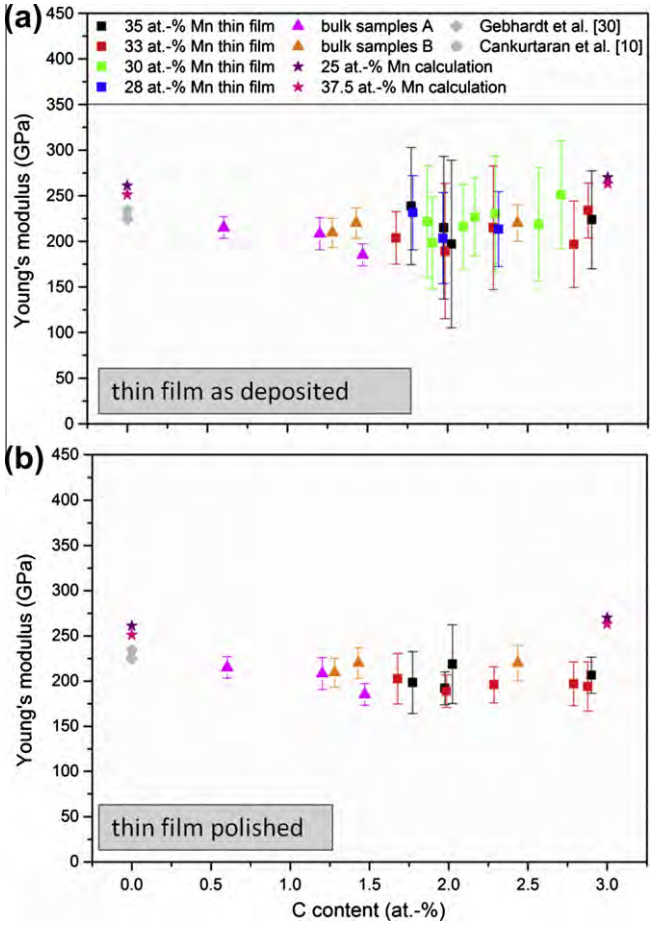

Fig. 5. Young's modulus as a function of C content for thin film (rectangles) and bulk samples (triangles) and calculations (stars) for (a) as-deposited thin film and (b) polished thin film.

Despite the different crystallographic textures and grain sizes of the bulk samples A and B, the experimental Young's moduli taken from the samples are similar. This may be due to the fact that the elastic anisotropy may not be quantified well using nanoindentation because during indentation in all directions of polycrystalline material the stiffness will be averaged [31,32]. The calculated elastic anisotropy of binary Fe–Mn with 37.5 at.% Mn and ternary Fe–Mn–C with 36.4 at.% Mn and 3 at.% C was 0.15 and 0.14, respectively. Thus, the change in elastic anisotropy with C addition is with 6.7% marginal.

Ledbetter and Austin [27] reported that a Young's modulus value reduced by 0.3% due to a 0.14–0.39 at.% C addition. This rather minute change is not quantifiable in the current indentation experiments. Hence, the current data are consistent with those in the literature, specifically in Ref. [27].

The VASP calculations of the elastic properties were conducted for four different compositions, see Fig. 5. These predicted values differ by 15–22% from the average experimental data at 3 at.% C for the as-deposited and polished thin film. Eriksson [33] reported that the calculated elastic properties can be determined within ~15% accuracy in comparison with the experiments. As the C concentration is increased to 3 at.%, the corresponding calculated Young's modulus increases by ~4%. While this increase is significant, it is too small to be verified in the current indentation experiments. Hence, the C changes considered in this work seem to have only a marginal influence on the overall Young's modulus values of fcc Fe–Mn–C alloys. This can be understood by considering the C-induced changes in the electronic structure.

In order to correlate the Young's modulus values with the electronic structure, we study the electron density distribution for the Fe–36.4 at.% Mn–3 at.% C alloy in comparison with the binary Fe–25 at.% Mn alloy in the crystallographic (0 0 4) plane of the fcc lattice structure (see Fig. 6). For the ternary Fe–Mn–C alloy the C atoms are located at the edges, while Fe and Mn are randomly

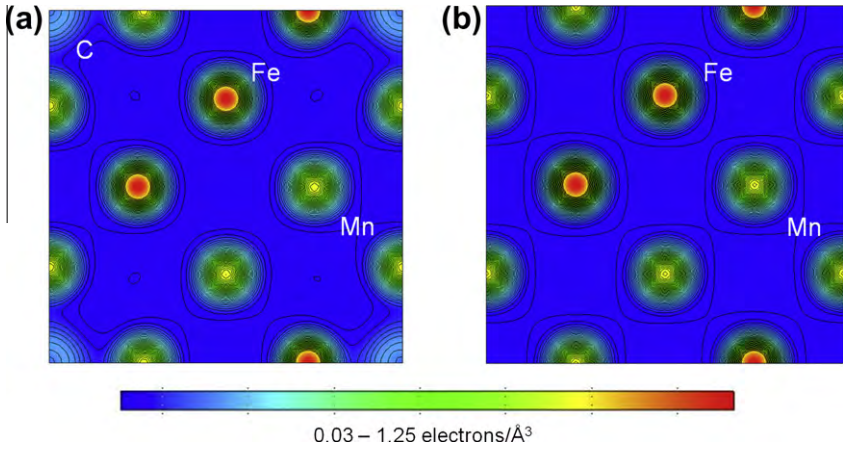

Fig. 6. Electron density distribution of (a) Fe–36.4 at.% Mn–3 at.% C and (b) Fe–25 at.% Mn in the (004) plane.

distributed at fcc sites within the SQS approach. The electron density never reaches zero in this plane, implying uniform distributions of charge between the metallic atoms. On the other hand, electrons are shared between C and the metals. Hence, the electronic structure can be described as a mixture of covalent (Fe–C and Mn–C) and metallic (Fe–Fe, Mn–Mn, Fe–Mn) bonding. According to von Appen and Dronskowski [21] the covalent bond is very strong, but it is not the most abundant one (3 at.% C in the Fe–Mn matrix). In other words, incorporation of C into the metallic matrix only leads to local effects so that no substantial changes in the electronic structure occur. Hence, C does not affect the Young's modulus to a larger extent in the concentration range investigated. This supports the presented experimental results.

5. Conclusions

The influence of the C and Mn concentration for austenitic Fe–Mn–C thin film and bulk samples on the Young's modulus and the equilibrium volume has been studied. Ab initio calculations have been carried out for selected alloy compositions using the VASP code. The calculated elastic property and equilibrium volume data were compared with experimental data to critically evaluate the reliability of the current design strategy for Fe–Mn–C alloys.

The experimental lattice parameter values vary in the whole composition range with C concentrations of 0–3 at.% by 0.017 Å. Hence, there is no significant dependence of the lattice parameter on the C concentration observed. The ab initio calculations predict that C expands the lattice slightly by 0.4% as compared to the binary metallic matrix. The ab initio calculations deviate by $\leqslant 2\%$ from the experiments and are hence in good agreement.

The C concentration does not have a significant influence on the Young's modulus of Fe–Mn–C alloys for the studied composition range. The measured Young's modulus values scatter for the polished thin film between 188 ± 18 GPa and 218 ± 43 GPa and for the bulk samples between 185 ± 12 GPa and 220 ± 20 GPa. The calculated Young's modulus values are 15–22% larger than the average Young's modulus values of the as-deposited and polished thin film at 3 at.% C. The Young's modulus values are in the same range for the as-deposited and polished thin film, while the experimental error is reduced on average from ~26% to ~13% as a result of polishing. The measured data for thin films and bulk samples as well as the calculated data reveal no significant influence of the C concentration on the Young's modulus. This is consistent with the observation of the absence of substantial changes in the electronic structure upon incorporation of C into the metallic matrix.

The thin film reproduces very well the properties of the bulk materials. Both thin film and bulk samples are probed in the austenite phase; lattice parameter data and Young's modulus values are in good agreement.

An influence of impurities of the bulk samples B could not be determined within the composition range investigated.

Thus both the presented implemented simulation strategy and the experimental approach are useful to predict and study the equilibrium volume and the Young's modulus of Fe–Mn–C alloys.

Acknowledgements

The authors gratefully acknowledge the financial support of the Deutsche Forschungsgemeinschaft (DFG) within the Collaborative Research Center (SFB) 761 "Steel – ab initio". The bulk samples A were provided by A. Lob from the Institute of Ferrous Metallurgy, RWTH Aachen University.

References

[1] Frommeyer G, Brüx U, Neumann P. ISIJ Int 2003;43:438.
[2] Gutierrez-Urrutia I, Raabe D. Acta Mater 2011;59:6449.
[3] Grässel O, Kruger L, Frommeyer G, Meyer LW. Int J Plast 2000;16:1391.
[4] Allain S, Chateau JP, Bouaziz O, Migot S, Guelton N. Mater Sci Eng A 2004;387:158.

[5] Bäumer A, Jimenez JA, Bleck W. Int J Mater Res 2010;101:705.
[6] Gutierrez-Urrutia I, Zaefferer S, Raabe D. Scr Mater 2009;61:737.
[7] Gutierrez-Urrutia I, Zaefferer S, Raabe D. Mater Sci Eng A 2010;527:3552.
[8] Music D, Takahashi T, Vitos L, Asker C, Abrikosov IA, Schneider JM. Appl Phys Lett 2007:91.
[9] Gebhardt T, Music D, Ekholm M, Abrikosov IA, von Appen J, Dronskowski R, et al. Acta Mater 2011;59:1493.
[10] Cankurtaran M, Saunders GA, Ray P, Wang Q, Kawald U, Pelzl J, et al. Phys Rev B 1993;47:3161.
[11] Oliver WC, Pharr GM. J Mater Res 1992;7:1564.
[12] Hohenberg P, Kohn W. Phys Rev B 1964;136:864.
[13] Kresse G, Hafner J. Phys Rev B 1993;48:13115.
[14] Kresse G, Hafner J. Phys Rev B 1994;49:14251.
[15] Schulthess TC, Butler WH, Stocks GM, Maat S, Mankey GJ. J Appl Phys 1999;85:4842.
[16] Spisak D, Hafner J. Phys Rev B 2000;61:11569.
[17] Kresse G, Joubert D. Phys Rev B 1999;59:1758.
[18] Blöchl PE. Phys Rev B 1994;50:17953.
[19] Monkhorst HJ, Pack JD. Phys Rev B 1976;13:5188.
[20] Zunger A, Wei SH, Ferreira LG, Bernard JE. Phys Rev Lett 1990;65:353.
[21] von Appen J, Dronskowski R. Steel Res Int 2011;82:101.
[22] Abrikosov IA, Niklasson AMN, Simak SI, Johansson B, Ruban AV, Skriver HL. Phys Rev Lett 1996;76:4203.
[23] Abrikosov IA, Simak SI, Johansson B, Ruban AV, Skriver HL. Phys Rev B 1997;56:9319.
[24] Cowley JM. J Appl Phys 1950;21:24.
[25] Marinelli P, Baruj A, Guillermet AF, Sade M. Z Metallkd 2000;91:957.
[26] Gavriljuk VG, Sozinov AL, Balanyuk AG, Grigoriev SV, Gubin OA, Kopitsa GP, et al. Metall Mater Trans A 1997;28:2195.
[27] Ledbetter HM, Austin MW. Mater Sci Eng 1985;70:143.
[28] Shanina BD, Gavrilyuk VG, Konchits AA, Kolesnik SP, Tarasenko AV. Phys Status Solidi A – Appl Res 1995;149:711.
[29] Verbeken K, Van Caenegem N, Raabe D. Micron 2009;40:151.
[30] Gebhardt T, Music D, Kossmann D, Ekholm M, Abrikosov IA, Vitos L, et al. Acta Mater 2011;59:3145.
[31] Kooi BJ, Poppen RJ, Carvalho NJM, De Hosson JTM, Barsoum MW. Acta Mater 2003;51:2859.
[32] Nix WD. Mater Sci Eng A 1997;234:37.
[33] Eriksson O. Encyclopedia of materials: science and technology. Amsterdam: Elsevier; 2006.

Available online at www.sciencedirect.com

SciVerse ScienceDirect

Acta Materialia 60 (2012) 4005–4016

Acta MATERIALIA

www.elsevier.com/locate/actamat

Evolution of strength and microstructure during annealing of heavily cold-drawn 6.3 GPa hypereutectoid pearlitic steel wire

Y.J. Li [a,b,*], P. Choi [b], S. Goto [c], C. Borchers [a], D. Raabe [b,*], R. Kirchheim [a,b]

[a] Institut für Materialphysik, Georg-August-Universität Göttingen, Friedrich-Hund-Platz 1, D-37077 Göttingen, Germany
[b] Max-Planck Institut für Eisenforschung, Max-Planck-Str. 1, D-40237 Düsseldorf, Germany
[c] Department of Materials Science and Engineering, Faculty of Engineering and Resource Science, Akita University, Tegata Gakuencho, Akita 010-0852, Japan

Received 28 January 2012; received in revised form 1 March 2012; accepted 3 March 2012

Abstract

Hypereutectoid steel wires with 6.35 GPa tensile strength after a cold-drawing true strain of 6.02 were annealed between 300 and 723 K. The ultrahigh strength remained upon annealing for 30 min up to a temperature of 423 K but dramatically decreased with further increasing temperature. The reduction of tensile strength mainly occurred within the first 2–3 min of annealing. Atom probe tomography and transmission electron microscopy reveal that the lamellar structure remains up to 523 K. After annealing at 673 K for 30 min, coarse hexagonal ferrite (sub)grains with spheroidized cementite, preferentially located at triple junctions, were observed in transverse cross-sections. C and Si segregated at the (sub)grain boundaries, while Mn and Cr enriched at the ferrite/cementite phase boundaries due to their low mobility in cementite. No evidence of recrystallization was found even after annealing at 723 K for 30 min. The stability of the tensile strength for low-temperature annealing (<473 K) and its dramatic drop upon high-temperature annealing (>473 K) are discussed based on the nanostructural observations.

Keywords: Pearlitic steel; Ultrahigh strength; Atom probe tomography; Annealing; Grain boundary segregation

1. Introduction

Cold-drawn, hypereutectoid pearlitic steel wires show maximal tensile strength above 5 GPa [1], thus making them the strongest bulk nanostructured materials. Although pearlite has a large potential in engineering applications, the microstructural origin of its extreme strength is not well understood. It has been shown by several authors that cold drawing not only strengthens pearlite by refining the lamellae structure [2–5], but also simultaneously causes partial chemical decomposition of cementite [6–18] and a structural transition from crystalline to amorphous cementite [9,13,14]. The deformation-induced decomposition and microstructural change of cementite is closely related to several other phenomena, such as a strong redistribution of carbon and other alloy elements like Si and Mn in both cementite and ferrite; a variation of the deformation accommodation at the phase interfaces due to a change in the carbon concentration gradient at the interfaces; mechanical alloying; and a further reduction of the deformability of cementite when rendered amorphous. Since these phenomena occur at the atomic scale, the understanding of the strengthening mechanisms of cold-drawn hypereutectoid pearlitic wires can only be improved on the basis of atomic-scale investigations.

Taking a first step in this direction, we recently studied the redistribution of carbon in ferrite and cementite in ultrahigh-strength pearlitic steel wires for a wide range of (true) drawing strains between 0 and 6.02 using atom probe

* Corresponding authors. Address: Max-Planck Institut für Eisenforschung, Max-Planck-Str. 1, D-40237 Düsseldorf, Germany. Tel.: +49 211 6792853; fax: +49 211 6792333.
E-mail addresses: y.li@mpie.de (Y.J. Li), d.raabe@mpie.de (D. Raabe), rkirch@ump.gwdg.de (R. Kirchheim).

1359-6454/$36.00
http://dx.doi.org/10.1016/j.actamat.2012.03.006

tomography (APT) [17,18]. In ferrite, we found that the carbon concentration increases with the drawing strain up to 3.47 and then saturates with further deformation. We found evidence of the formation of dislocation (sub)grain boundaries in the ferrite lamellae and observed the segregation of carbon at ferrite dislocations and (sub)grain boundaries. In cementite, we found that the carbon concentration decreases with the thickness of the cementite lamellae. This finding gives a quantitative correlation between plastic deformation and cementite decomposition in cold-drawn pearlitic steel wires [17,18]. Furthermore, both the saturation of the carbon content in the ferrite and the discontinuation of further decomposition of cementite at high strains indicate the important role of dislocations during cementite decomposition. This is also supported by the direct observation of carbon segregation at ferrite dislocations and grain boundaries [17,18].

Nanostructured materials produced by severe plastic deformation are highly susceptible to grain coarsening upon heating, due to the large density of dislocations and grain boundaries. However, little attention has been paid so far to the thermal stability of the nanostructure of heavily cold-deformed pearlitic wires [9,19–21] and its effect on the mechanical properties. In this work, we study the changes in the nanostructure of a heavily cold-drawn hypereutectoid pearlitic steel wire upon annealing in order to elucidate the mechanism leading to the ultrahigh strength of cold-drawn pearlitic steel wires. The wires studied here were subjected to the most extreme deformation by cold drawing to a true drawing strain of $\epsilon = 6.02$ and exhibit the highest tensile strength achieved to date (6.35 GPa). The tensile strength was measured as a function of the annealing temperature between 423 and 723 K and of the annealing time. The samples were characterized by means of APT in conjunction with transmission electron microscopy (TEM). APT yields three-dimensional elemental maps with near-atomic resolution. This technique is a key to the current study as it allows us to identify the carbon distribution in the drawn and heat-treated pearlite samples [16,22–28]. A local electrode atom probe (LEAP 3000X HR^{TM}, Cameca Instruments) was used, which provides a larger field of view, faster data acquisition rates and higher mass resolution [29–32] compared to conventional atom probes and thus yields compositional data with high accuracy. We surprisingly observed hexagonal (sub)grains in ferrite after annealing, where carbon is segregated to (sub)grain boundaries and spheroidized cementite particles are preferentially located at triple junctions. In addition, the redistribution of other alloying elements, such as Si, Mn and Cr, upon annealing is also quantified and discussed from the viewpoint of the kinetic barriers in terms of the differences in diffusion coefficients between the two abutting phases (ferrite and cementite). On the basis of our experimental observations, we discuss the influence of annealing temperature T and time, and also of the alloying elements and their respective redistribution on the drop in tensile strength upon heat treatment.

2. Experimental

2.1. Material and experimental methods

The material studied in this work was a pearlitic steel wire of hypereutectoid composition (Fe–0.98C–0.31Mn–0.20Si–0.20Cr–0.01Cu–0.006P–0.007S in wt.% and Fe–4.40C–0.30Mn–0.39Si–0.21Cr–0.003Cu–0.01P–0.01S in at.%), provided by Suzuki Metal Industry Co., Ltd. The as-deformed wires were in a cold-drawn state, with a true strain of $\epsilon = 6.02$. Samples taken from this material were annealed for 30 min between 423 and 723 K, at 50 K intervals. Tensile strength, APT and TEM measurements were taken on the as-deformed and annealed wires. The tensile strength was measured with a Dia Stron LEX 810 device using an initial strain rate of $\dot{\epsilon}_0 = 1.16 \times 10^{-3}$ s^{-1}.

The local electrode atom probe was used to analyze the nanostructural changes and the three-dimensional (3-D) elemental distributions upon annealing. The measurements were performed in voltage mode at 70 K, with a pulse fraction of 15%, a pulse repetition rate of 200 kHz and a detection rate of 0.005 atoms per pulse. APT samples perpendicular to the wire axis were prepared using a dual-beam focused ion beam (FEI Helios NanoLab 600TM) according to the procedure described in Ref. [15]. Reconstructions of the APT data were made using standard parameters for the image compression factor (1.65) and the evaporation field (33 V nm^{-1}), with an efficiency of the detector of 0.37. The final specimen tip radii (after APT measurements) were also taken into account for the reconstructions. TEM samples were prepared using the focused ion beam lift-out method. The sample preparation was done with 30 kV Ga ions, finishing the last step with 5 kV Ga ions. We used a Philips CM30 instrument at an acceleration voltage of 300 kV.

2.2. Mass spectrum analyses of atom probe data

The assignment of ion peaks in a mass spectrum of cold-drawn pearlitic steel wire has been addressed previously [8,15,18]. A mass spectrum of an annealed wire with an initial drawing strain of 6.02 is shown in Fig. 1a. All peaks due to Fe, alloy elements (C, Si, Cr and Mn) as well as impurities like P and S are assigned. As reported in Refs. [17,18] for cold-drawn wires, the mass spectra of ferrite (Fig. 1b) and cementite (Fig. 1c) also reveal the presence of the peak at 24.5 Da in cementite only, which means that 100% of the peak at 24 Da is due to C_2^+ in the ferrite, while a mixture of ions from C_2^+ and C_4^{2+} in the cementite contribute to this peak. A peak deconvolution algorithm (supplied by the software IVAS, Cameca Instruments) taking into account the isotope ratios of C was applied to the peak at $m/n = 24$ Da. The result shows that less than 50% of the peak is due to C_4^{2+} in the cementite, while for the cold-drawn wires the contribution from C_4^{2+} exceeds 80% [17]. It is reported that the fractions of carbon molecular ions change with the APT acquisition conditions, e.g. temperature,

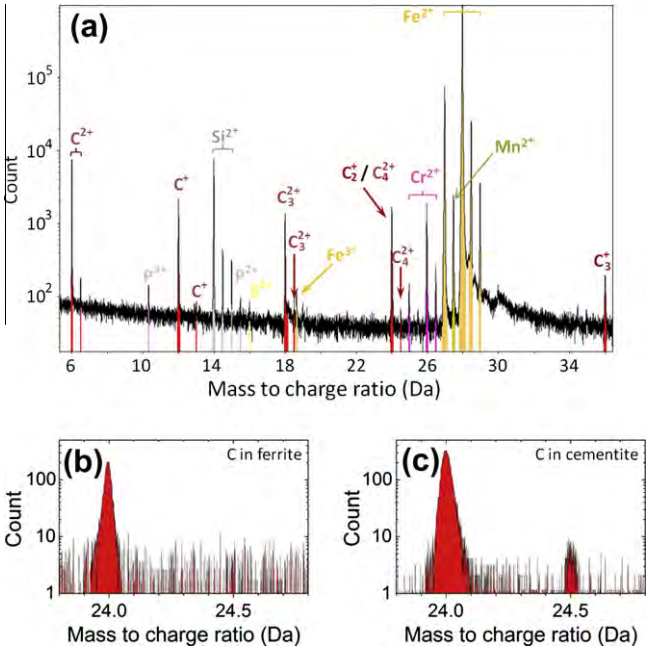

Fig. 1. (a) Mass spectrum of a cold-drawn ($\epsilon = 6.02$) wire after annealing at 673 K for 30 min. Peaks ascribed to C, Si, Cr, Mn and Fe are marked in red, gray, pink, green and yellow, respectively. (b and c) Mass spectra for ferrite and cementite, respectively. Note the presence of the peak of 24.5 Da only in the cementite.

pulse fraction and evaporation rate [33]. It might be possible that the different material states (e.g. deformed and annealed) also influence the ratio of field-evaporated carbon molecules. As C_2^+ mainly contributes to the peak at 24 Da according to the peak deconvolution analysis, this peak was assigned as C_2^+ for atom maps of the annealed samples.

3. Results

3.1. Evolution of tensile strength upon annealing

Fig. 2 shows the tensile strength as a function of the annealing temperature. At room temperature the as-deformed material exhibits a tensile strength of 6.35 GPa, which, to the best of our knowledge, makes it the strongest pearlitic steel wire available today. The ultrahigh tensile strength remains after annealing at 423 K for 30 min. Beyond this temperature, the tensile strength decreases approximately linearly with the annealing temperature. The evolution of the tensile strength with annealing time shown in Fig. 3 indicates that the dramatic drop in tensile strength mainly occurs within the first 2–3 min of the annealing process. After this short time interval, the tensile strength remains approximately constant at a relatively low temperature of 523 K. Even for the highest temperature of 723 K, the tensile strength decreases only slightly with further annealing time. This suggests that the underlying structural changes take place during the early annealing stage. The large circles in Figs. 2 and 3 mark the annealing conditions

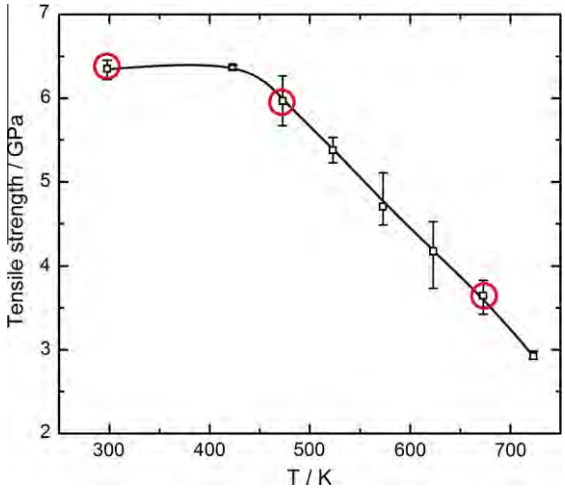

Fig. 2. Tensile strength as a function of annealing temperature for an annealing time of 30 min for cold-drawn hypereutectoid pearlitic steel wires. The red circles mark the annealing conditions for which APT measurements were performed.

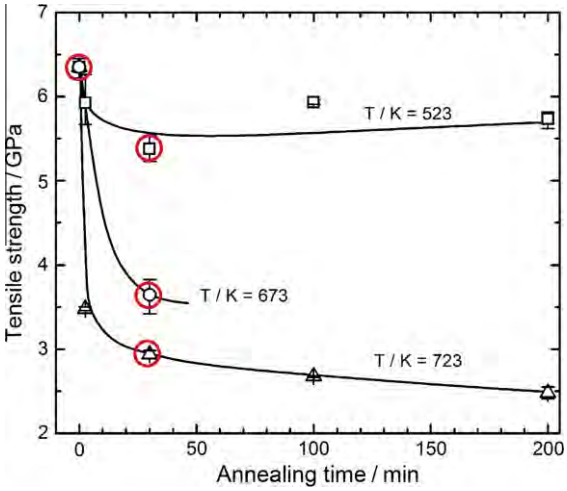

Fig. 3. Tensile strength as a function of annealing time at various temperatures for cold-drawn hypereutectoid pearlitic steel wires. The red circles mark the annealing conditions for which HRTEM studies were performed.

under which the nanostructure and the distribution of alloy elements in the deformed and annealed wires were studied by APT and high-resolution (HR) TEM.

3.2. Evolution of microstructure upon annealing

APT results on the as-deformed and the 473 K and 673 K heat-treated states are displayed in Fig. 4. The atom maps of the as-deformed material (Fig. 4a) clearly show that a lamellar structure consisting of carbon-depleted (ferrite) and -enriched (cementite) regions still prevails after severe cold-drawing up to a strain of 6.02, although fragmentation of cementite lamellae can be observed. The lamellar structure remains stable after annealing at 473 K for 30 min (Fig. 4b). No cementite spheroidization occurs.

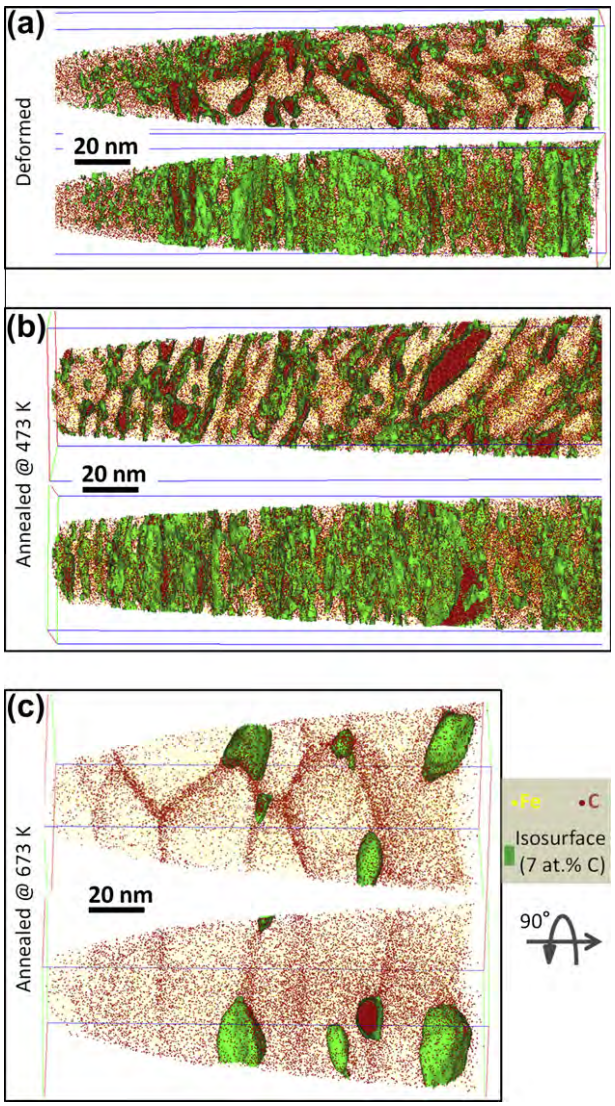

Fig. 4. 3-D carbon atom maps of hypereutectoid pearlitic steel wires with a cold drawing strain of $\epsilon = 6.02$: (a) as-deformed state; (b) annealed at 473 K for 30 min; and (c) annealed at 673 K for 30 min. The isoconcentration surfaces for 7 at.% carbon are shown in green. Only 30% of all carbon and 0.5% of all iron atoms are displayed. Both the cross-sectional (top) and longitudinal views (bottom) of the wires are shown.

However, Languillaume et al. observed speroidized cementite particles at 473 K [19]. Since the alloy elements, the initial strain and the annealing time of the pearlitic wire studied in Ref. [19] were different from those studied in this work, it is difficult to analyze the exact reasons for the different observations.

After heat treatment at 673 K for 30 min, strong microstructural changes occur. The original lamellar pearlitic structure is no longer visible; instead, a nearly equiaxed hexagonal (sub)grain structure has formed inside the ferrite (see Fig. 4c). The (sub)grain boundaries enclosing the carbon-depleted ferrite (sub)grains are decorated with carbon atoms. The (sub)grains exhibit an average grain size of 30–40 nm, which is about 2–3 times higher than the interlamellar spacing in the as-deformed wire [17,18]. Furthermore, the cementite lamellae have undergone spheroidization and are mainly located at the triple junctions. Similar observations were made by TEM for pearlitic steel wires at true drawing strains of 3.5 after annealing for 1 h at 823 K [19], 4.22 for 1 h at 673 K [9] and 5 for 0.5 h at 723 K [20]. Closer observation of Fig. 4c shows that the grains are not equiaxed but, rather, elongated along the drawing direction, with longitudinal sizes above 70 nm. It is noted that the reconstruction of the APT data shown in Fig. 4c was done based on the final tip radius after APT measurement, and is hence reliable. This observation suggests that the relatively coarse (sub)grain structure observed in the ferrite is not due to recrystallization, as this mechanism would lead to equiaxed grains.

Fig. 5 shows TEM micrographs of pearlitic wires for the corresponding conditions marked in Fig. 3. Strong strain contrast due to heavy drawing can be observed from Fig. 5a. The phase boundaries between ferrite and cementite are blurred and nearly invisible. The observation in the cross-section of the wire (Fig. 5b) shows the typical curled ribbon-like lamellar structure around the wire axis [3,34,35]. As explained by Hosford [36], the $\langle 1\,1\,0 \rangle$ fiber texture developed during wire drawing confines further slipping in each lamella to a plain strain state, and thus the compatibility of the neighboring grains can be maintained only by the bending of the grains around one another. This mechanism is referred to as curling [36–38]. The observation of fragmentation of cementite in Fig. 5b is consistent with the APT result shown at the bottom of Fig. 4a, where the cementite lamellae are curled and fragmented into numerous short segments and even small particles. This is direct evidence that cementite lamellae are capable of undergoing plastic deformation and even strain-induced fragmentation, as reported in Ref. [2,3]. Upon annealing at 523 K for 30 min, the lamellar structure is still preserved and no recrystallization occurs (Fig. 5c).

After annealing at 723 K (see Fig. 5d), the lamellar structure along the drawing direction is still visible, while cell/subgrain boundaries have formed in the ferrite and the cementite lamellae have undergone spheroidization. The ferrite cell/subgrains are elongated along the wire axis, in agreement with the APT observation at 673 K (Fig. 4c). In the direction perpendicular to the wire axis, the average subgrain size is below 80 nm.

3.3. Redistribution of carbon during annealing

Fig. 6 illustrates the carbon partitioning among the various phases or regions (ferrite, cementite and interface region) in the as-deformed and annealed samples, where the bulk carbon concentration is plotted against the cumulative (phase) volume fractions. In accordance with our previous works [17,18], the phases of ferrite and cementite, and the interface between them, are defined according to their carbon content (see also caption of Fig. 6), where the volume fraction of each phase can be estimated as the ratio of the total number of atoms in each phase to the total

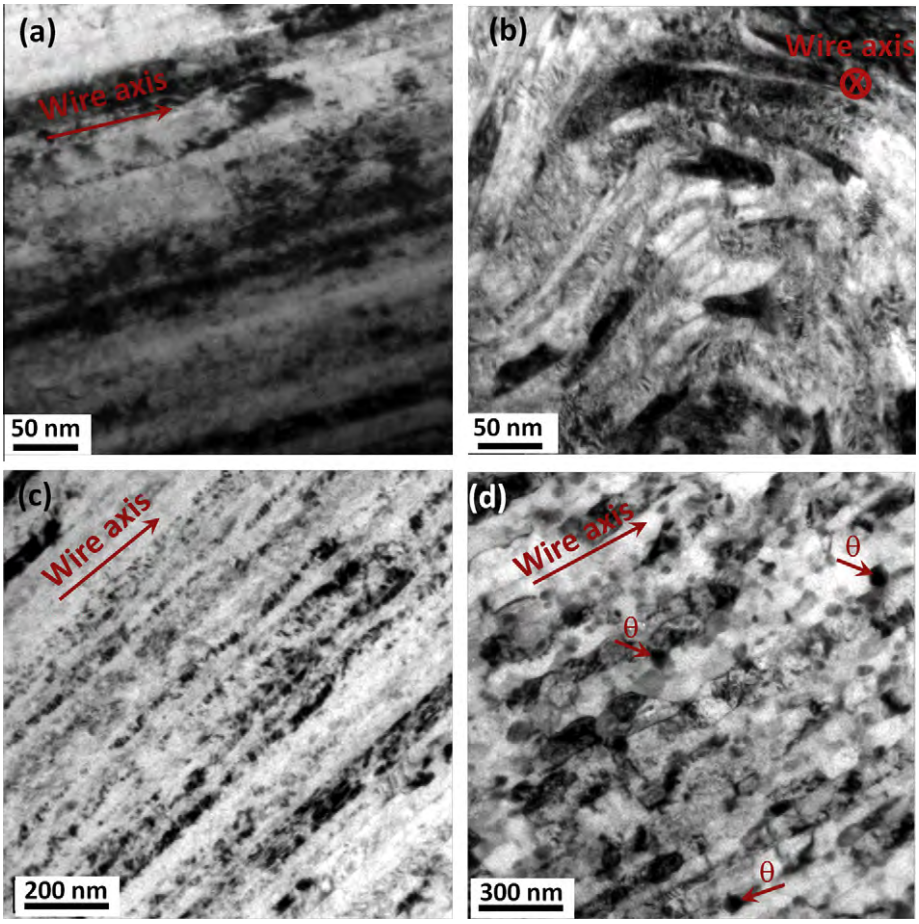

Fig. 5. TEM images of hypereutectoid pearlitic steel wires. (a and b) As-deformed ($\epsilon = 6.02$) states in longitudinal and transverse cross-sections of wires, respectively. (c and d) As-annealed states at 523 and 723 K for 30 min, respectively. The arrows mark the wire axis which is also parallel with the ferrite/cemetite interfaces. Some globular cementite particles (θ) are marked.

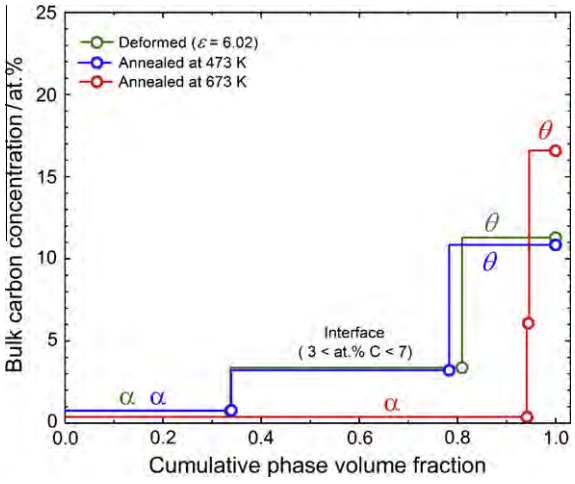

Fig. 6. Bulk carbon concentrations in the defined phase zones vs. volume fractions of the corresponding phase zones. Ferrite (α) and cementite (θ) are defined as the regions with carbon concentrations lower than 3 at.% and higher than 7 at.%, respectively. The region between the two phases is defined as the ferrite/cementite interface.

number of atoms in the whole sample. The result shows that, in the as-deformed sample, the carbon concentration of 0.73 ± 0.006 at.% in the ferrite is far beyond the equilibrium value of several tens of atom ppm, while the carbon concentration in the cementite decreases to approximately half of the stoichiometric value. In addition, the large volume fraction of the interface characterized by an extended carbon concentration gradient suggests dissolution of carbon atoms from cementite to ferrite and a mechanical alloying process. After annealing at 473 K for 30 min, no significant redistribution of carbon atoms is found, since both the carbon concentrations and the volume fractions of all phases remain close to the values measured in the as-deformed sample.

A dramatic change in the redistribution of carbon occurs after annealing at 673 K for 30 min. As shown in Fig. 6 (red curve), the high volume fraction of the ferrite/cementite interface produced during extreme deformation decreases greatly after annealing. The bulk carbon concentration in ferrite is reduced to 0.37 ± 0.003 at.% and the carbon concentration in the cementite of 16.6 ± 0.013 at.% approaches the stoichiometric value. We observe that the volume fraction of ferrite after annealing at 673 K even exceeds the value of 85% (for C wt.% = 0.98), as expected from the lever rule. This is due to the fact that a limited size

of the probed volume confines the statistics in determining the phase volume fractions. However, this limit has little influence on the accuracy of the concentration measurement in each individual phase region.

Note that 16.6 at.% is not the carbon concentration in the center of the cementite particles, but the average one in the defined region (see caption of Fig. 6). As will be shown in Section 3.4, the carbon concentration inside these particles reaches 25 at.% after annealing at 673 K for 30 min. Both the dark-field image and the HRTEM result shown in Fig. 7 demonstrate the crystallinity of the cementite particle that may form during annealing at $T \geqslant 673$ K. However, its transformation mechanism upon high-temperature annealing is complicated in the present case due to the uncertainty of the existence of lamellar cementite before annealing. If the cementite undergoes only a partial chemical (not structural) decomposition before annealing, then the formation of cementite particles upon annealing proceeds without nucleation; instead, it is driven simply by the reduction of the ferrite/cementite phase boundary area.

3.4. Grain boundary excess of carbon after annealing at 673 K

Fig. 4 shows that carbon atoms segregate at the ferrite (sub)grain boundaries at 673 K. By using the sub-cutting method [17], the average carbon concentration inside the ferrite grains was measured to be 0.163 ± 0.057 at.% (see the dotted lines in Fig. 8f and g), while it exceeds 1.5 at.% at the grain boundaries (Fig. 8f and g). Two regions of interest cutting through the spheriodized cementite are selected for the analysis of the carbon concentration. The measured values of about 25 at.% C (Fig. 8h and i) show that the carbon concentration in cementite has reached the stoichiometric value again.

It is known that segregation of solute atoms at grain boundaries decreases the grain boundary energy, as described by the Gibbs adsorption isotherm [39–41],

$$d\gamma = -\Gamma_A d\mu_A \quad (1)$$

where γ is the specific grain boundary energy, Γ is the excess amount of A atoms at the boundary and μ_A is the chemical potential of the solute atoms of type A. This means that the higher the solute excess at the grain boundary, the lower the grain boundary energy.

$\Gamma^{\alpha}_{C,gb}$, the grain boundary excess of carbon, can be determined either from 1-D concentration profiles (e.g. Fig. 8f and g) or by direct counting of the number of carbon atoms per grain boundary area. With the former method, the carbon concentration in (sub)grain interiors (as shown by the dotted lines in Fig. 8f and g) is subtracted from the measured concentrations. Using the latter method, the number of carbon atoms within the selected region, e.g. "GI" in Fig. 8a, is subtracted from the number of carbon atoms in region "GB", which has the same size as the domain "GI". By using the two methods, $\Gamma^{\alpha}_{C,gb}$ is determined to be (5.30 ± 0.73) atoms nm^{-2} $(8.80 \times 10^{-6}$ mol m$^{-2})$ and (5.14 ± 0.72) atoms nm^{-2} $(8.54 \times 10^{-6}$ mol m$^{-2})$, respectively.

According to Eq. (1), a carbon excess of $\approx 9 \times 10^{-6}$ mol m^{-2} reduces the grain boundary energy and thus reduces the driving force for grain coarsening, even when annealing the heavily cold-drawn pearlitic steel sample at 723 K. The stabilization of defects such as grain boundaries and dislocations by solute segregation, known as the defactant concept [39–41], has also been reported in Refs. [42–45].

3.5. Redistribution of Si, Mn and Cr during annealing at 673 K

Fig. 9a–d shows the atom maps of Si, Cr, Mn and C (as a reference), respectively, in the wire annealed at 673 K for 30 min. To quantify the distribution of the solute atoms, concentration profiles along a domain $10 \times 2 \times 83$ nm^3 in size, as shown in Fig. 9d, were plotted in Fig. 9f. Corresponding atom maps within the inspected region are shown in Fig. 9e. In accordance with the carbon distribution shown in Fig. 9e, the carbon concentration reaches a maximum in the center of a cementite particle and at the grain boundaries in ferrite, respectively, and has a minimum in the grain

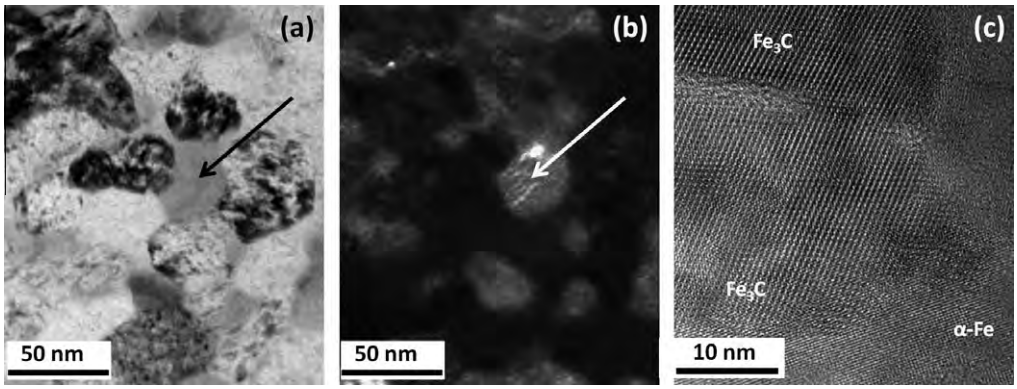

Fig. 7. (a) TEM bright-field and (b) dark-field images in the transverse cross-section of a hypereutectoid pearlitic wire after annealing at 673 K for 30 min. A distinct contrast line in the form of bright lines in one cementite particle marked with an arrow indicates a crystalline particle. (c) HRTEM image of a wire after annealing at 723 K for 30 min, showing a crystalline cementite particle in the ferrite matrix.

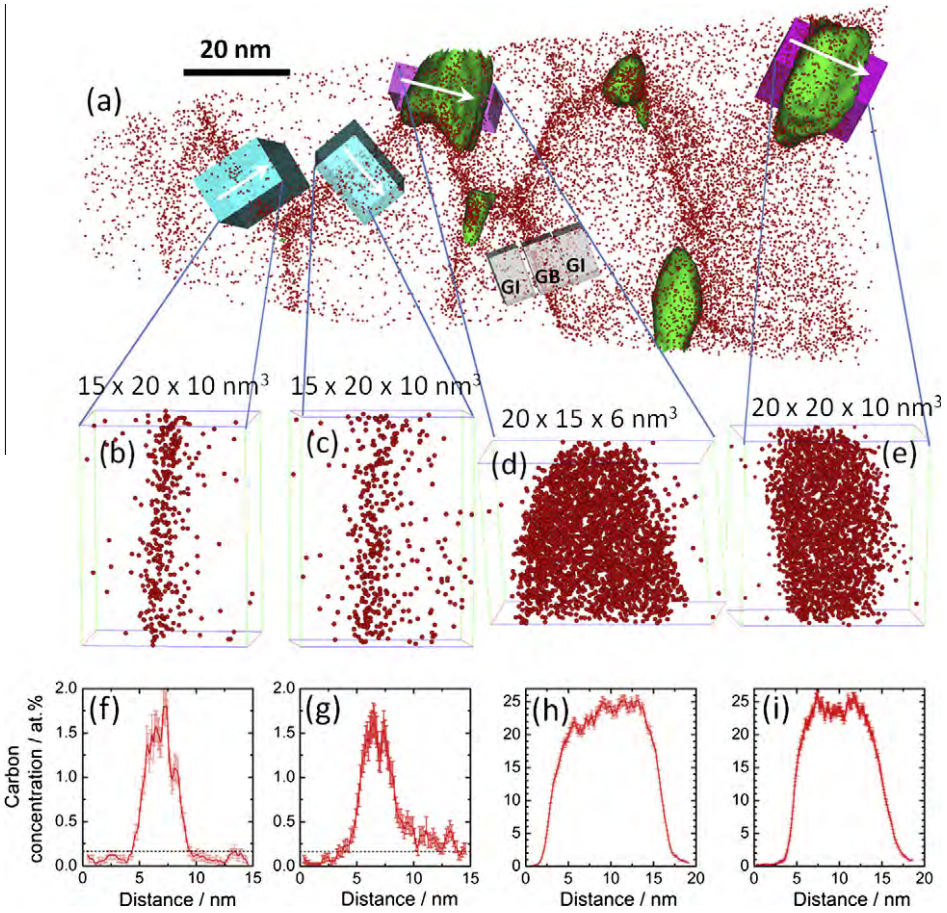

Fig. 8. (a) Carbon atom map of the annealed (673 K for 30 min) hypereutectoid pearlitic steel wire with selected regions of interest (ROIs). The white arrows mark the directions along which the concentration profiles are drawn. The gray-colored ROIs containing grain boundary (GB) and grain interior (GI) are shown as an example for determining the grain boundary excess of carbon (see text). (b–e) Carbon atom maps for the ROIs. The corresponding 1-D carbon concentration profiles are displayed below each atom map (f–i).The average carbon concentration inside the ferrite grains is displayed as short-dashed lines in (f) and (g).

interior (see Fig. 9e). Si is also segregated at the subgrain boundaries (see Fig. 9a and f), where the maxima and minima of the Si concentration correspond well to the locations of subgrain boundaries and subgrain interiors, respectively. The absolute minimum of Si at the center of the cementite particle is consistent to the diminishing equilibrium solubility of Si in cementite as calculated by Thermo-Calc (see Table 1). Cr and Mn atoms are strongly segregated in cementite (see Fig. 9b, c and e). In the grain interior we also observed a depletion of Cr and Mn atoms next to some subgrain boundaries (see the arrows in Fig. 9c). This suggests twofold kinetics in the redistribution of the alloy elements during annealing. One process is the diffusion of Cr and Mn atoms from the subgrain interior to the subgrain boundary inside the ferrite, which leads to Cr- and Mn-depleted areas next to the subgrain boundaries. In the second process, the subgrain boundaries supply a fast diffusion path along which Cr and Mn atoms can quickly diffuse to triple-junction lines, where the spheroidized cementite particles are located owing to the higher vacancy flux along subgrain boundaries. In addition, the distribution of Cr and Mn atoms in cementite is also inhomogeneous (see Fig. 9b, c and e top). The concentration profiles of Cr and Mn in Fig. 9f show a double plateau (see arrows), located at the ferrite/cementite phase boundaries.

4. Discussion

4.1. Thermal stability of microstructure and strength upon annealing below 473 K

The ultrahigh strength remained stable after the material was annealed at temperatures below 473 K for 30 min (see Fig. 2). This observation is consistent with the analyses of the as-deformed and annealed wires by APT (see Fig. 4a and b). The TEM image in Fig. 5c shows that the lamellar structure still remains even after annealing at 523 K. We conclude that no substantial microstructural change has taken place during annealing at temperatures below 473 K.

One can argue that some softening might already occur due to a slight recovery at the relatively low annealing temperatures. However, this could be compensated by static strain aging during low-temperature annealing or even during the storage of the cold-deformed material at room temperature. The net effect from these two phenomena is that the strength remains unchanged. This argument can

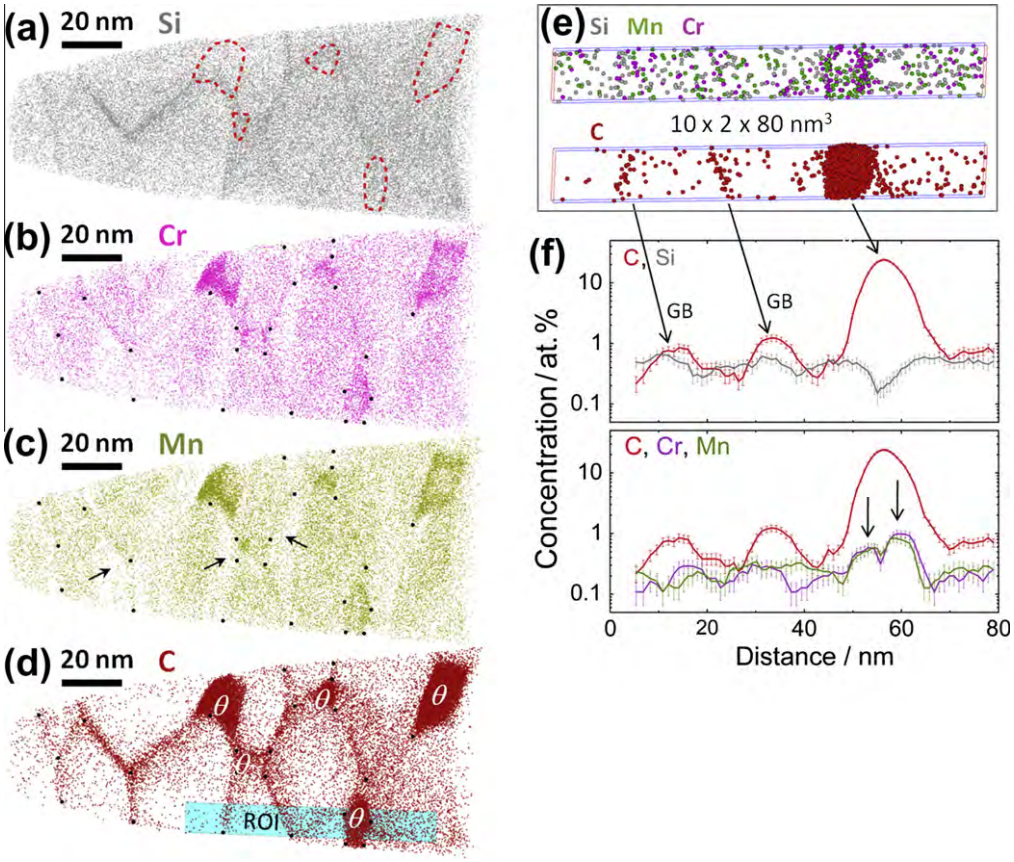

Fig. 9. 3-D atom maps of Si, Cr, Mn and C of a sample annealed at 673 K. 100% of Si, Cr and Mn and 30% of the carbon atoms are displayed. Cementite is labeled with "θ". The red dashed borders in (a) and the black dots in (b) and (c) mark cementite particles and grain boundaries shown in (d), respectively. The 1-D concentration profiles along the ROI chosen in (d) are shown in (f).

Table 1
Solubilities of Si, Mn and Cr in ferrite and cementite under equilibrium conditions calculated by Thermo-Calc using the nominal composition of the wire given in Section 2 (unit: at.%).

Temperature (K)	Si		Mn		Cr	
	Ferrite	Cementite	Ferrite	Cementite	Ferrite	Cementite
473	0.46	0	1.39×10^{-3}	1.81	1.37×10^{-4}	1.24
673	0.46	0	1.86×10^{-2}	1.73	3.27×10^{-3}	1.225

be further discussed as follows: before measuring the tensile strength (both at room temperature and after the various heat treatments), the as-cold-drawn wires were kept at room temperature for about 6 months. The carbon diffusion distance can be estimated as $x = \sqrt{6Dt}$ by taking the bulk diffusivity $D_\alpha^C = D_{0,\alpha}^C \cdot \exp\left(\frac{-Q}{RT}\right)$ ($D_{0,\alpha}^C = 2 \times 10^{-6}$ m^2 s^{-1} and $Q = 84.1$ kJ mol^{-1} [46], R is the gas constant) of carbon in ferrite. This rough estimate yields a carbon diffusion distance of 650 nm in ferrite at room temperature for $t = 0.5$ year and an additional 300 nm at 423 K for 30 min. This estimate shows that carbon can diffuse to dislocations within the fine ferrite lamellae. However, our recent results show that strain aging becomes less significant with increasing wire strain. For a true strain of 6.02 the strain aging effect is barely noticeable. This means that for weakly drawn wires some carbon atoms have not diffused sufficiently to decorate dislocations even after a storage period of 6 months at room temperature. However, they can diffuse to dislocations upon annealing for only 30 min. This implies an overestimation of the carbon diffusion length at room temperature, possibly due to the supersaturation of the ferrite with carbon upon cold drawing. We attribute the absence of strain aging upon high-temperature annealing for highly strained pearlitic wires ($\epsilon > 5$) to the slightly higher temperature that occurs during drawing as compared to weakly strained wires. This effect facilitates the strong segregation of carbon to single dislocations in the case of highly strained ferrite during the drawing process [17,18]. The effect limits the free sites at dislocations that remain for carbon decoration during static storage at room temperature or annealing at elevated temperatures. Moreover, the

density of single dislocations decreases with further drawing due to the formation of ferrite dislocation cell/substructures which are also decorated with carbon [17,18].

4.2. Recovery and recrystallization during annealing above 473 K

Both the APT (Fig. 4c) and TEM (Fig. 5d) observations show that the elongated ferrite grains inherited from cold drawing still exist after annealing at 673 and 723 K for 30 min. These results suggest that no recrystallization occurs, since recrystallization typically yields equiaxed grains. Furthermore, after annealing at 673 K for 30 min, the carbon content in the ferrite amounts to 40 times the equilibrium value of 0.001 wt.% C at room temperature. This indicates an existence of lattice defects such as vacancies, dislocations and (sub)grain boundaries in the ferrite because these types of defects are able to supply additional sites to trap a large amount of carbon atoms [14,17,18,21]. This means that a typical entirely defect-free recrystallized structure has not yet been formed after annealing at 673 K for 30 min. In addition, the slight (sub)grain structure coarsening in ferrite indicates that recovery rather than recrystallization takes place during annealing because the observed grain size remains far below the typical recrystallized grain size, which is in the micrometer range.

The inhibition of recrystallization in the most heavily cold-deformed ($\epsilon = 6.02$) pearlitic wire can be attributed to the strong fiber texture [3,35], which reduces the driving force for recrystallization and decreases the mobility of grain boundaries by forming low-angle grain boundaries (one dominant grain orientation). Embury and Fisher [2] reported that the misorientation between the ferrite cells is of the order of 1° at a true drawing strain of 3.1. Tarui et al. [47] also confirmed the formation of a cell structure in the ferrite of pearlite at $\epsilon = 4.2$ by selected-area electron diffraction. In addition, the segregation of carbon at the cell/subgrain boundaries and the spheroidized cementite may also inhibit the recrystallization by reducing the grain boundary energy and pinning the grain boundaries against migration, respectively. Also, primary recrystallization proceeds through a nucleation and growth sequence, and the confined interlamellar spacing might be too small for a critical nucleus size to be reached. Thus, we suggest that the formation of cell/subgrain structures after annealing at temperatures above 473 K results not from recrystallization, but from strong recovery of the deformed microstructure.

4.3. Softening during annealing above 473 K

Based on the discussion above, the dramatic drop in tensile strength upon annealing at temperatures above 473 K seems to be mainly due to static recovery of the deformed microstructure through annihilation, rearrangement or polygonization of ferrite dislocations. Readers are referred to Ref. [18] for the mechanism of formation of (sub)grain structure inside the ferrite channel. In addition, the other microstructural changes upon annealing, such as cementite spherodization, redistributions of alloy elements, recovery of point defects (vacancies and interstitials) and relatively slight coarsening of cell/subgrain structures, may also cause the drop in tensile strength, as discussed below in more detail.

4.3.1. Recovery of dislocations at cell/subgrain boundaries

Severe plastic deformation such as cold drawing introduces a high dislocation density into the material. Recently, Zhang et al. [48] reported that the dislocation density ρ in the ferrite lamellae increases from $7.5 \times 10^{13}\ \mathrm{m}^{-2}$ in the as-patented state to $2 \times 10^{16}\ \mathrm{m}^{-2}$ after a cold-drawing strain of 3.68. Chen and Kirchheim [49] measured the dislocation density in an annealed pearlitic (0.8 wt.% C) steel wire produced by cold drawing to $\epsilon = 3$. They found that the dislocation density decreases to $8.53 \times 10^{14}\ \mathrm{m}^{-2}$ after annealing at 723 K for 30 min. While it is not clear how the recovery process occurs, it is very likely in the current system that dislocation recovery takes place mainly at the ferrite/cementite interfaces. For the materials studied in the present work, the lamellar spacing decreases to about 10 nm, thus the major portion of the dislocations created during cold drawing becomes stored at the interface between ferrite and cementite, where they form cell/grain boundaries superimposing on the phase boundaries [18]. Meanwhile, due to the decomposition of cementite, the dislocations from neighboring ferrite may meet at the sites of the original cementite and form a dipolar configuration. Together with an enhanced diffusion process along the phase interface due to severe plastic deformation, a fast annihilation of the dislocation dipoles during annealing becomes feasible. One may note that the quick drop of the tensile strength in the first few minutes during annealing agrees well with the feature of dipole annihilation, as suggest by Hausselt and Blum [50]. We estimate the reduction of the dislocation density on the basis of the drop of the tensile strength by calculating the change of the athermal stress due to the dislocations after annealing:

$$\Delta\sigma_{\mathrm{G}} = \alpha M G b\left(\sqrt{\rho_0} - \sqrt{\rho(T,t)}\right) \tag{2}$$

where α is the dislocation interaction constant, M is the Taylor factor, G is the shear modulus at ambient temperature, b is the length of the Burgers vector, ρ_0 is the dislocation density for the as-deformed state and $\rho(T, t)$ is the dislocation density for the as-annealed state. As a first estimate, we use $\alpha = 0.35$, $M = 3.06$, $G(300\ \mathrm{K}) = 8.2 \times 10^4$ MPa [51] and $b = 0.25$ nm, and the dislocation densities of the above-mentioned measurements. This yields a reduction of the athermal stress of 2.5 GPa by taking the measured dislocations densities of $2 \times 10^{16}\ \mathrm{m}^{-2}$ for as-deformed wire [48] and $8.53 \times 10^{14}\ \mathrm{m}^{-2}$ for the wire annealed at 723 K for 30 min [49]. We ignore the possibility of relaxation of the dislocation stress field due to the segregation of carbon atoms at dislocation cores. While this value explains a major part of the strength reduction of 3.4 GPa at 723 K (Fig. 2), one should also consider possible effects associated with other microstructural changes.

4.3.2. Cell/subgrain coarsening during annealing

In the preceding section we discussed that the reduction of strength during annealing can be explained in terms of recovery of dislocations at cell/grain boundaries. As demonstrated by Blum and Zeng [52], the dislocation density in ultrafine-grained materials is closely related to the grain size since dislocations are mainly stored at grain boundaries. Here, as an alternative approach, we may directly describe the relationship between the strength and the (sub)grain size. From Figs. 4 and 5, the initial (sub)grain size d_0 can be roughly estimated to be 10 nm, and the size values $d(T)$ in the transverse direction of the wires are about 30 and 70 nm after annealing at 673 and 723 K, respectively. The corresponding strengths before (σ_0) and after (σ_T) annealing read 6.35, 3.64 and 2.92 GPa (see Fig. 2), respectively. The annealing apparently leads to coarsening of the grain structure, which consequently degrades the strength of the material. These data can be approximated by a Hall–Petch-type relationship:

$$\sigma_0 - \sigma_T = k_{H-P}\left(d_0^{-0.5} - d(T)^{-0.5}\right) \quad (3)$$

with $k_{H-P} \approx 550$ MPa $\mu m^{0.5}$. It has been frequently reported that the Hall–Petch slope in steels increases with the carbon concentration [53], in particular with the carbon concentration at grain boundaries [54–57]. Although a direct comparison of the carbon concentration-dependent k_{H-P} values between our measurement and the literature data is difficult because of the large scatter of the latter data sets [54–57], our measured value falls reasonably within the commonly observed range of $k_{H-P} = 315 \sim 760$ MPa $\mu m^{0.5}$ for steels with carbon segregation at ferrite grain boundaries [55,58].

4.3.3. Spheroidization of cementite

Steels containing pearlitic microstructures have higher strength and hardness than those with spherical cementite because the latter materials have a smaller area fraction of heterointerfaces. In the present case, it is hard to quantify the reduction of tensile strength resulting from the loss of phase boundary density due to cementite spheroidization. During annealing at temperatures above 473 K, the reduced phase boundaries are replenished by cell/subgrain boundaries. The question arises how effective the cell/subgrain boundaries are as barriers to dislocation motion. Together with the spheroidization of cementite, the ferrite cell/subgrain structure continuously coarsens during annealing. Hence, it is difficult to distinguish the softening effects resulting from the loss of phase boundaries from that associated with coarsening of the cell/subgrain structure. The estimate shown in Section 4.3.2 indicates the importance of the cell/subgrain size in the ferrite for the strength of pearlite.

4.3.4. Reduction of solid solution hardening

The loss of solid solution hardening due to the transport of solute atoms from the ferrite to the (sub)grain boundary as well as to cementite during annealing also leads to softening. A loss of carbon solid solution hardening between 300 and 673 K can be estimated by

$$\Delta\sigma_{sol} = k\left(\sqrt{C_{300}} - \sqrt{C_{673}}\right) \quad (4)$$

where k is a prefactor ($\approx 1.12 \times 10^4$ MPa for carbon in Fe [59]) and C_{300} and C_{673} are the carbon concentrations in weight percent in the ferrite after annealing at 300 and 673 K, respectively, for 30 min. Based on the values of 0.75 at.% (0.167 wt.%) for C_{300} and 0.16 at.% (0.036 wt.%) for C_{673} measured by APT, $\Delta\sigma_{sol}$ amounts to only 240 MPa. This means that the loss of solid solution hardening due to the redistribution of carbon atoms upon annealing does not play a major role in the reduction of the tensile strength.

The strengthening effect of other alloying elements, like Mn and Cr, is even lower than that of carbon in the ferrite. Therefore, significant softening resulting from the loss of solid solution hardening by Mn and Cr is not expected. On the contrary, these two elements may have a strengthening effect during annealing, as they are found to segregate at the interfaces between ferrite and cementite, and thus suppress the further growth of cementite particles during annealing. Regarding the solid solution effect, Si is known to be even less effective than Mn. Except for its segregation at ferrite gain boundaries, the distribution of Si in the ferrite and cementite upon annealing does not show a significant difference from that in the as-deformed wire (Fig. 10b).

4.4. Redistribution of alloy elements upon annealing

To better understand the elemental redistribution processes during annealing, proximity histograms [32,60] across ferrite/cementite interfaces were analyzed. Fig. 10 shows the proximity histograms of C, Si, Cr and Mn averaged over multiple interfaces in the as-deformed and annealed wires.

As the concentration profiles show little difference before (i.e. the as-deformed state) and after annealing at 473 K, we only compare in more detail the results between the as-deformed state and the state after annealing at 673 K. In the as-deformed state, two effects of the severe deformation on the microstructure can be observed. One is the partial redistribution of carbon from cementite into ferrite; the other is the approximately homogeneous distribution of Cr and Mn among ferrite and cementite compared to the equilibrium values (Table 1), which we attribute to mechanical mixing (see the green curves in Fig. 10(c) for Cr and (d) for Mn). The main reason why Si does not undergo mechanical mixing upon deformation is the insolubility of Si in cementite (see Table 1). In addition, Si is preferentially located at the ferrite grain boundaries, as seen in Fig. 9aa. This might render mechanical mixing phenomena more sluggish.

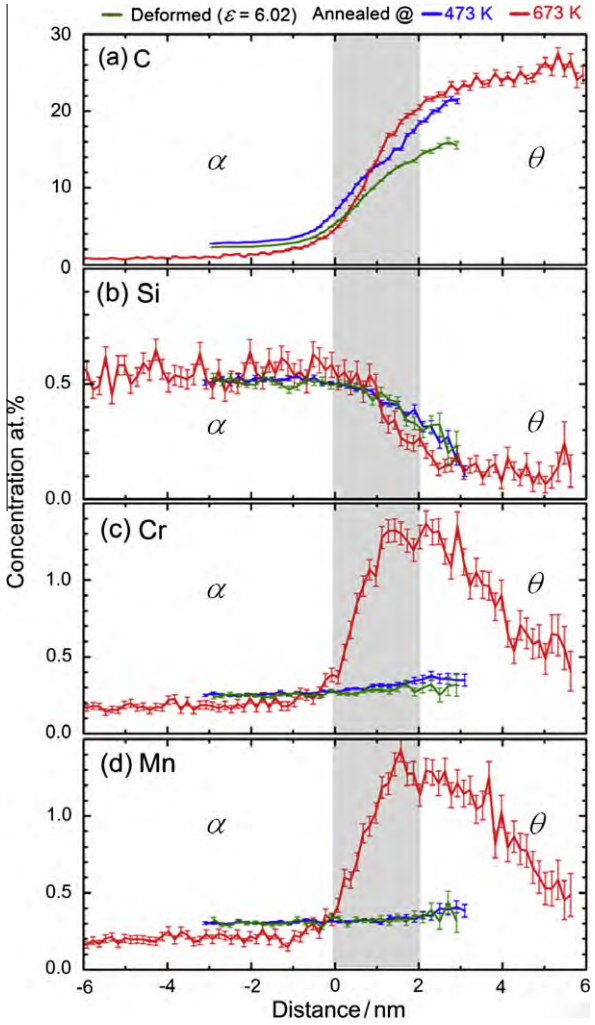

Fig. 10. The proximity histograms [32,60] of (a) C, (b) Si, (c) Cr and (d) Mn obtained from multiple interfaces shown in Fig. 4 for as-deformed (green) and as-annealed states at 473 K (blue) and 673 K (red). Ferrite and cementite separated by the interface (gray zone) are marked with α and θ, respectively.

After annealing at 673 K for 30 min, the alloy elements undergo strong redistribution. First, as shown in Fig. 10a, the reduced carbon content in cementite after deformation returns to the stoichiometric value. It should be mentioned that the carbon concentrations we found in cementite in the as-deformed state are inversely dependent on the thickness of the cementite lamellae [17]. The green curve shown in Fig. 10a is obtained from the analysis of relatively thick cementite lamellae. In addition, the concentration gradient at the interfaces between ferrite and cementite becomes sharper after annealing as compared to the blurred interface in the as-deformed state.

Second, a similar increase in the concentration gradient of Si at the ferrite/cementite interfaces indicates an enhanced redistribution of Si atoms from cementite to ferrite due to annealing (see Fig. 10b). It is noted that the concentration of Si increases monotonically from cementite to ferrite without any sign of enrichment of Si at the ferrite/cementite interface [9,61]. This may be attributed to a low initial Si content in cementite (in the as-deformed state) and the fast diffusivity of Si at ferrite grain boundaries, along which the Si can leave the cementite.

Third, a significant number of Cr and Mn atoms diffuse from ferrite to the interfaces between ferrite and cementite. It is known that Cr and Mn are carbide-forming elements and that their solubilities in cementite are much higher than in ferrite (Table 1), as they can substitute Fe in the carbides and form $(Fe,Cr)_3$ C and $(Fe,Mn)_3C$ [62,63], respectively. As a result, there is a driving force for Cr and Mn to diffuse from ferrite to cementite during annealing. However, the limited diffusivity of these atoms in cementite is likely to act as a kinetic barrier for the fast accommodation of the incoming atom flux from ferrite. According to Ref. [64], the diffusion coefficient of Mn in ferrite D_{α}^{Mn} (2.4×10^{-23} m^2 s^{-1}) is about three orders of magnitude higher than that in cementite D_{θ}^{Mn} (8.8×10^{-27} m^2 s^{-1}). According to Ref. [65], Cr behaves similarly to Mn. In particular, at ferrite grain boundaries the diffusivity of Cr and Mn can be even higher, so that the incoming atoms segregate at the ferrite/cementite interface and result in the concentration peaks we observe here (Fig. 10c and d). A similar scenario was recently reported for a maraging-TRIP steel, where the Mn partitioning at martensite/austenite interfaces is due to the low diffusivity of Mn in the austenite, which does not allow the incoming Mn flux from the adjacent martensite to be accommodated within the austenite [66,67].

5. Conclusions

The micro- and nanostructures of a heavily cold-drawn hypereutectoid pearlitic steel wire were studied by APT and TEM in both the as-deformed and annealed states. The lamellar structure consisting of ferrite and cementite is preserved up to annealing at 473 K, with only small changes in the distribution of the solute atoms. Upon annealing at 673 K, the lamellar structure transforms to a subgrain structure in ferrite, with carbon atoms segregated at the grain boundaries and spheroidized cementite located at the triple junctions inside the ferrite. No evidence of recrystallization was found after annealing up to 723 K. The atom maps and concentration profiles of the solutes suggest that (sub)grain boundaries provide a fast diffusion path, along which Si atoms can diffuse from cementite to ferrite and segregate at ferrite grain boundaries. Cr and Mn diffuse from ferrite to cementite, where a kinetic freezing effect (smaller diffusion coefficient in cementite) for the further diffusion of Cr and Mn deeper into the cementite leads to segregation of Cr and Mn at the phase boundaries between ferrite and cementite. The considerable drop in tensile strength after annealing can be mainly attributed to the recovery of dislocations and coarsening of dislocation substructures. The loss of solid solution hardening due to the redistribution of carbon atoms upon annealing gives only a small contribution.

Acknowledgements

The authors thank Dr. H. Yarita, from Suzuki Metal Industry Co., Ltd., for providing the cold drawn specimens. We also thank Dr. D. Ponge, from Max-Planck Institut für Eisenforschung, Prof. W. Blum, from University of Erlangen-Nürnberg, and Dr. J. Takahashi, from Nippon Steel Corporation, for many valuable discussions, and Dr. A. Kostka for performing TEM. We are grateful to the Deutsche Forschungsgemeinschaft for funding this research (SFB 602 and KI230/34-1).

References

[1] Takahashi T, Ochiai I, Tashiro H, Ohashi S, Nishida S, Tarui T. Nippon Steel Tech Rep 1995;64:45.
[2] Embury JD, Fisher RM. Acta Metall 1966;14:147.
[3] Langford G. Metall Trans A 1977;8:861.
[4] Embury JD, Hirth JP. Acta Metall Mater 1994;42:2051.
[5] Raabe D, Choi P, Li YJ, Kostka A, Sauvage X, Lecouturier F, et al. MRS Bull 2010;35:982.
[6] Belous MV, Cherepin VT. Fiz. Met Metalloved 1961;12:685.
[7] Gridnev VN, Gavrilyuk VG, Dekhtyar IY, Meshkov YY, Nizin PS, Prokopenko VG. Phys Status Solidi A 1972;14:689.
[8] Danoix F, Julien D, Sauvage X, Copreaux J. Mater Sci Eng A 1998;250:8.
[9] Hong MH, Reynolds Jr WT, Tarui T, Hono K. Metall Mater Trans A 1999;30:717.
[10] Sauvage X, Copreaux J, Danoix F, Blavette D. Philos Mag A 2000;80:781.
[11] Hono K, Ohnuma M, Murayama M, Nishida S, Yoshie A. Scripta Mater 2001;44:977.
[12] Wetscher F, Pippan R, Sturm S, Kauffmann F, Scheu C, Dehm G. Metall Mater Trans A 2006;37:1963.
[13] Goto S, Kirchheim R, Al-Kassab T, Borchers C. Trans. Nonferrous Met Soc China 2007;17:1129.
[14] Borchers C, Al-Kassab T, Goto S, Kirchheim R. Mater Sci Eng A 2009;502:131.
[15] Takahashi J, Tarui T, Kawakami K. Ultramicroscopy 2009;109:193.
[16] Sauvage X, Lefebvre W, Genevois C, Ohsaki S, Hono K. Scripta Mater 2009;60:1056.
[17] Li YJ, Choi P, Borchers C, Chen YZ, Goto S, Raabe D, et al. Ultramicroscopy 2011;111:628.
[18] Li YJ, Choi P, Borchers C, Westerkamp S, Goto S, Raabe D, et al. Acta Mater 2011;59:3965.
[19] Languillaume J, Kapelski G, Baudelet B. Acta Mater 1997;45:1201.
[20] Borchers C, Chen Y, Deutges M, Goto S, Kirchheim R. Philos Mag Lett 2010;90:581.
[21] Takahashi J, Kosaka M, Kawakami K, Tarui T. Acta Mater 2012;60:387.
[22] Cerezo A, Godfrey TJ, Smith GDW. Rev Sci Instrum 1988;59:862.
[23] Blavette D, Deconihout B, Bostel A, Sarrau JM, Bouet M, Menand A. Rev Sci Instrum 1993;64:2911.
[24] Miller MK, Cerezo A, Hetherington MG, Smith GDW. Atom probe field ion microscopy. Oxford: Oxford University Press; 1996.
[25] Kelly TF, Miller MK. Rev Sci Instrum 2007;78:031101.
[26] Seidman D. Annu Rev Mater Sci 2007;37:127.
[27] Marquis EA, Miller MK, Blavette D, Ringer SP, Sudbrack CK, Smith GDW. MRS Bull 2009;34:725.
[28] Pereloma EV, Stohr RA, Miller MK, Ringer SP. Metall Mater Trans 2009;40A:3069.
[29] Miller MK. Rev Sci Instrum 2007;78:031101.
[30] Miller MK, Russell KF. Surf Interface Anal 2007;39:262.
[31] Kelly TF, Miller MK. Microsc Res Tech 2006;69:359.
[32] Miller MK, Forbes RG. Mater Charact 2009;60:461.
[33] Takahashi J, Kawakami K, Kobayashi Y. Ultramicroscopy 2011;111:1233.
[34] Langford G. Metall Trans 1970;1:465.
[35] Zelin M. Acta Mater 2002;50:4431.
[36] Hosford Jr WF. Trans AIME 1964;230:12.
[37] Raabe D, Heringhaus F, Hangen U, Gottstein G. Z Metallkd 1995;86:405.
[38] Heringhaus F, Raabe D, Gottstein G. Acta Mater 1995;43:1467.
[39] Kirchheim R. Acta Mater 2002;50:413.
[40] Kirchheim R. Acta Mater 2007;55:5129.
[41] Kirchheim R. Acta Mater 2007;55:5139.
[42] Boylan K, Ostrander D, Erb U, Palumbo G, Aust KT. Scripta Metall Mater 1991;25:2711.
[43] Mehta SC, Smith DA, Erb U. Mater Sci Eng A 1995;204:227.
[44] Farber B, Cadel B, Menand A, Schmitz G, Kirchheim R. Acta Mater 2000;48:789.
[45] Choi P, da Silva M, Klement U, Al-kassab T, Kirchheim R. Acta Mater 2005;53:4473.
[46] Wert CA. Phys Rev 1950;79:601.
[47] Tarui T, Maruyama N, Takahashi J, Nishida S, Tashiro H. Nippon steel technical report no. 91; January 2005.
[48] Zhang X, Godfrey A, Huang X, Hansen N, Liu Q. Acta Mater 2011;59:3422.
[49] Chen YZ, Kirchheim R. Personal communication.
[50] Hausselt J, Blum W. Acta Metall 1976;24:1027.
[51] Frost HJ, Ashby MF. Deformation-mechanism maps. Oxford: Pergamon Press; 1982.
[52] Blum W, Zeng XH. Acta Mater 2009;57:1966.
[53] Nam WJ, Bae CM, Lee CS. J Mater Sci 2002;37:2243.
[54] Wilson DV. Met Sci J 1967;1:40.
[55] Mintz B, He H, Smith GDW. Mater Sci Technol 1992;8:537.
[56] Takeda K, Nakada N, Tsuchiyama T, Takaki S. ISIJ Int 2008;48:1122.
[57] Takahashi J, Kawakami K, Ushioda K, Takaki S, Nakata N, Tsuchiyama T. Scripta Mater 2012;66:207.
[58] Mintz B. Met Technol 1984;11:265.
[59] Gottstein G. Physikalische grundlagen der materialkunde. Heidelberg: Springer-Verlag; 1998.
[60] Hellman OC, Vandenbroucke JA, Rüsing J, Isheim D, Seidman DN. Microsc Microanal 2000;65:437.
[61] Balak J, Sauvage X, Lee DL, Lee CY, Pareige P. Adv Mater Res 2007;26–28:45.
[62] Gurry RW, Christakos J, Darken LS. Trans ASM 1961;53:187.
[63] Schaaf P, Wiesen S, Gonser U. Acta Metall Mater 1992;40:373.
[64] Fridberg J, Trndahl LE, Hillert M. Jernk Ann 1969;153:263.
[65] Barnard SJ, Smith GDW, Garratt-Reed AJ, Vander Sande JB. In: Aaronson HI, Laughlin DE, Sekerka RF, Wayman CM, editors. Proceedings of the international conference on "solid–solid phase transformations". Warrendale (PA): AIME; 1982. p. 881.
[66] Raabe D, Ponge D, Dmitrieva O, Sander B. Scripta Mater 2009;60:1141.
[67] Dmitrieva O, Ponge D, Inden G, Millán J, Choi P, Sietsma J, et al. Acta Mater 2011;59:364.

Available online at www.sciencedirect.com

SciVerse ScienceDirect

Scripta Materialia 68 (2013) 348–353

Scripta MATERIALIA

www.elsevier.com/locate/scriptamat

Viewpoint Paper

Direct evidence for the formation of ordered carbides in a ferrite-based low-density Fe–Mn–Al–C alloy studied by transmission electron microscopy and atom probe tomography

Jae-Bok Seol,[a] Dierk Raabe,[a] P. Choi,[a] Hyung-Seok Park,[b] J.-H. Kwak[c] and Chan-Gyung Park[b,*]

[a] *Max-Planck-Insititut für Eisenforschung, Max-Planck-Str.1, 40237 Düsseldorf, Germany*
[b] *Materials Science and Engineering, POSTECH, Pohang 790-784, Republic of Korea*
[c] *Automotive Steels Research Laboratories, POSCO, Gwangyang 545-711, Republic of Korea*

Available online 17 August 2012

Abstract—We study the structure and chemical composition of the κ-carbide formed as a result of isothermal transformation in an Fe–3.0Mn–5.5Al–0.3C alloy using transmission electron microscopy and atom probe tomography. Both methods reveal the evolution of κ-particle morphology as well as the partitioning of solutes. We propose that the κ-phase is formed by a eutectoid reaction associated with nucleation growth. The nucleation of κ-carbide is controlled by both the ordering of Al partitioned to austenite and the carbon diffusion at elevated temperatures.

Keywords: Lightweight steels; Ordered carbide; Decomposition; Atom probe tomography

1. Introduction

Recent trends in designing advanced high-strength steels aim at controlling the mechanical properties and reducing the specific weight by varying the Mn and Al contents [1–6]. Following this concept, a ferritic-matrix-based Fe–Mn–Al–C alloy with a higher content of Al than Mn was developed [7]. The major benefit behind this alloy design is a weight reduction of ~10% compared to transformation-induced plasticity or twinning induced plasticity steels. The reduction in mass density is due to the high Al content, which also enhances oxidation, corrosion resistance and impact toughness at high temperature [6,8]. These new low-density steels can achieve tensile strengths above 780 MPa and elongations above 30% owing to the formation of the ordered $L'1_2$ κ-carbide, $(Fe,Mn)_3AlC_x$ [8]. The deformation behavior of weight-reduced austenitic Fe–Mn–Al–C alloys is reported to depend on the size, fraction, location and distribution of the κ-phase [9–11]. However, no experimental investigations have so far been made on the compositional gradients across the phase boundaries between κ-carbide and abutting phase, except for an austenitic Fe–(20–30)Mn–Al–C alloy (wt.%) using electron probe microanalysis at the micrometer-scale [12,13]. Moreover, the effects of isothermal annealing on the precipitation of the κ-phase in Fe–Mn–Al–C alloys have not yet been elucidated.

The present study aims at identifying the decomposition mechanism of metastable austenite into ferrite and κ-carbide upon isothermal annealing in high-Al steels from the viewpoint of experiments and thermodynamic calculations. Using transmission electron microscopy (TEM), the present study gives detailed information on κ-carbide, such as crystallographic structure, morphology and orientation relationship with the abutting phases (austenite or ferrite). Another important goal is to reveal the chemical composition of the κ-phase as a function of isothermal annealing temperature using atom probe tomography (APT) and aberration-corrected scanning TEM (STEM).

* Corresponding author. Tel.: +82 54 279 2139; e-mail: cgpark@postech.ac.kr

1359-6462/$ - see front matter © 2012 Acta Materialia Inc. Published by Elsevier Ltd. All rights reserved.
http://dx.doi.org/10.1016/j.scriptamat.2012.08.013

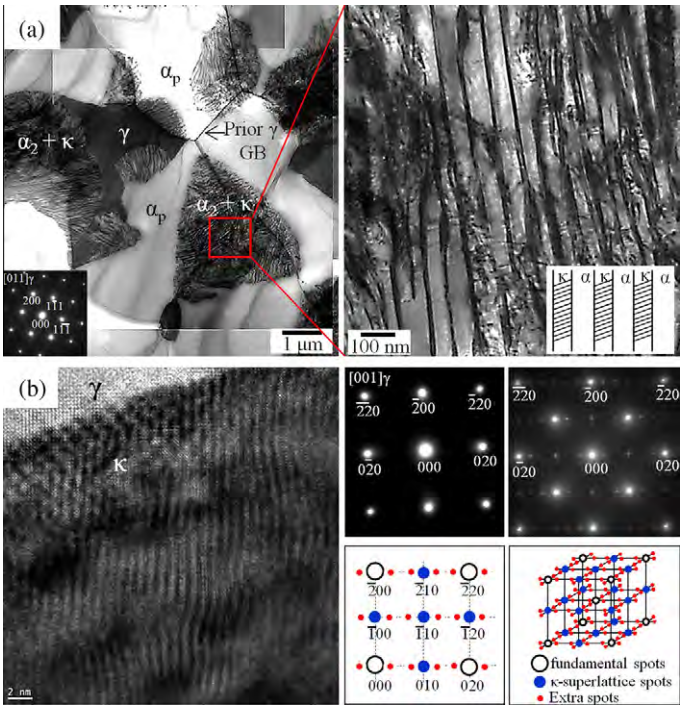

Figure 1. (a) TEM micrographs and the corresponding SADP taken from austenite for the steel subjected to isothermal holding at 500 °C. (b) HREM image and the corresponding SADPs of $[001]_\gamma$ zone including the simulated 2-D and 3-D reciprocal lattice illustrations of the perovskite κ-phase. α_p, polygonal ferrite; α_2, fine ferrite surrounded by carbides; γ, retained austenite; κ, κ-carbide.

2. Experimental procedure

An alloy with the composition 1.2 C, 3.2 Mn and 10.0 Al (at.%) was prepared by vacuum induction melting at 1200 °C for 60 min. Details of the alloy preparation and the thermomechanical processing have been published elsewhere [14]. In the current study, the cold-rolled steels were subjected to a two-step isothermal annealing: intercritical annealing at 900 °C for 30 min in a protective Ar atmosphere followed by isothermal annealing at 500 or 600 °C for 60 min and water quenching. The cooling rate from 900 °C to a desired level of holding temperature was about 150 K s^{-1} [6]. Microstructure characterization was done by TEM (JEM 2010F) and selected-area diffraction pattern (SADP) analysis. The TEM samples were prepared by electrochemical polishing. The lattice parameters of the κ-phase and the austenite were determined by high-resolution TEM (HRTEM). The chemical composition of the κ-phase was determined by energy-dispersive spectroscopy (EDS) on a Cs-corrected STEM (JEM 2100F) and APT. APT specimens were prepared by the standard two-stage electropolishing method. Prior to APT measurements, APT samples were also observed by TEM. APT analyses were conducted using a laser-assisted wide-angle APT (LAWATAP™, Cameca Instruments), applying laser pulses of 525 nm wavelength, 0.3 nJ pulse energy and 100 kHz pulse repetition rate at 40 K specimen temperature [15].

3. Results and discussion

Figure 1a shows TEM micrographs and SADP of the steel after an intercritical annealing followed by isothermal holding at 500 °C. The final microstructure is composed of a polygonal ferritic matrix (α_p) and the lamellae formed along the prior γ grain boundaries. In the lamellar structure, there are three other phases: fine ferrite, κ-carbide and retained austenite (γ_R). Hence, the γ phase is partially decomposed into ferrite and needle-like κ-carbide ($\gamma \rightarrow \kappa + \alpha_2 + \gamma_R$). For clarity, the ferritic matrix and the fine ferrite surrounded by κ-carbides have to be differentiated from each other and are hence denoted as α_p and α_2, respectively. The distribution of the α_p grains is irregular and inhomogeneous, as the current alloy has a duplex microstructure consisting of α and γ at 900 °C. HRTEM imaging yields lattice parameters of 3.65 Å for γ_R and 3.72 Å for κ, which corresponds to a lattice misfit (δ) of about 1.88% (Fig. 1b). The estimated δ is consistent with previous works [9,16], confirming that the phase boundaries between γ_R and κ are coherent as shown in Figure 1b. In the SADP along the [001] zone axis, clear {100}, {110} and {120} superlattice reflections of the κ-phase are visible. The intensity difference of the diffraction spots observed for the κ-phase can be assigned to the perovskite-type structure rather than $L1_2$ structure (characteristic of the γ′ phase). The diffraction patterns for both structures are very similar except for the fact that no intensity difference between {100} and {110} spots was detected for the γ′ phase with randomly distributed C atoms. However, the intensity of {110} spots in Figure 1b is much stronger than that of {100} and {120} spots. Typically, for fully austenitic Fe–(20–30) Mn–5.0Al–2.8C (wt.%) alloys, a higher intensity for the {010} superlattice spots than for the {110} spots was observed, which was caused by an ordering process of interstitial C at the body-centered site of κ-phase

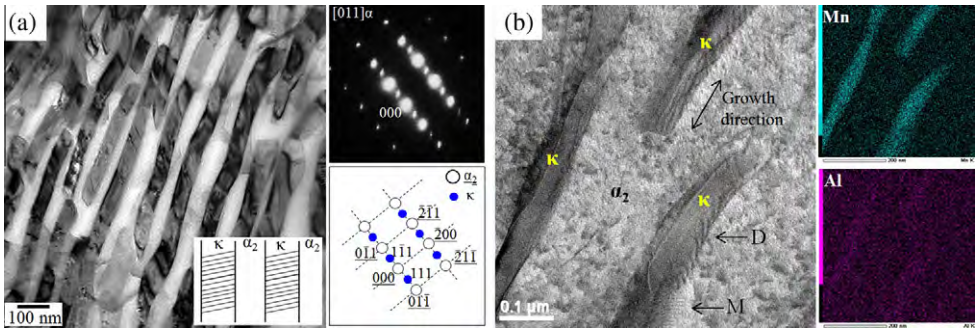

Figure 2. (a) TEM micrograph and the corresponding SADP of $[0\,1\,1]_\alpha$ zone for the steel isothermally annealed at 600 °C and (b) Cs-corrected (S)TEM bright-field image and the corresponding EDS elemental maps. D, dislocations; M, moiré fringes.

[11,12]. The intensity difference between {1 0 0} and {1 1 0} reflections, observed here, is probably attributed to the formation of C-vacancy long-range ordering inside the κ-phase formed by the employed annealing conditions, which is often observed in MC-type carbides (M = Nb, V, Mo and W) with a B1 structure [17] and in perovskite-type Ti_3AlC with an $L'1_2$ structure [18]. Furthermore, the SADP in Figure 1b reveals that there are several additional spots besides the fundamental and κ-carbide reflections. To date, this type of spot has not been found in Fe–Mn–Al–C alloys. We propose that the additional spots can be caused by fourfold splitting of the diffuse short-range order intensity peak. A similar splitting behavior was found in a disordered Cu_3Au alloy [19]. The origin of such splitting in this study could be due to an exchange of atomic position among Al, Fe and Mn inside the $L'1_2$-structure at elevated temperatures and the nominal composition of specimen.

TEM micrographs and the corresponding SADP with a $[0\,1\,1]_\alpha$ zone axis for the steel isothermally annealed at 600 °C are shown in Figure 2. In this specimen, γ phase is fully decomposed into κ-carbide and α_2 ($\gamma \rightarrow \kappa + \alpha_2$). The thickness or width of κ-particles increases with a higher annealing temperature: the average widths of the κ-particles at 500 and 600 °C are 17 ± 7 nm and 45 ± 10 nm, respectively. Thus, the spacing width between the particles for 600 annealed sample is lager than that of 500 sample due to a nucleation-growth process, leading to a decrease in the aspect ratio of the κ-particles. The shape of the κ-phase changes from extremely elongated rod-type to cylindrical-type as the annealing temperature increases. The elongated rod-like κ-carbides may be a result of high lattice misfit (δ) between α_2 and κ. The SADP confirms a $(0\,1\,1)_\alpha$ // $(1\,1\,1)_\kappa$ orientation relationship between the α_2 and κ-carbide, which corresponds to the well-known Nishiyama–Wasserman relationship [14]. Here, we observe that only {1 1 1} superlattice reflections for κ-phase are present without {1 1 0} spots for κ-phase. Assuming that the planar spacing of the $(1\,1\,0)_\alpha$ planes is 2.03 Å, the measured δ between α_2 and κ is nearly 5.9%, which implies that the formation of a coherent interface would be difficult. For such a high misfit value, the morphology of the precipitates was reported to be controlled by the elastic coherency term rather than by the interfacial energy contribution [11]. According to their results [11], the preferential growth of κ-carbide could be due to an increase in the elastic lattice misfit between γ and κ with

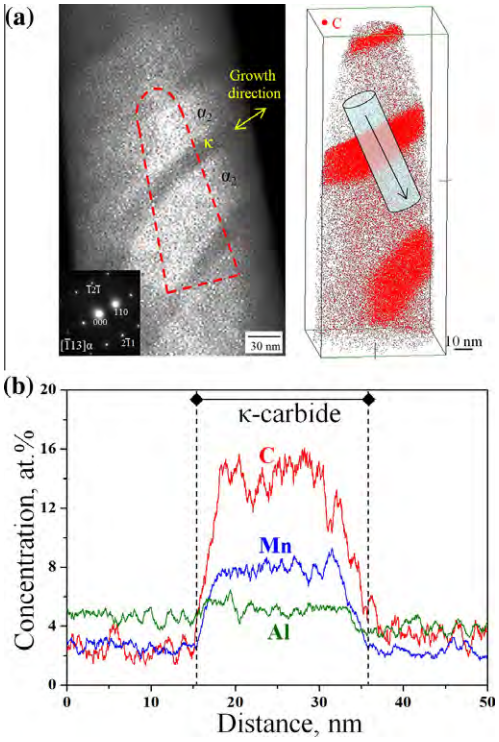

Figure 3. TEM image of APT specimen showing the lamellae formed in the steel after isothermal transformation at 600 °C and the corresponding SADP taken from ferrite, and the reconstructed APT map of C (red). The joint analysis including 1-D concentration profiles of elements obtained from the cylindrical region (cyan) reveals solutes partitioning and the morphology of the κ-carbides (For interpretation of the references to colour in this figure legend, the reader is referred to the web version of this article.).

aging time. The STEM image illustrates misfit dislocations (marked by "D") located at the α_2/κ interfaces given by Figure 2b, suggesting that the lateral interfaces are semicoherent. The spacing between dislocations dispersed at the interface is about 16.8 nm. The STEM-EDS maps reveal partitioning of Mn (cyan) and Al (pink) to κ-carbides. Although the Mn signals from the carbides are strong, the corresponding Al signals can barely be distinguished from those of the matrix. This means that the partitioning of Mn differs from that of Al. No significant C signals are also detected inside the carbides due to the insufficient sensitivity of STEM [20].

Figure 3 shows a TEM micrograph and the corresponding APT map of C (red) for the sample isothermally annealed at 600 °C. The two images were taken from exactly the same position as indicated. C-enriched lamellae are found in the reconstructed APT data, which can clearly be identified as κ-carbides by correlating the TEM micrograph with the APT map. Using 1-D composition profiles perpendicular to the semicoherent interfaces, the partitioning of solutes can be quantified. We detect a compositional fluctuation of C inside a κ-particle, much higher than those of Mn and Al. There are two possible explanations for this observation. (i) The observed C variation could be due to the formation of C-vacancies inside the κ-carbide. This defected state is in the following expressed as $(Fe,Mn)_3Al(C,Va)_x$. The stability of C–V formation inside the κ-carbide is also supported by thermodynamic calculations [7]. (ii) The preferential field evaporation induced by laser or voltage pulses and the trajectory overlap of the field-evaporated ions can lead to errors in measuring the absolute composition values determined by APT [21,22]. In this context and considering the enhanced intensity of {1 1 0} reflections in the SADP (see Fig. 1b), the former effect is more plausible than the latter one. Besides C atoms, Al and Mn atoms are partitioned to the κ-carbides, where the κ to α_2 ratio for Al is much lower than that for Mn, in good agreement with the EDS result (see Fig. 2b).

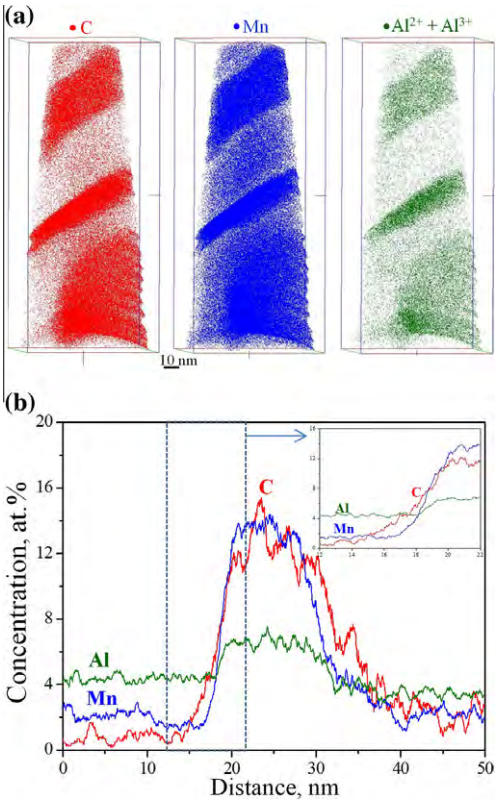

Figure 4. (a) APT maps of C, Mn (blue) and Al (green) for the steel after isothermal transformation at 500 °C, showing the rod-like shape of the κ-particles. Only 50% of Al atoms assigned as $^{27}Al^{2+}$ peak and $^{27}Al^{3+}$ peak are displayed. (b) Local concentration profiles of solutes and the artificial spread of planar interface in the vicinity of the κ/α_2 interface (For interpretation of the references to colour in this figure legend, the reader is referred to the web version of this article.).

Table 1. Chemical compositions of κ-carbide determined by APT and (S)TEM-EDS (in at.%).

Methods	APT		(S)TEM-EDS	
Temp.	500 °C	600 °C	500 °C	600 °C
Mn	14.4 ± 0.4	8.4 ± 0.4	12.7 ± 1.2	8.8 ± 0.7
C	12.8 ± 0.8	14.5 ± 1.0	–	–
Al	9.5 ± 0.2	10.1 ± 0.3	7.7 ± 0.9	7.6 ± 0.7

Table 2. The values of the enrichment factor (ε) between κ-carbide and α_2-ferrite for alloying elements as determined by APT.

	Mn	C	Al
500 °C	7.6	7.1	1.7
600 °C	2.8	4.8	1.2

The reconstructed C, Mn and Al maps obtained from APT for the steel annealed at 500 °C are shown in Figure 4. The needle-like shape of the κ-particles is confirmed. Nevertheless, APT artifacts that arise because of field-evaporation differences, such as a local magnification or demagnification effects [23,24], can lead to an error in measuring interfacial width between κ-particle and ferrite. For this reason, it is not possible to conclude unambiguously from the voltage-pulsed or laser-pulsed APT data whether the κ-phase is formed via spinodal decomposition or via a nucleation-growth sequence. Another point observed in this study is that decomposition of γ into κ and α_2 leads to supersaturation of α_2 with C.

The experimentally obtained concentrations of the κ-phase as a function of holding temperature are listed in Table 1. The Al content inside the κ-phase measured by APT was corrected by applying a deconvolution procedure for the overlapping Al^+ and Fe^{2+} mass peaks at 27 Da, considering the isotope ratios of Fe [6,25]. Accordingly, the C contents of κ-phase were obtained using the identification procedure for C peaks, as described in Ref. [26]. The compositional changes of the κ-phase depending on the temperatures as determined by APT are consistent with STEM-EDS data. In particular, an increase in the annealing temperature leads to a remarkable decrease in the Mn content of κ-carbide. This means that a higher annealing temperature affects the formation energy, lattice parameter and magnetization of κ-phase, as shown using density functional theory calculations [27]. Thus, we anticipate that an increase in the Mn substitution for Fe makes the κ-phase harder and stronger owing to the Mn–C atomic bonds being stronger than the Fe–C bonds.

Here, we confirm the formation of non-stoichiometric κ-carbides in Fe–Mn–Al–C alloys, in agreement with previous reports on κ-carbides existing over a range of varying Mn and Al contents [8,11–13]. According to these reports, the chemical composition of the κ-phase varies with both the nominal composition of the bulk specimen and its formation temperature. So far, the stoichiometric κ-phase has not been observed experimentally [28] and has been only theoretically addressed using ab initio calculations [27–29]. From our observations, we suggest under-stoichiometry of the κ-carbide with respect to C at the body-centered sites and partial replacement of Al by Fe or Mn in the corner positions

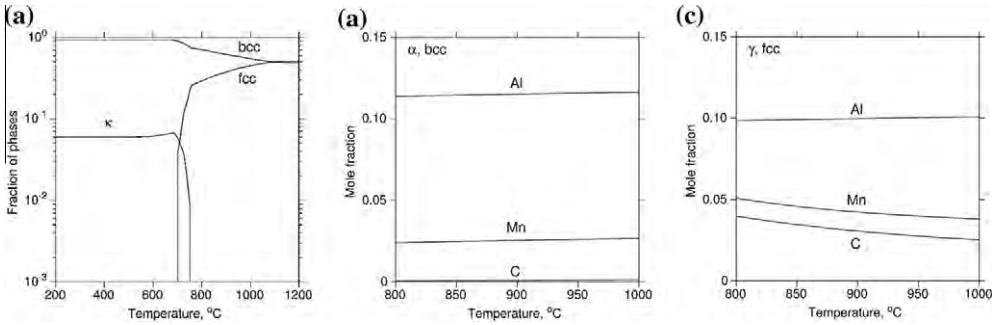

Figure 5. (a) Equilibrium phase fractions for the present alloy as a function of temperatures, and equilibrium concentration values of alloying elements in (b) ferrite and (c) austenite, as calculated using Thermo-Calc [7].

in its face-centered cubic-based unit cell. Thus, the composition of the κ-phase can be expressed as $(Fe,Mn)_3(Fe,Al)C_x$, but still containing Al. Partitioning of solutes to different phases can be quantified in terms of an enrichment factor, $\varepsilon = (\text{at.\% in } \kappa\text{-carbide})/(\text{at.\% in } \alpha_2\text{-ferrite})$. The ε values measured by APT are shown in Table 2. On the other hand, ε for Al is substantially lower than for Mn and C. It seems that Al is energetically stable inside either intermetallic κ or α_2 phase. Therefore, we conclude that during γ decomposition into κ and α_2, both product phases are competing sites for Al. This is an indication that the partitioning of Mn and Al to κ-carbides can be controlled by the abutting phase which is either austenite or ferrite.

We used Thermo-Calc predictions [7] to evaluate the remarkable decrease in ε for Mn and C with higher annealing temperature for the present alloy (Fig. 5). This calculation shows the equilibrium phase fractions of α and γ as a function of temperature. It confirms our microstructure characterization made above, namely the irregular and inhomogeneous distribution of α_p grains, as the current alloy has a duplex microstructure of α and γ at 900 °C. In addition, we quantify the concentration values of the elements in α and γ as a function of temperature, showing that most of the C can be solved in the γ, where the measured partitioning ratios of α to γ at 900 °C are 1.2/1.0 for Al and 1.0/2.0 for Mn, respectively. Even though Al is a strong ferrite former, a considerable amount of Al is solved in the γ phase at 900 °C. During isothermal holding at 500 or 600 °C for 60 min, the diffusion of C inside the γ phase is fast, while the diffusion of Al and Mn is negligible. Therefore, we propose that both the high content of Al partitioned to γ at 900 °C and fast diffusion of C during isothermal holding are significant factors for the nucleation of the κ-phase, leading to an accelerated decomposition of the γ phase. As reported, an ordering in Fe–Mn–Al–C alloys may be accomplished by the cooperative ordering of C and Al [30].

The compositional differences of κ-carbide grown at different holding temperatures can be understood in terms of undercooling (ΔT_1) between the intercritical temperature (900 °C) and the isothermal holding temperature (500 or 600 °C in this case). Stronger undercooling ($\Delta T_1 = 900\,^\circ\text{C} - 500\,^\circ\text{C}$) for the steels held at 500 °C leads to an increase in the driving force for pro-eutectoid ferritic transformation, reducing the γ fraction. As a result, a decrease in the γ fraction leads to an increase in the content of Mn and C in the γ phase and hence to its stabilization. To validate this, the volume fractions of the corresponding phases were determined by optical microscopy (OM), SEM, X-ray diffraction (XRD) and electron backscatter diffraction (EBSD). It is important to note that for the current alloys there are no ordered ferritic phases, such as B2 and DO3. Further OM, SEM and XRD results as shown in Figures S1 and S2 in the Supplementary Information confirmed that a higher holding temperature leads to a decrease in the γ_R fraction with increasing lamellae that are a mixture of fine ferrite and needle-like κ-carbide. The average volume fraction of the γ_R was 13.7 ± 2.0 vol.% and 4.8 ± 1.7 vol.% for the steels annealed at 500 and 600 °C, respectively. Based on the equilibrium phase fractions at 900 °C shown in Figure 5a, the pro-eutectoid ferrite fraction was also estimated as ~38 vol.% for 500 °C steel and ~56 vol.% for the 600 °C sample. It is therefore plausible that the steel annealed at 500 °C contains a higher γ_R fraction than the sample annealed at 600 °C, and that the κ-phase grown at 500 °C has a higher Mn and a lower Al content.

The morphological evolution of κ-carbide for different isothermal holding temperatures can be explained by the difference between the κ-phase precipitation-start temperature (750 °C as shown in Fig. 5c) and the respective holding temperatures. A stronger undercooling ($\Delta T_2 = 750\,^\circ\text{C} - 500\,^\circ\text{C}$) for the steel annealed at 500 °C increases the driving force for κ-phase precipitation, leading to a higher nucleation density of κ-particles. Subsequently, during isothermal annealing at 500 °C, the γ decomposition kinetics into κ-carbide is retarded due to the lower diffusion rate of solutes, especially C, compared to the 600 °C sample. Consequently, the κ-phase formed at 500 °C exhibits a finer and more dense distribution compared to that formed at 600 °C (Figs. 1 and 2). Here, it is the diffusion of C during isothermal holding that mainly controls κ-carbide morphology, whereas the contributions of Al and Mn are negligible.

4. Conclusions

We found direct evidence for the precipitation of nonstoichiometric κ-carbide, $(Fe,Mn)_3(Fe,Al)C_x$ containing Al, in a ferritic-matrix-based high-Al steel isothermally annealed at either 500 or 600 °C. With

increasing isothermal holding temperature: (i) the kinetics for γ decomposition increases; (ii) the width of κ-phase increases; (iii) the Mn content in κ-carbide decreases; and (iv) the enrichment factors for solutes decrease. We revealed that fine lamellae consisting of α_2 and κ-phase are formed by a eutectoid decomposition of γ, where the kinetics is controlled by the undercooling. Using TEM and APT, we also elucidated the solute partitioning at the atomic-scale and thus obtained insights into the transformation mechanism of the κ-phase in the ferrite matrix. Al atoms partitioned to austenite at high temperatures as well as the diffusion of C are significant factors for needle-like κ-carbide nucleation. The variable chemical composition of the κ-carbides was found to depend on the annealing temperature, which was confirmed by thermodynamic calculations.

Acknowledgements

The authors are grateful to Prof. D.W. Suh (GIFT) for careful reading and fruitful comments. We also acknowledge the help of H.J. Lee, J.H. Lee, Mr. H.S. Park, Prof. B.J. Lee (POSTECH), and Dr. I. Gutierrez, Dr. M. Friak (MPIE). This study was supported by POSCO and BK21.

Appendix A. Supplementary data

Supplementary data associated with this article can be found, in the online version, at http://dx.doi.org/10.1016/j.scriptamat.2012.08.013.

References

[1] D.W. Suh, S.J. Park, C.S. Oh, S.J. Kim, Scripta Mater. 57 (2007) 1097.
[2] D. Raabe, D. Ponge, O. Dmitrieva, B. Sander, Scripta Mater. 60 (2009) 1141.
[3] J.M. Jang, S.J. Kim, N.H. Kang, K.M. Cho, D.W. Suh, Met. Mater. Int. 15 (2009) 909.
[4] K.Y. Choi, C.H. Seo, H.C. Lee, S.K. Kim, J.H. Kwak, K.G. Chin, K.T. Park, N.J. Kim, Scripta Mater. 63 (2010) 1028.
[5] O. Dmitrieva, D. Ponge, G. Inden, J. Millan, P. Choi, J. Sietsma, D. Raabe, Acta Mater. 59 (2011) 364.
[6] J.B. Seol, D. Raabe, P. Choi, Y.R. Lim, C.G. Park, Acta Mater. (2012), http://dx.doi.org/10.1016/j.actamat.2012.07.064
[7] K.G. Chin, H.J. Lee, J.H. Kwak, J.Y. Kang, B.J. Lee, J. Alloys Compd. 505 (2010) 217.
[8] G. Frommeyer, U. Brüx, Steel Res. Int. 77 (9–10) (2006) 627.
[9] K.H. Han, J.C. Yoon, W.K. Choo, Scripta Metall. 20 (1986) 33.
[10] K. Sato, K. Tagawa, Y. Inoue, Scripta Metall. 22 (1988) 899.
[11] W.K. Choo, J.H. Kim, J.C. Yoon, Acta Mater. 45 (1997) 4877.
[12] K. Ishida, H. Ohtani, N. Satoh, R. Kainuma, T. Nishizawa, ISIJ Int. 30 (1990) 680.
[13] Y. Kimura, K. Handa, K. Hayashi, Y. Mishima, Intermeallics 12 (2004) 607.
[14] S.Y. Han, S.Y. Shin, H.J. Lee, B.J. Lee, S.H. Lee, N.J. Kim, J.H. Kwak, Metall. Mater. Trans. A (2011), http://dx.doi.org/10.1007/s11661-011-0942-2.
[15] T.M. Chen, T. Ohkubo, M. Kodzuke, K. Morita, K. Hono, Scripta Mater. 61 (2009) 693.
[16] A. Inoue, Y. Kojima, T. Minemura, T. Masumoto, Metall. Trans. A 12A (1981) 1245.
[17] J.H. Jang, C.H. Lee, Y.U. Heo, D.W. Suh, Acta Mater. 60 (2012) 208.
[18] C.S. Han, Met, Mater. Int. 14 (2008) 151.
[19] H. Reichert, S.C. Moss, K.S. Liang, Phys. Rev. Lett. 77 (1996) 4382.
[20] J.B. Seol, G.H. Gu, N.S. Lim, S. Das, C.G. Park, Ultramicroscopy 111 (2011) 623.
[21] A. Vella, F. Vurpillot, B. Gault, A. Bostel, A. Menand, B. Deconihout, Phys. Rev. B 73 (2006) 165416.
[22] F. Vurpillot, B. Gault, A. Vella, M. Bouet, B. Deconihout, Appl. Phys. Lett. 88 (2006) 094105.
[23] O. Thuillier, F. Danoix, M. Gouné, D. Blavette, Scripta Mater. 55 (2006) 1071.
[24] M.D. Mulholland, D.N. Seidman, Microsc. Microanal. 17 (2011) 950.
[25] O. Dmitrieva, P. Choi, S.S.A. Gestl, D. Ponge, D. Raabe, Ultramicroscopy 111 (2011) 623.
[26] Y.J. Li, P. Choi, C. Borchers, Y.Z. Chen, S. Goto, D. Raabe, R. Kirchheim, Acta Mater. 59 (2011) 3965.
[27] J.Y. Noh, H. Kim, J. Kor, Phys. Soc. 58 (2011) 285.
[28] D. Connétable, P. Magis, Intermetallics 16 (2008) 345.
[29] H. Ohtani, M. Yamano, M. Hasebe, ISIJ Int. 44 (2004) 1738.
[30] K.H. Han, W.K. Choo, Scripta Metall. 17 (1983) 281.

Available online at www.sciencedirect.com

SciVerse ScienceDirect

Acta Materialia 60 (2012) 2790–2804

Acta MATERIALIA

www.elsevier.com/locate/actamat

Nanoscale austenite reversion through partitioning, segregation and kinetic freezing: Example of a ductile 2 GPa Fe–Cr–C steel

L. Yuan [a], D. Ponge [a], J. Wittig [a,b], P. Choi [a], J.A. Jiménez [c], D. Raabe [a,*]

[a] *Max-Planck-Institut für Eisenforschung, Max-Planck-Str. 1, 40237 Düsseldorf, Germany*
[b] *Vanderbilt University, Nashville, TN 37235-1683, USA*
[c] *CENIM-CSIC, Avda. Gregorio del Amo 8, 28040 Madrid, Spain*

Received 5 July 2011; received in revised form 29 November 2011; accepted 25 January 2012
Available online 2 March 2012

Abstract

Austenite reversion during tempering of a Fe–13.6 Cr–0.44 C (wt.%) martensite results in an ultra-high-strength ferritic stainless steel with excellent ductility. The austenite reversion mechanism is coupled to the kinetic freezing of carbon during low-temperature partitioning at the interfaces between martensite and retained austenite and to carbon segregation at martensite–martensite grain boundaries. An advantage of austenite reversion is its scalability, i.e. changing tempering time and temperature tailors the desired strength–ductility profiles (e.g. tempering at 400 °C for 1 min produces a 2 GPa ultimate tensile strength (UTS) and 14% elongation while 30 min at 400 °C results in a UTS of ~1.75 GPa with an elongation of 23%). The austenite reversion process, carbide precipitation and carbon segregation have been characterized by X-ray diffraction, electron back-scatter diffraction, transmission electron microscopy and atom probe tomography in order to develop the structure–property relationships that control the material's strength and ductility.

Keywords: Austenite reversion; Partitioning; Diffusion; Strength; Ductility

1. Introduction

A high demand exists for lean, ductile and high-strength Fe–Cr stainless steels in the fields of energy conversion, mobility and industrial infrastructure. As conventional martensitic stainless steels (MSSs) typically exhibit brittle behavior, supermartensitic Fe–Cr stainless steels (SMSSs) with enhanced ductility have been designed in the past years by reducing carbon (<0.03 wt.%) and adding nickel (4–6.5 wt.%) and molybdenum (2.5 wt.%) [1–4]. The heat-treated microstructures of these materials are characterized by tempered martensite and retained austenite [1–4].

In this work we present an alternative approach of designing MSSs with both high strength and high ductility. Our method is based on nanoscale austenite reversion and martensite relaxation via a modest heat treatment at 300–500 °C for several minutes. We make the surprising observation that this method leads to very high strength (up to 2 GPa) of a Fe–13.6Cr–0.44C (wt.%) steel without loss in ductility (X44Cr13, 1.4034, AISI 420).

Quenching followed by tempering is known to improve the strength and toughness of martensitic steels [5–7]. Specifically, quench and partitioning (Q&P) treatments are efficient for producing steels with retained austenite and improved ductility [8]. The heat treatment sequence for Q&P steel involves quenching to a temperature between the martensite-start (M_s) and martensite-finish (M_f) temperatures, followed by a partitioning treatment either at, or above, the initial quench temperature. Partitioning is typically designed in a way that enriches and stabilizes the retained austenite with carbon from the supersaturated martensite [9]. In conventional Q&P processes, the quench temperature is hence chosen such that some retained austenite prevails and subsequent tempering leads to carbon

* Corresponding author. Tel.: +49 0211 6792 333.
E-mail address: d.raabe@mpie.de (D. Raabe).

1359-6454/$36.00
doi:10.1016/j.actamat.2012.01.045

partitioning between martensite and austenite. Typically, no new austenite is formed during partitioning.

In our study we modify this approach with the aim to increase the amount of austenite during low-temperature partitioning. We start with austenitization and water quenching to room temperature. This provides a martensitic–austenitic starting microstructure. During a subsequent heat treatment in the range 300–500 °C, austenite reversion [10–15] takes place on the basis of partial partitioning according to local equilibrium, segregation and kinetic freezing of carbon inside the newly formed austenite.

It is important to point out that the phenomena occurring during austenite reversion are in the present case different from conventional Q&P approaches: in Q&P processing, the carbon diffuses from martensite into the already present austenite during tempering where equilibration of the carbon distribution inside the austenite is generally assumed. In the current case of low-temperature partitioning, however, the carbon is enriched in front of the austenite boundary and accumulates there since it has a much higher diffusion rate in body-centered cubic (bcc) than in face-centered cubic (fcc) material. The accumulated carbon at the martensite–austenite interface then provides a high local driving force for austenite reversion. Once captured by the growing austenite, the carbon is kinetically frozen owing to its small mobility in this phase.

The phenomena occurring during austenite reversion in Fe–Cr–C stainless steels are complex due to the high content of carbon and substitutional alloying elements. In contrast to typical Q&P steels where carbide precipitation (M_3C) is suppressed by alloying with Si and/or Al [16], in the present alloy M_3C-type carbide precipitation occurs at 400 °C. This means that a kinetic and thermodynamic competition exists for carbon between austenite reversion, enrichment of retained austenite and carbide formation during tempering.

Therefore, the partitioning temperature must be chosen on a theoretically well founded basis for two reasons: first, low temperature annealing requires more local carbon enrichment to provide a driving force high enough for austenite reversion. We emphasize in this context that the local equilibrium matters for this process, i.e. a high carbon content is required at the martensite–austenite interface (not everywhere within the austenite). Equilibration of the carbon inside the austenite is not necessarily required. Second, high temperature annealing may cause more carbide formation, consuming too much carbon, so that austenite reversion is suppressed due to an insufficient carbon chemical potential to promote it.

In order to elucidate the competing phenomena occurring during such low-temperature partitioning, namely, carbide formation vs. austenite reversion as well as the carbon redistribution inside the retained and reversed austenite fractions, atom probe tomography (APT) was used. This method allows us to measure the carbon content inside the austenite, which determines its stability, as well as inside the martensite and the carbides [17–28]. The APT method allows for three-dimensional (3-D) elemental mapping with nearly atomic resolution and provides information about internal interfaces and local chemical gradients [28–32].

2. Experimental

The material used in this study was a martensitic stainless steel with the chemical composition Fe–13.6Cr–0.44C (wt.%; 1.4034, X44Cr13, AISI 420), which was provided by ThyssenKrupp Nirosta as a cold rolled sheet, Table 1. The Ae_3 temperature, calculated by Thermo-Calc [33] using the TCFE5 database [34], indicates that the incipient holding temperature for full austenitization should be above 800 °C. The calculation further reveals that full dissolution of chromium carbides in austenite is achieved at ~1100 °C. Hence, the annealing conditions were set to 1150 °C for 5 min. Dilatometer tests were performed using a Bähr Dil805 A/D quenching and deformation device to identify the M_s temperature during quenching. After water quenching, tempering at 300, 400 and 500 °C, respectively, with different holding times was performed to study carbon redistribution, austenite reversion and carbide formation (Fig. 1).

Mechanical properties were determined by tensile and Vickers hardness measurements (980N load, HV10). Tensile tests were carried out along the rolling direction of the samples at room temperature. Flat tensile specimens were machined with a cross-section of 2.5 mm × 8 mm and a gauge length of 40 mm. The tests were conducted on a Zwick/Roell Z100 tensile testing machine at a constant cross-head speed of 1 mm min^{-1}, corresponding to an initial strain rate of 4.2×10^{-4} s^{-1}.

The volume fraction of the austenite phase after heat treatments (carbide dissolution annealing and tempering at 400 °C for 1, 2, 10 and 30 min) was measured by X-ray diffraction (XRD), electron back-scatter diffraction (EBSD) and magnetic characterization (Feritscope MP30E-S).

EBSD samples were prepared by standard mechanical grinding and polishing procedures normal to the rolling direction. Subsequently, these samples were electropolished using Struers electrolyte A3 at room temperature using a voltage of 40 V, a flow rate of 20 s^{-1} and a polishing time of 20 s. EBSD was performed on a JEOL-6500F high-resolution field-emission scanning electron microscope operated at 15 kV [35].

XRD measurements were carried out using Co Kα radiation. XRD data were collected over a 2θ range of 30–138°

Table 1
Chemical composition of material used for the investigation (1.4034, X44Cr13, AISI 420).

	C	Cr	Mn	Ni	Si	N	Fe
wt.%	0.437	13.6	0.53	0.16	0.284	0.0205	Bal.
at.%	1.97	14.19	0.52	0.15	0.55	0.079	Bal.

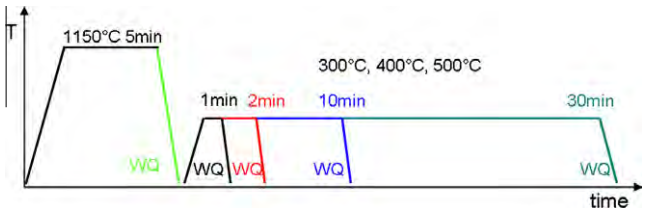

Fig. 1. Schematic diagram of the heat treatment route (WQ: water quenching).

with a step width of 0.05° and a counting time of 10 s per step. The Rietveld method was used for the calculation of the structural parameters from the diffraction data of the polycrystalline bulk materials. We used version 4.0 of the Rietveld analysis program TOPAS (Bruker AXS). The analysis protocol included consideration of background, zero displacement, scale factors, peak breath, unit cell parameter and texture parameters. The room temperature structures used in the refinement were martensite/ferrite and austenite.

Thin foils were prepared using standard twin-jet electropolishing from the as-quenched material and the tempered samples before and after deformation [36]. These samples were examined by transmission electron microscopy (TEM) in a Philips CM 20 at an acceleration voltage of 200 kV to characterize the carbide evolution and the formation of reverted austenite. Carbide characterization was also carried out by using a carbon extraction replica technique [37] and investigated by electron diffraction and energy dispersive spectroscopy (EDS) in the transmission electron microscope.

Needle-shaped APT samples were prepared by applying a combination of standard electropolishing and subsequent ion-milling with a focused-ion-beam (FIB) device. APT analyses were performed with a local electrode atom probe (LEAP™ 3000X HR) in voltage mode at a specimen temperature of ~60 K. The pulse-to-base voltage ratio and the pulse rate were 15% and 200 kHz, respectively. Data analysis was performed using the IVAS software (Cameca Instruments).

3. Results

3.1. Mechanical properties

The as-received cold rolled and recrystallized material has an ultimate tensile strength (UTS) of 640 MPa and a uniform elongation of 19%, Fig. 2a. After austenitization at 1150 °C and water quenching, the material is brittle and fails before the yield stress is reached at a stress of 400 MPa (Fig. 2a). Thus, the true UTS for the as-quenched state could be only estimated from the indentation hardness. The relationship between Vickers hardness (HV) and tensile strength was calculated considering a linear relationship of the form $\Delta HV = K \times \Delta UTS$. A constant K of 3.5 was determined by linear regression through data obtained from the hardness and UTS values obtained from samples after tempering at 400 °C for different times. Fig. 2e suggests that the hardness for the as-quenched state corresponds to a tensile strength of more than 2300 MPa.

Fig. 2a also shows the stress–strain curves obtained from the tensile tests performed on samples tempered at 400 °C for different times. The most remarkable feature of these curves is the transition from a brittle behavior in the as-quenched material to a ductile one after tempering. When the tempering time is increased, we observe an increase in uniform elongation and a decrease in UTS. After 30 min, the uniform elongation of the sample reaches a value of ~22% and a UTS above 1760 MPa. This value for the UTS can be also reached upon tempering at 500 °C, but in this case, a gradual increase in total elongation upon increase in tempering time is not observed, Fig. 2b. It can be observed that in this case the stress does not go through a maximum; that is, σ/e (the partial derivative of the stress with respect to strain) does not go through zero. This would indicate that the sample fractures before the strain reach the necking value. At 300 °C, after 1 min, the ductility improves slightly, i.e. longer tempering is required for obtaining better ductility at this temperature, as shown in Fig. 2c. When comparing the mechanical properties of samples tempered at different temperatures (Fig. 2d), the 400 °C treatment yields the optimum improvement in both UTS and total elongation (TE).

3.2. Phase fractions and kinetics: predictions and experiments

Thermo-Calc was used to calculate the phase equilibrium at the different partitioning temperatures. For evaluating kinetics during heating and cooling, we conducted dilatometer tests (Fig. 3). The heating and cooling rates were set to 10 and $-30\ K\ s^{-1}$, respectively. Above 876 °C, the microstructure is fully austenitic. The M_s temperatures were derived from the dilatometer tests (118 °C after 1150 °C annealing and 360 °C after 950 °C annealing). The Thermo-Calc calculations were used to predict the equilibrium carbon content of the austenite after annealing at different temperatures (Fig. 3c).

Fig. 4 shows the phase fraction of austenite vs. tempering time for 400 °C measured by feritscope (magnetic signal), EBSD and XRD. For the as-quenched state the EBSD result provides a higher volume fraction (20%) than the magnetic (14.5%) and the XRD data (8%), which is attributed to the limited statistics of the EBSD method. During the first 2 min of tempering the amount of austenite increases rapidly, indicating austenite reversion. After 30 min, nearly 40 vol.% austenite is observed consistently for all three methods.

Fig. 5 shows in situ EBSD observations of the austenite during tempering. Fig. 5a maps the material in the as-quenched state containing only retained austenite. Fig. 5b shows the same area during the in situ experiment containing both retained plus reverted austenite after 5 min

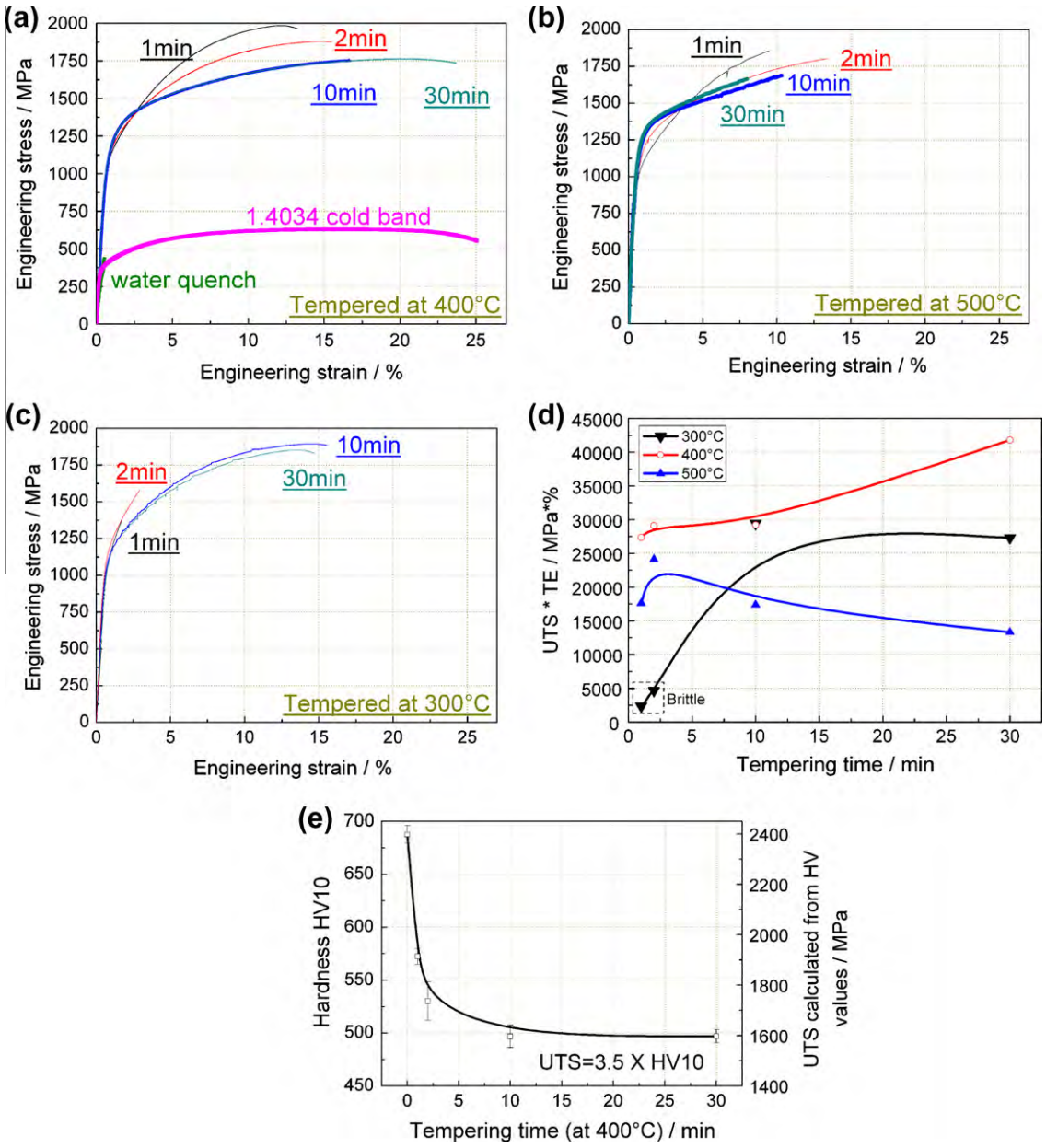

Fig. 2. Mechanical properties of the quenched and partitioned stainless steel Fe–13.6Cr–0.44C (wt.%, 1.4034, AISI 420) after different types of partitioning and austenite reversion treatments. The original state of a commercial alloy (1.4034, cold band) is shown as reference. The term "cold band" refers here to hot rolled, cold rolled and finally recrystallized material. (a–c) Stress–strain curve of samples tempered at 400, 500 and 300 °C, respectively. Note in (a) that the as-quenched sample (green) fails already in the elastic regime. (d) Multiplied quantity UTS × TE as a function of annealing time for the three different temperatures; (e) UTS–HV relationship (UTS: ultimate tensile strength; HV: Vickers hardness; TE: total elongation).

tempering at 400 °C subsequent to the quenching treatment. The EBSD map reveals the fine dispersion of the newly formed reverted austenite after 5 min. We observe two kinds of austenite, namely one with a coarse topology and another one with a fine and dispersed topology.

The microstructures of the samples tempered for 0, 1 and 2 min, respectively, are shown in Fig. 6. The as-quenched material (0 min tempering) is brittle and failed already in the elastic regime during tensile testing. From the microstructure it can be seen (Fig. 6b, left: before tensile test; right: after tensile test, for each state) that only a small amount of austenite was transformed to martensite when the material failed, i.e. austenite bands can still be observed near the fracture interface. For samples after 400 °C tempering, no premature failure takes place and the total elongation (TE) reaches 14% (engineering strain). The microstructure at the fracture zone shows nearly no remaining austenite. This observation indicates that deformation-driven austenite-to-martensite transformation takes place. Secondary cracks along the tensile direction are visible in the EBSD maps. It seems that these cracks follow the band-like former retained austenite regions, which transformed during straining into martensite.

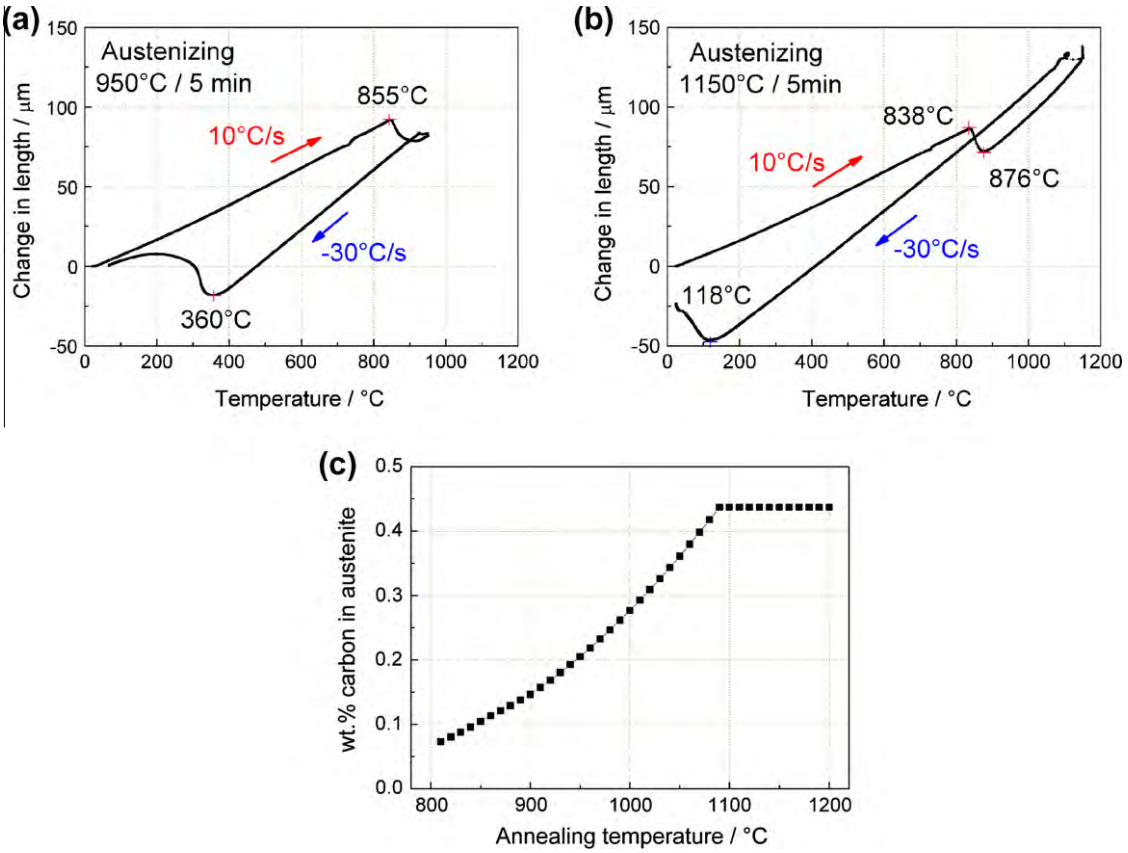

Fig. 3. Results of the dilatometer tests of the stainless steel Fe–13.6Cr–0.44C (wt.%, 1.4034). (a) Austenitization at 950 °C for 5 min. (b) Austenitization at 1150 °C for 5 min. (c) Calculated equilibrium carbon content in austenite at different annealing temperatures (Thermo-Calc TCFE5).

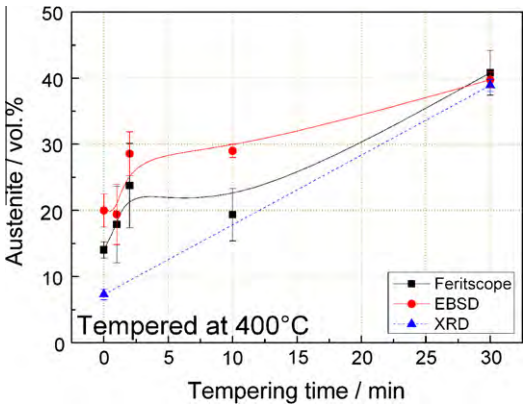

Fig. 4. Austenite volume fraction as a function of tempering time (at 400 °C) measured by feritscope (magnetic signal), EBSD and XRD.

3.3. TEM characterization

After solid solution and subsequent water quenching, we found no retained austenite in the TEM foils (Fig. 7a and b). This is in contrast to the results obtained from the EBSD maps which show retained austenite in the as-quenched state (Figs. 5 and 6). We attribute this discrepancy between TEM and EBSD results to the fact that the as-quenched metastable retained austenite – when thinned for TEM analysis – is no longer constrained by the surrounding martensite and hence transforms into martensite.

After 1 min tempering at 400 °C we observe a high tensile strength of 2 GPa, Fig. 2a. The corresponding microstructure was monitored by TEM, Fig. 7. Fig. 7c and d gives an overview of the nanoscaled elongated carbides formed during tempering.

The carbides have an average length of 70 nm and an average width of 5 nm. After 30 min tempering the average particle spacing is ~80 nm and the length 110 nm. The carbides after 1 min tempering at 400 °C were examined via carbon extraction replica. The diffraction patterns reveal that they have M_3C structure. This means that the formation of $M_{23}C_6$ carbides is suppressed at such a low tempering temperature. EDS analyses showed that the metal content in the carbide (M in M_3C) amounts to 74 at.% Fe and 26 at.% Cr, i.e. the Cr/Fe atomic ratio is 0.35. The measured chromium content in the M_3C carbides significantly deviates from the nominal chromium concentration of 14.2 at.% Cr/82.5 at.% Fe = 0.17.

Fig. 7e shows the formation of a thin austenite layer that is located at a former martensite–martensite grain boundary. Fig. 7f is a close-up view of a thin austenite zone that is surrounded by martensite. Electron diffraction analysis reveals that a Kurdjumov–Sachs orientation relationship exists between the martensite matrix and the thin austenite

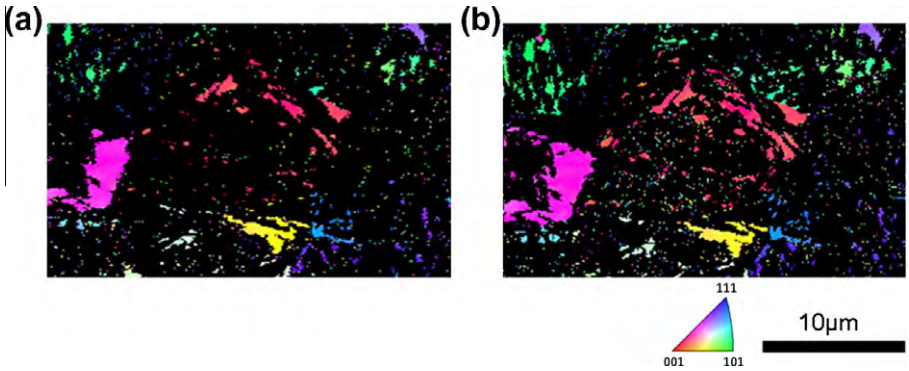

Fig. 5. EBSD inverse pole figure map of the same specimen region showing retained and reverted austenite (IPF‖ND, only austenite shown): (a) shows the material as-quenched containing only retained austenite; (b) shows the material containing both retained plus reverted austenite after quenching and 5 min tempering at 400 °C (EBSD: electron back-scatter diffraction; IPF: inverse pole figure color code; ND: normal direction).

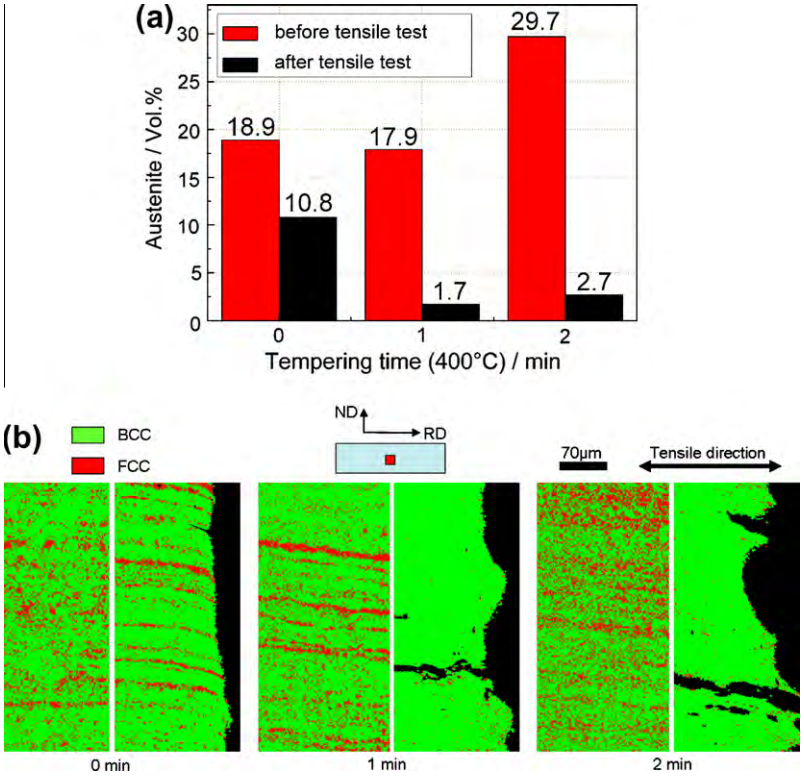

Fig. 6. (a) EBSD phase maps of samples tempered at 400 °C for 0, 1 and 2 min at 400 °C, and of the TRIP effect obtained from EBSD phase analysis. The red columns show the austenite content before and the black ones after the tensile tests. (b) Microstructure of samples before and after tensile testing subjected to different tempering conditions (left: before tensile test; right: after tensile test); bcc: martensite phase; fcc: austenite phase.

layer, Fig. 7g [38]. In line with the in situ EBSD results in Fig. 5, where we observed reverted austenite formed between martensitic grains, the austenite film observed here in TEM might be either retained or reversed austenite. In order to determine more reliably which of the two kinds is observed local atomic scale chemical analysis is conducted by using APT as outlined below. The two types of austenite can then be distinguished in terms of their carbon content: Retained austenite has at first the nominal quenched-in C content (~2 at.% in the present case) of the alloy while reverted austenite has a higher C content (up to 9 at.%) owing to local partitioning and kinetic freezing. However, we also have to account for the possibility that the retained austenite can have a higher C content as the lath martensite mechanism is slow enough to allow for some C diffusion out of the martensite into the retained austenite during quenching.

3.4. Atom probe tomography

The local chemical compositions and their changes during 400 °C tempering of the martensite, austenite, carbides

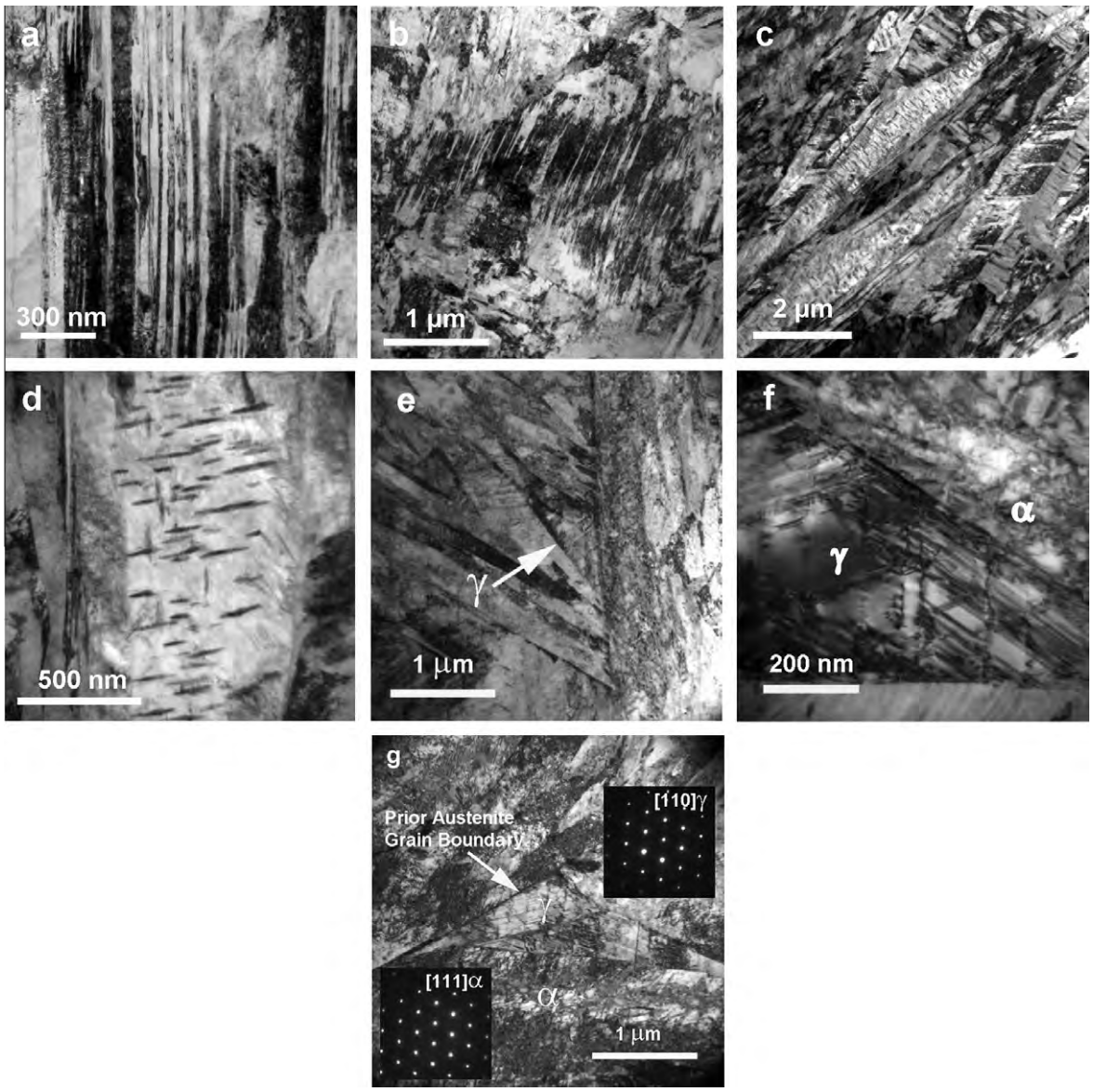

Fig. 7. TEM images of as-quenched sample (only lath martensite was found: (a and b) TEM images of samples tempered at 400 °C for 1 min; (c) overview image of the very dense array of nanoscaled carbides that is formed during tempering; (d) in-grain view of the carbides; (e) overview image of the formation of a reverted austenite grain that is located at a former martensite–martensite grain boundary; (f) close-up view of reverted austenite that is surrounded by martensite; (g) electron diffraction analysis reveals that a Kurdjumov–Sachs growth orientation relationship exists between the martensite matrix and the reverted austenite.

and interface regions were studied by atom probe tomography. Phase identification is in all cases achieved via the characteristic carbon contents of the present phases. Fig. 8 shows the 3-D atom maps after water quenching (Fig. 8a), water quenching plus tempering at 400 °C for 1 min (Fig. 8b) and water quenching plus tempering at 400 °C for 30 min (Fig. 8c). Carbon atoms are visualized as pink dots and carbon iso-concentration surfaces are in green for a value of 2 at.%. This value corresponds to the nominal carbon concentration of the alloy of 0.44 wt.%. The different phases (martensite, austenite, carbide) are marked. They were identified in terms of their characteristic carbon content and the TEM and EBSD data presented above. For more quantitative analyses, one-dimensional compositional profiles of carbon across the martensite–martensite and martensite–austenite interfaces were plotted (along cylinders marked in yellow in the 3-D atom maps).

3.4.1. As-quenched condition

Fig. 8a reveals that in the probed volume carbon is enriched along the martensite–austenite interface. The interface region, shown as composition profile in Fig. 8a, reveals an average carbon concentration of ~1.90 at.% in the austenite with strong local variations and of ~0.98 at.% in the abutting supersaturated martensite. The carbon concentration in the austenite nearly matches the nominal carbon concentration of the alloy. Some carbon clusters occur in both phases. The carbon concentration

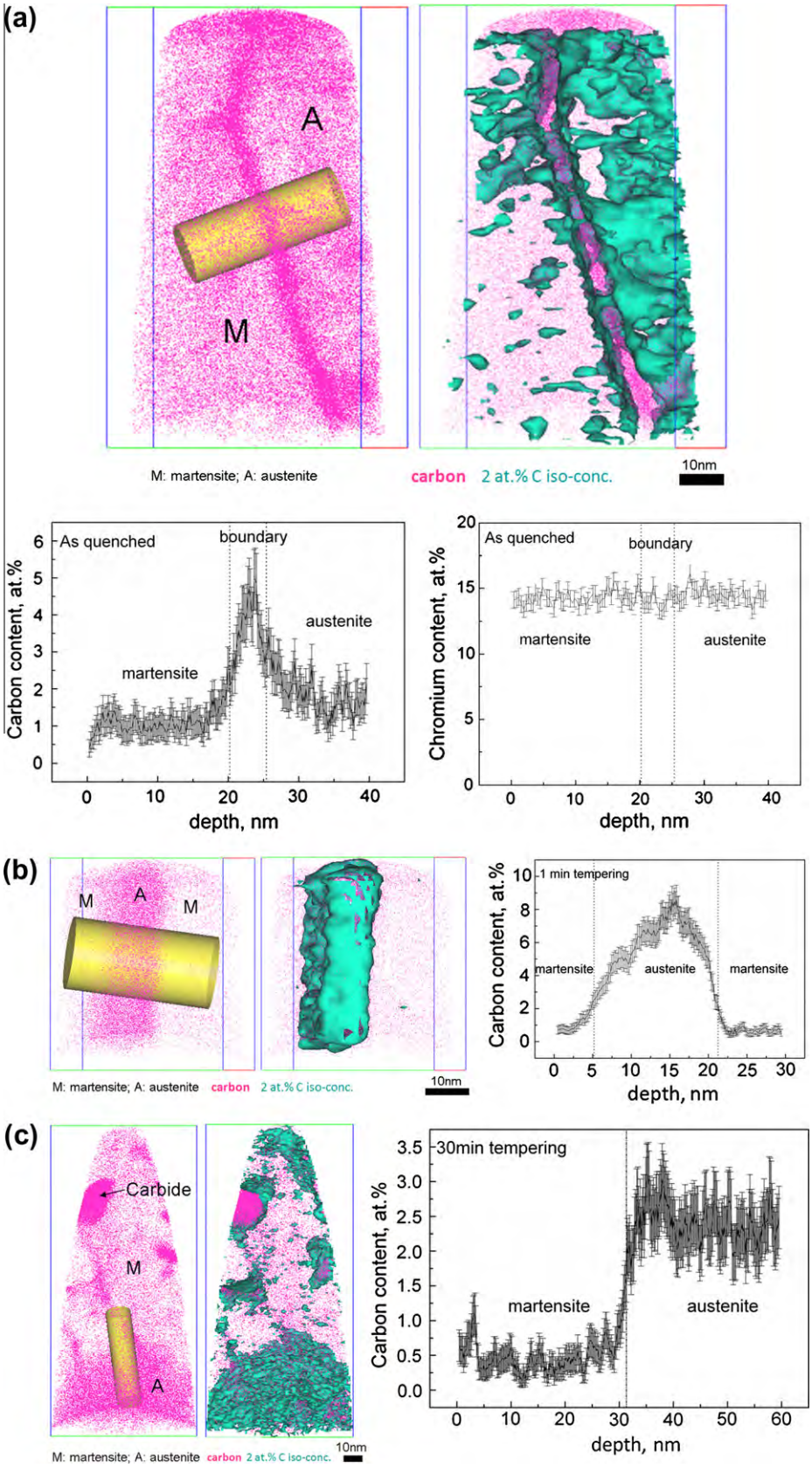

Fig. 8. (a) 3-D reconstructions (frame scale in nm) of sample after water quenching. The data clearly show that carbon redistribution already occurs during quenching. Cr redistribution does not occur. (b) Tempered at 400 °C for 1 min; (c) tempered at 400 °C for 30 min. Carbon atoms are displayed pink. The different phases are marked in the figure. Carbon iso-concentration surface (2 at.%, corresponding to 0.44 wt.%, green) and concentration profiles across the phase boundaries along the yellow cylinder) are also shown.

Table 2
Change of the carbon content observed in each phase via atom probe tomography during annealing, quenching and austenite reversion. The carbon partitioning to the different phases is quantified in terms of the enrichment factor ε = (at.% C tempered)/(at.% C as-quenched), which allows us to compare the chemical composition in the phases before and after tempering.

State of samples	Retained austenite (at.%)	Martensite (at.%)	Interface (at.%)	Reverted austenite (at.%)
Nominal composition (annealing at 1150 °C)	1.97%	–	–	–
As-quenched	1.90%	0.98%	4.52%	–
Quenched plus tempering (400 °C/1 min)	–	0.82% ($\varepsilon = 0.84$)	–	6.86% ($\varepsilon = 3.61$)
Quenched plus tempering (400 °C/30 min)	2.42% ($\varepsilon = 1.27$)	0.48% ($\varepsilon = 0.49$)	–	–

in these clusters is ~3 at.%, i.e. they are not carbides. In a thin interface layer of only ~5 nm, the carbon content is very high and reaches a level of 4–6 at.%. In contrast to the variation in the carbon distribution, the chromium content is the same in the martensite, the interface and the austenite, Fig. 8a.

3.4.2. 400 °C tempered condition after quenching

After 1 min tempering at 400 °C, a carbon-enriched austenite layer (15–20 nm width) is observed between two abutting martensite regions (Fig. 8b). The thin austenite zone contains on average ~6.86 at.% carbon while the martensite matrix contains only ~0.82 at.% carbon. The identification of the phases in these diagrams follows their characteristic carbon content.

After 30 min tempering (Fig. 8c), different carbon-enriched areas appear. They correspond to individual phases. The analyzed volume can be divided into two zones. The top region with low carbon content corresponds to martensite. The bottom zone with higher carbon content corresponds to austenite. Inside the martensitic region there are areas with very high carbon content (see arrow in Fig. 8c). The carbon content is 25.1 at.% in this particle, indicating M_3C cementite stoichiometry. In the martensitic matrix surrounding the precipitate the carbon content amounts to only 0.48 at.%. Carbon partitioning to the different phases can be quantified in terms of an enrichment factor ε = (at.% C tempered)/(at.% C as-quenched) to compare the compositions in the phases before and after tempering. The observed values of ε for each state are listed in Table 2. The carbon content in the martensite decreases continuously during tempering, which can be ascribed to carbon partitioning from the supersaturated martensite to the austenite and to carbide formation [39–50].

4. Discussion

4.1. Mechanisms of partitioning and austenite reversion

The microstructure observed by EBSD and TEM allows us to monitor the austenite development at the mesoscopic scale: during the initial high temperature solution annealing in the austenitic regime (1150 °C for 5 min), all carbides were dissolved (Fig. 3c). The high content of solute carbon that is present in the austenite after carbide dissolution decreases the M_s and the M_f temperatures of the austenite below room temperature. Hence, 8–20 vol.% retained austenite exists after quenching the solution-annealed material to room temperature, Fig. 4. The differences in retained austenite are due to the individual precision of the different characterization methods. EBSD provides a direct method and hence is assumed to give a realistic value within its statistical limits.

After tempering at 400 °C for 30 min the area fraction of austenite increases to ~40%. This change documents that strong austenite reversion takes place even at this low temperature. The local variations in the austenite dispersion after short tempering were larger compared to longer tempering times. We attribute this heterogeneity in the re-austenitization kinetics and topology to the mean diffusion range of the carbon and to the distribution of the carbon sources. Using the data of Speer et al. [40] for the diffusion coefficients in ferrite $D_\alpha = 2 \times 10^{-12}\ m^2\ s^{-1}$ and in austenite $D_\gamma = 5 \times 10^{-17}\ m^2\ s^{-1}$ we obtain a mean free path for carbon of 1.5×10^{-4} m in ferrite and 7.4×10^{-7} m in austenite at 400 °C and 30 min.

This means that austenite reversion starts at decorated defects (e.g. internal interfaces) where the local carbon concentration is high enough and the nucleation energy low enough to promote the formation of this phase. Fig. 7e confirms this assumption. The TEM analysis also suggests that austenite reversion proceeds via a Kurdjumov–Sachs orientation relationship. Shtansky et al. [38] found the same crystallographic relationship during reverse transformation in an Fe–17Cr–0.5C tempered martensite (wt.%).

An important aspect of the pronounced austenite reversion in the current case is that the competing formation of $M_{23}C_6$ carbides is suppressed at 400 °C. This means that more carbon is available to stabilize and promote austenite formation [38,45–47].

We used Thermo-Calc predictions [33,34] to estimate the driving force for austenite reversion for the current alloy and the employed tempering conditions, Fig. 9b. The results reveal that if the carbon concentration in the bulk martensite (α') exceeds 1.21 wt.% (5.45 at.%), austenite (γ) will form at 400 °C, provided that the nucleation barrier is overcome. This result confirms our suggestion made above, namely that no bulk austenitization can occur at this temperature since the average carbon content of the matrix is too low. Instead we assume that only certain lattice defects (interfaces) that experience very high elastic distortions and carbon segregation can provide the nucleation

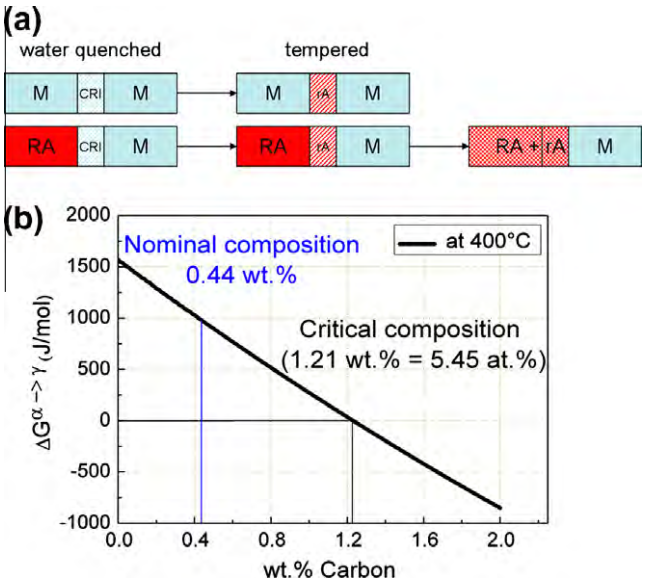

Fig. 9. (a) Schematic illustration of austenite reversion. M: martensite; CRI: carbon-rich interface; RA: retained austenite as obtained after quenching with equilibrium austenite carbon content; rA: reverted austenite formed during 300–500 °C tempering at interfaces owing to the higher local carbon content. After sufficient long diffusion time the carbon content in both types of austenite becomes similar. (b) Calculated driving force for austenite reversion at 400 °C (Thermo-Calc TCFE5).

conditions and a sufficiently high carbon concentration for local austenite formation, Figs. 7e–g and 8. This leads to an increase in the overall austenite fraction. Fig. 6a shows that a 2 min heat treatment at 400 °C leads to an increase in the austenite content from 18.9 to 29.7 vol.%.

Thermo-Calc predictions show that in the current alloy carbon provides the required driving force for this low-temperature austenite reversion. Substitutional atoms, particularly Cr, do not participate in reversion in the current alloy owing to their limited mobility at 400 °C, i.e. the driving force for transformation is here provided exclusively by the high carbon enrichment rather than by substitutional depletion of the austenite, Fig. 8a [39].

Based on these thermodynamic boundary conditions the APT results allow us now to monitor and evaluate the kinetics of carbon at different stages of tempering in more detail (Fig. 8). Fig. 8a shows the as-quenched state: during solution annealing where the material is completely austenitic the elements distribute homogeneously within that phase.

At the onset of water quenching, the majority of the austenite starts to transform into martensite without at first changing its chemical composition. However, as the solubility of carbon in the quenched-in martensite is very small, carbon starts to leave the martensite during and after the $\gamma \rightarrow \alpha'$ transformation and enriches at the γ–α' interfaces, Fig. 8a [45–50]. This process can happen extremely fast: Speer et al. [40,41] showed that carbon partitioning between martensite and austenite in a 0.19C–1.59Mn–1.63Si (wt.%) steel required at 400 °C less than 0.1 s owing to the relatively high diffusion rate of carbon in martensite. In contrast, the further distribution of the newly acquired carbon within the austenite is nearly three orders of magnitude slower [40–50]. This means that in this case the escape rate of carbon from the newly forming lath martensite is much higher than the carbon equilibration within the austenite [48–50].

In the present quenching process, carbon segregation takes place even faster than in the study quoted above [40,41]. In the current case the carbon has already started to partition and segregate at the martensite–austenite interfaces during the early stages of water quenching immediately after the first martensite has formed [45–50]. The fast kinetics is due to the high mobility of carbon in martensite, Table 3. Such pronounced carbon segregation at the martensite–austenite interfaces is clearly observed in the as-quenched state (Fig. 8a). In the interface area the carbon content reaches up to 4–6 at.% within a narrow layer of ~5 nm. This value is clearly above the nominal composition that purely retained austenite would have [45–50]. Owing to the high escape rate of carbon from the martensite this zone is interpreted as a portion of initially retained austenite which has been enriched in carbon during quenching [45–50].

As explained above this high level of carbon segregation in the present case is a consequence of two effects: the rapid carbon escape from the newly formed martensite, and the low mobility of carbon within the retained austenite. According to Table 3 at 400 °C in 1 min carbon can diffuse 27.000 nm in the martensite and only 130 nm in the austenite [40]. Other sources suggest a 10–20% smaller mean free path of carbon in the martensite [43,44].

Hence, the carbon segregation observed after quenching (Fig. 8a) is due to a partitioning step and a kinetic freezing step (limited mobility of carbon once it arrives in the austenite). From comparing this experimentally observed frozen-in value of 4–6 at.% carbon at the martensite–austenite interface (Fig. 8a) with the value that is predicted by Thermo-Calc as a driving force required for austenite reversion at 400 °C (5.45 at.%), we conclude that austenite reversion will occur under the current conditions at this interface upon heat treatment.

After 1 min tempering at 400 °C, a carbon-enriched austenite layer is observed between two martensite regions (Fig. 8b). In principle this thin austenite layer could originate either from a very thin layer of retained austenite that was enriched with carbon due to partitioning from the

Table 3
Diffusion data for carbon in ferrite and austenite taken from Ref. [40]. For the current heat treatment case of 400 °C (673 K) the diffusion coefficient in ferrite is $D_\alpha = 2 \times 10^{-12}$ m^2 s^{-1} and in austenite $D_\gamma = 5 \times 10^{-17}$ m^2 s^{-1}. The table gives the mean free path for the different tempering stages. The diffusion of carbon on the ferrite can be regarded as a lower bound. The corresponding value for martensite is likely to be higher owing to the high defect density of the martensite.

Time (min)	Austenite (m)	Ferrite (m)
1	1.3×10^{-7}	2.7×10^{-5}
2	1.9×10^{-7}	3.8×10^{-5}
30	7.4×10^{-7}	1.5×10^{-4}

abutting lath martensite or from austenite reversion without any preceding retained austenite. If the carbon-rich zone would be retained austenite the carbon profile in the austenite region would assume a V type distribution. This type of concentration profile would be characterized by a high content at the two martensite–austenite interfaces and a low content in the center of the austenite layer (hence "V"). Also, retained austenite would have the nominal composition, i.e. in the center of the retained austenite zone the carbon content should be 2 at.% or slightly above, as in Fig. 8a. This type of carbon distribution is not observed though. Instead, Fig. 8b shows that the carbon profile assumes a Λ shape within the austenite layer with a maximum carbon concentration above 8 at.%. It is hence plausible to assume that this profile is due to carbon segregation on a former martensite–martensite grain boundary according to the Gibbs adsorption isotherm. This means that during water quenching the carbon that is segregated at the martensite grain boundary has come from both sides. Therefore, the maximum carbon concentration revealed in Fig. 8b, which highly exceeds the equilibrium concentration that it would have been in the austenite, is in the center of the enrichment layer rather than at its rims. This means that during tempering austenite reversion starts in the center of this carbon-enriched area, i.e. at the former martensite–martensite grain boundary. The resulting average carbon concentration in this reverted austenite grain is very high, namely, 6.86 at.% (with a maximum above 8 at.%). The fact that the pronounced Λ shape of the carbon is preserved (frozen in) inside the austenite is due to the low mobility of carbon in austenite, Table 3. These observations suggest that the carbon-rich zone in Fig. 8b is a newly formed austenite layer. If the carbon-enriched area had been located between a martensite and an austenite grain, such as at the positions observed in Fig. 8a and c, the carbon atoms would have arrived only from one side, namely, from the martensite side (Fig. 9). The thickness of the newly formed reverted austenite layer in Fig. 8b is ~15 nm. With increasing tempering time, more reverted austenite is formed (Figs. 4 and 9).

In summary, the behavior of carbon in the current alloy can be described as follows: during quenching, carbon segregates to martensite–martensite grain boundaries (equilibrium segregation) or to martensite-retained austenite interfaces (partitioning plus kinetic freezing). In the first case (equilibrium segregation between two lath martensite zones) during tempering, these carbon-enriched areas in the martensite revert to austenite when the driving force is high enough, owing to the favorable nucleation barrier at the interfaces. In the second case (partitioning at retained austenite) the carbon enrichment leads to austenite growth according to local equilibrium. If the so-reverted austenite is located at or in the vicinity of the austenite–martensite phase boundary, carbon can diffuse from the reverted austenite further into the retained austenite provided that the tempering time is long enough. This carbon enrichment stabilizes the retained austenite. Also, this effect makes it generally difficult to distinguish reverted austenite from retained austenite (Fig. 9). After 1 min tempering, the reverted austenite has a high carbon content of 6.86 at.% (enrichment factor $\varepsilon = 3.61$). With increasing tempering time, the diffusion of carbon from reverted austenite into retained austenite leads to an increase in the carbon concentration of the retained austenite. After 30 min tempering, the carbon concentration in the retained austenite increases to an average value of 2.42 at.% (Fig. 8c). If the diffusion distance to the nearest phase boundary is too far, e.g. inside the bulk martensite, the high concentration of carbon leads to the formation of carbides inside the martensite.

After 30 min tempering time, the carbon content in the carbides is 25.1 at.%, as measured by APT. This value agrees with the stoichiometric content of carbon in M_3C (25 at.%). Due to the carbon partitioning to austenite, austenite reversion and the competing formation of carbides, the carbon content of the martensite continuously decreases during tempering. The amount of carbon in each phase before and after tempering is listed in Table 2 for the different stages. The other elements, for example chromium, have nearly the same content in both austenite and martensite. This means that during 400 °C tempering, medium range diffusion of carbon can be observed, but the substitutional elements only experience short distance diffusion. For all tempering conditions analyzed above we observe that not the nominal (global) but the local chemical potential of carbon directly at the martensite–austenite and martensite–martensite interfaces and the smaller nucleation energy at the interfaces determine the kinetics of austenite reversion. Similar trends were observed in maraging steels during aging [28,51,52].

In a thought experiment, assuming infinite mobility of the carbon when entering from martensite into austenite, the reversion would proceed more slowly owing to the smaller chemical driving force at the interface when carbon is distributed more homogeneously inside the austenite. In the current situations, however, carbon becomes trapped and highly enriched at the martensite–austenite interface owing to the partitioning and its low mobility within the austenite. This provides a much higher local driving force for austenite reversion. We refer to this mechanism as low temperature partitioning and kinetic freezing effect because the carbon is fast inside the martensite when leaving it but slow (and, hence, frozen) when entering the austenite. A similar effect was recently observed in Fe–Mn steels [28].

4.2. Transformation induced plasticity (TRIP) effect

During tensile testing, the volume fraction of austenite decreases not only in the quenched samples but also in the tempered samples (Fig. 6). When the brittle as-quenched sample failed at an early stage of loading (Fig. 2a, green curve), the amount of retained austenite had decreased from 18.9 to 10.8 vol.%. At failure most of the quenched-in martensite was still in the elastic regime. This means that stress-induced austenite-to-martensite

transformation prevailed since the material took nearly no plastic strain until fracture. After 400 °C austenite-reversion tempering, the ductility of the material improves drastically (Fig. 2). The EBSD results reveal that nearly all of the austenite transformed into martensite during tensile testing, especially in the near-fracture zones (Fig. 6a and b). This observation suggests that strain-induced austenite-to-martensite transformation (rather than stress-induced transformation) prevails in the tempered samples containing reverted nano-sized austenite.

The difference in the displacive deformation behavior between the as-quenched and tempered samples is due to the fact that directly after water quenching, the retained austenite is unstable due to its relatively low carbon content. In the as-quenched state (i.e. without tempering) the carbon content of the retained austenite is equal to the nominal composition after solution treatment. A relatively weak load is, hence, required to transform this retained and rather unstable austenite into martensite at the onset of the tensile test. Transforming a large amount of austenite at the same time, namely, at the beginning of deformation, promotes crack formation and premature failure. In contrast to this as-quenched and rather unstable austenite, subsequent tempering enriches the retained austenite with carbon due to partitioning. The higher carbon content stabilizes the retained and the reverted austenite so that austenite portions with different carbon content undergo the TRIP effect at different stages of deformation. These differences in carbon content of different austenite portions in the same sample are due to the fact that only the local chemical potential of the carbon at the hetero-interfaces determines the partitioning and reversing rates and, hence, also the exact carbon content of the abutting austenite. This means that retained and reverted austenite zones that are carbon-enriched through partitioning have a kinetically determined composition which is subject to local variations in the chemical potential (of carbon). This context explains the more continuous displacive transformation sequence in the tempered material and hence the observed ductility improvement.

Another aspect of the TRIP effect in this material is that austenite reversion, obtained from tempering, does not only stabilize the austenite via a higher carbon content but also increases its overall volume fraction at least after sufficient tempering time. Fig. 6a reveals that the austenite fraction increases from 18.9 vol.% after quenching to 29.7 vol.% after 2 min at 400 °C. Interestingly, after 1 min at 400 °C the austenite fraction did not change much. This means that for the short-annealing case (1 min) the austenite stability and its more sequential transformation as outlined above are more important for the ductilization than its mere volume fraction.

4.3. Precipitation development

The TEM and APT observations confirm that the carbides formed during tempering have are of M_3C type (instead of $M_{23}C_6$). The formation of M_3C is associated with a smaller loss of chromium from the matrix (into carbides) compared to $M_{23}C_6$-type carbides, which can have a high chromium content. Some authors found a sequence of carbide formation in Fe–Cr–C systems during tempering according to $MC \rightarrow M_3C \rightarrow M_7C_3 + M_{23}C_6 + M_6C$ [53]. In our study M_3C carbides prevailed up to 30 min annealing time. Samples taken from the as-quenched state show the highest hardness due to carbon in solid solution. The hardness decrease observed during tempering is related to carbide formation because carbon has a higher strengthening effect in solid solution than in the form of carbides. However, the small carbides (Fig. 8c) also contribute to the strength as observed with TEM (see Fig. 7b). The strain hardening rate decreases with increasing tempering time. This might be due to the coarsening of the carbides and due to the increase in the average carbide spacing (from ~40 nm after 1 min to ~80 nm after 30 min tempering at 400 °C). Further, we observe that the yield stress increases during tempering. This might be due to the change in the internal stress state of the martensite matrix. After water quenching, high elastic stresses prevail in the martensite. These lead to early microplastic yielding of the material prior to percolative bulk plastic yielding. During tempering, the internal stress state of the martensite is relaxed due to the escape of carbon. This leads to a delay in the yielding of the tempered samples.

4.4. Relationship between nanostructure and stress–strain behavior

In the preceding sections we presented experimental evidence of grain boundary segregation, hetero-interface partitioning, kinetic freezing, carbide precipitation, retained austenite formation and stabilization, austenite reversion, and the TRIP effect.

In this part we discuss the joint influence of these phenomena on the excellent strength–ductility profile of this steel (Fig. 2a and d).

We differentiate between mechanisms that provide higher strength and those promoting ductility: the most relevant phase responsible for the high strength of the steel after heat treatment is the relaxed martensite. The quenched-in martensite with an extrapolated tensile strength of more than 2300 MPa (approximated from hardness data) is very brittle. Already a very modest heat treatment of 1 min at 400 °C though (Fig. 2a) provides sufficient carbon mobility. This leads to carbon redistribution (carbide formation, grain boundary segregation, dislocation decoration, martensite–austenite interface segregation, austenite solution) and thus to a reduction in the internal stresses of the martensite. The reduced carbon content renders the martensite into a phase that can be plastically deformed without immediate fracture. The second contribution to the increase in strength are the nanoscaled carbides which provide Orowan strengthening, Figs. 7 (TEM) and Fig. 8c (APT). Their average spacing increases

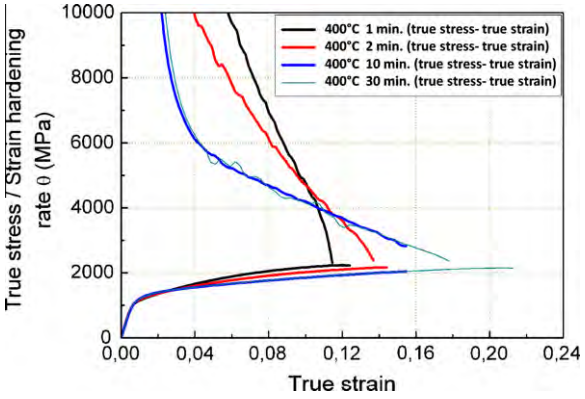

Fig. 10. True stress–true strain curves and corresponding strain hardening curves for the steel after 400 °C heat treatment at different times. The data reveal that the tempering, associated with the increase in the austenite content via austenite reversion, yields higher strain hardening reserves at the later stages of deformation due to the TRIP effect.

from ~50 nm (1 min at 400 °C) to ~80 nm (30 min at 400 °C), Fig. 8b. These two effects, i.e. conventional martensite strength (via high dislocation density, high internal interface density, internal stresses, solid solution strengthening) and Orowan strengthening explain the high strength of the material, but they do not explain its high ductility.

In this context the TRIP effect, i.e. the displacive transformation of retained and reverted austenite, becomes relevant: Fig. 6a reveals a drop in the austenite content from 29.7 to ~2.7 vol.% during deformation for the sample heat treated at 400 °C for 2 min. Fig. 10 shows the true stress–true strain curves and their corresponding derivatives (strain hardening) after 400 °C heat treatment at different times. The data reveal that the tempering, which increases the austenite content via reversion, leads indeed to higher strain hardening reserves at the later stages of deformation due to the TRIP effect, Fig. 6b. Since longer heat treatments lead to higher volume fractions of reverted austenite the TRIP-related strain hardening assumes a higher level for these samples (Fig. 10).

Another important effect that might promote ductility in this context is the wide distribution of the austenite dispersion and stability (carbon content) which are both characteristic for this material. As revealed in Fig. 8 we can differentiate three types of austenite, Fig. 9a. The first type is the as-quenched retained austenite with the nominal carbon content and relatively low stability. The second one is retained austenite, which assumes an increased carbon content due to partitioning during quenching and particularly during heat treatment and has thus higher stability against

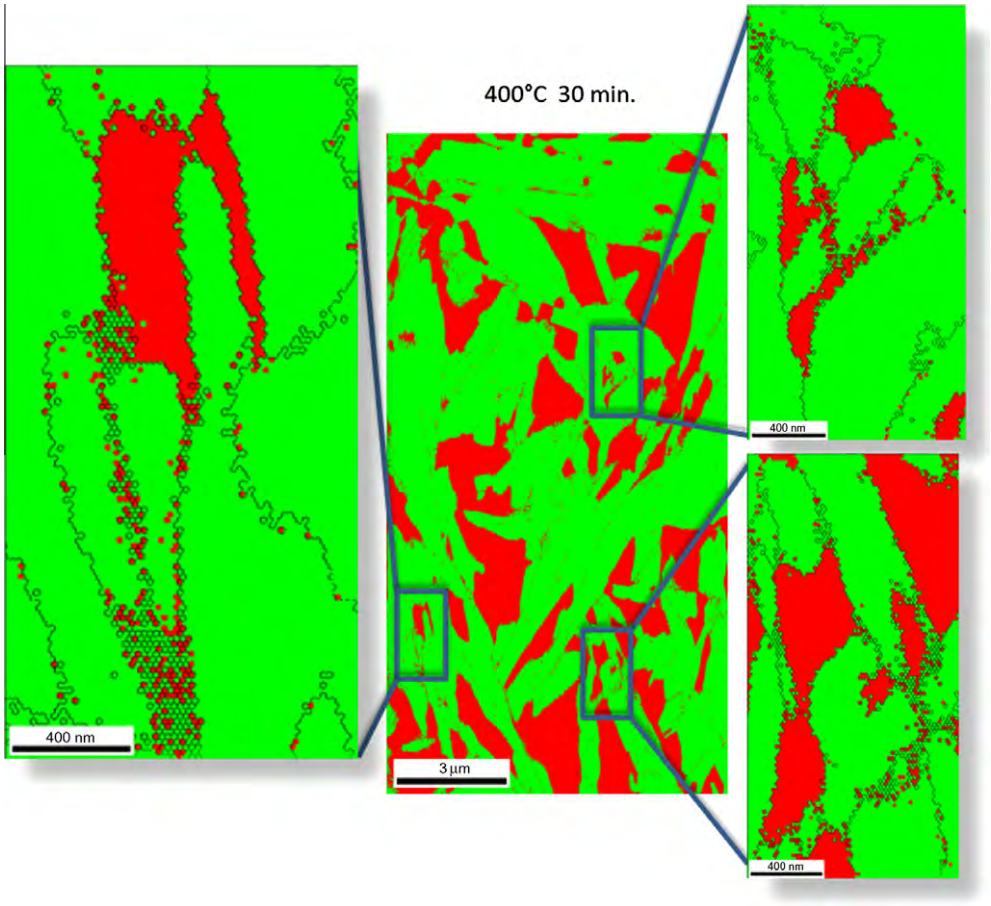

Fig. 11. High-resolution EBSD map (20 nm step size) of the sample tempered at 400 °C for 30 min. The map shows that on some martensite grain boundaries a very thin reverted austenite layer exists. This thin austenite seam can act as a compliance or respectively repair layer against damage percolation entering from the martensite grain. Austenite: red; martensite: green.

displacive transformation. The third type of austenite is the reverted one. These three types of austenite have different carbon concentration, volume fraction and size. Both carbon content and size affect austenite stability. This means that the displacive transformation during tensile testing and the associated accommodation plasticity occur more gradually upon loading compared to a TRIP effect that affects a more homogeneous austenite. We refer to this mechanism as a heterogeneous TRIP effect.

Another important aspect is the composite-like architecture of the reverted austenite, which is located at the martensite–martensite and at the martensite–austenite interfaces in the form of nanoscaled seams (see Figs. 8 and 11). Such a topology might act as a soft barrier against incoming cracks or stress–strain localizations from the martensite. We hence speculate that the austenite seam is a compliance or respectively repair layer that can immobilize defects through its high formability and prevent cracks from percolating from one martensite grain into another (Fig. 11). In this context it is important to note that conventional martensite–martensite interfaces often have a small-angle grain boundary between them which facilitates crack penetration from one lath to another. Here, a compliant austenite seam between the laths might hence be very efficient in stopping cracks.

We emphasize this point since the increase in macroscopic ductility can generally be promoted by both an increase in strain hardening at the later stages of deformation and mechanisms that prevent premature damage initiation.

5. Conclusions

We studied carbon partitioning, retained austenite, austenite stabilization, nanoscale austenite reversion, carbide formation and kinetic freezing of carbon during heat treatment of a martensitic stainless steel Fe–13.6Cr–0.44C (wt.%). The main results are as follows:

1. Austenite formation in carbon-enriched martensite–austenite interface areas is confirmed by XRD, EBSD, TEM and APT. Both the formation of retained austenite and austenite reversion during low-temperature partitioning is discussed. The enrichment of carbon at martensite–martensite grain boundaries and martensite-retained austenite phase boundaries provides the driving force for austenite reversion. The reverted austenite zones have nanoscopic size (~15–20 nm). The driving forces for austenite reversion are determined by local and not by global chemical equilibrium.
2. Martensite-to-austenite reversion proceeds fast. This applies to both the formation of reversed austenite at retained austenite layers and austenite reversion among martensite laths. The volume fraction of austenite has nearly doubled after 2 min at 400 °C.
3. The carbides formed during tempering have M_3C structure. With increasing tempering time the dispersion of the carbides decreases due to the Gibbs–Thomson effect.
4. During tempering between 300 °C and 500 °C carbon redistributes in three different ways. During quenching, in the vicinity of martensite–austenite interfaces, carbon segregates from the supersaturated martensite to both the hetero-interfaces and homophase grain boundaries. During tempering, carbon continuously partitions to martensite–austenite interfaces, driving the carbon-enriched areas towards austenite reversion (irrespective of whether the nucleation zones were initially retained or reversed austenite). Carbon inside martensite, far away from any interfaces, tends to form M_3C carbides. This means that carbon segregates to martensite grain boundaries, to martensite–austenite interfaces, and forms carbides.
5. We differentiate between three different types of austenite, namely, first, as-quenched retained austenite with nominal carbon content and low stability; second, retained austenite with increased carbon content and higher stability due to partitioning according to the local chemical potential of carbon; and third, reverted austenite.
6. The nanoscale structural changes lead to drastic improvements in the mechanical properties. A sample after 1 min tempering at 400 °C has 2 GPa tensile strength with 14% total elongation. The strength increase is attributed to the high carbon content of the martensite and the interaction between dislocations and nano-sized carbides. The TRIP effect of the austenite during deformation, including the reverted nanoscale austenite, contributes to a strain-hardening capacity and, hence, promotes the ductility. Also, the topology of the reverted austenite is important: we suggest that the nanoscaled seam topology of the austenite surrounding the martensite acts as a soft barrier which has compliance and repair function. This might immobilize defects and prevent cracks from growth and inter-grain percolation.
7. We attribute the fast nanoscale austenite reversion to an effect that we refer to as kinetic freezing of carbon. This means that the carbon is fast inside the martensite when leaving it but slow (and hence frozen) when entering the austenite. This means that carbon becomes trapped and highly enriched at the martensite–austenite interfaces owing to its low mobility within the austenite during low-temperature partitioning. This provides a much higher local driving force for austenite reversion. This means that the formation of nanoscaled reverted austenite depends mainly on the local but not on the global chemical potential of carbon at internal interfaces.

Acknowledgement

The authors are grateful for discussions on carbon partitioning and martensite tempering with Professor George D.W. Smith from Oxford University.

References

[1] Zou D, Han Y, Zhang W, Fang X. J Iron Steel Res Int 2010;17(8):50.
[2] Rodrigues CAD, Lorenzo PLD, Sokolowski A, Barbosa CA, Rollo JMDA. Mater Sci Eng A 2007;460–461:149.
[3] Karlsen M, Grong O, Soefferud M, Hjelen J, Roervik G, Chiron R. Metall Mater Trans 2009;40A:310.
[4] Pieta G, Leite R, Kwietniewski C, Clarke T, Strohaecker T. J Mater Eng Perform 2010;19(9):1318.
[5] Kurdjumov GV. Twelfth Hatfield Memorial Lecture; 1959.
[6] Clarke AJ, Speer JG, Miller MK, Hackenberg RE, Edmonds DV, Matlock DK, et al. Acta Mater 2008;56:16.
[7] Malakondaiah G, Srinivas M, Rao PR. Prog Mater Sci 1997;42:209.
[8] Speer JG, Matlock DK, Cooman BCD, Schroth JG. Acta Mater 2003;51:2611.
[9] Edmonds DV, Hea K, Rizzo FC, Cooman BCD, Matlock DK, Speer JG. Mater Sci Eng A 2006;438–440:25.
[10] Tomimura K, Takaki S, Tanimoto S, Tokunaga Y. ISIJ Int 1991;31:721.
[11] Tomimura K, Takaki S, Tokunaga Y. ISIJ Int 1991;31:1431.
[12] Takaki S, Tomimura K, Ueda S. ISIJ Int 1994;34:522.
[13] Nakada N, Tsuchiyama T, Takaki S, Hashizume S. ISIJ Int 2007;47:1527.
[14] Furuhara T, Kikumoto K, Saito H, Sekine T, Ogawa T, Morito S, et al. ISIJ Int 2008;48:1038.
[15] Nakada N, Tsuchiyama T, Takaki S, Miyano N. ISIJ Int 2011;51:299.
[16] Nayak SS, Anumolu R, Misra RDK, Kim KH, Lee DL. Mater Sci Eng 2008;A498:442.
[17] Cerezo A, Godfrey TJ, Smith GDW. Rev Sci Instrum 1988;59:862.
[18] Blavette D, Deconihout B, Bostel A, Sarrau JM, Bouet M, Menand A. Rev Sci Instrum 1993;64:2911.
[19] Miller MK, Cerezo A, Hetherington MG, Smith GDW. Atom probe field ion microscopy. Oxford: Oxford University Press; 1996.
[20] Thuvander M, Miller MK, Stiller K. Mater Sci Eng 1999;A270:38.
[21] Miller MK. Atom probe tomography analysis at the atomic scale. New York: Kluwer Academic/Plenum; 2000.
[22] Kelly TF, Miller MK. Rev Sci Instrum 2007;78:031101.
[23] Seidman D. Annu Rev Mater Sci 2007;37:127.
[24] Miller MK, Forbes RG. Mater Charact 2009;60:461.
[25] Marquis EA, Miller MK, Blavette D, Ringer SP, Sudbrack CK, Smith GDW. MRS Bull 2009;34:725.
[26] Pereloma EV, Stohr RA, Miller MK, Ringer SP. Metall Mater Trans 2009;40A:3069.
[27] Sauvage X, Lefebvre W, Genevois C, Ohsaki S, Hono K. Scripta Mater 2009;60:1056.
[28] Dmitrieva O, Ponge D, Inden G, Millán J, Choi P, Sietsma J, et al. Acta Mater 2011;59:364.
[29] Gerezo A, Godfrey TJ, Smith GDW. Rev Sci Instrum 1988;59:862.
[30] Raabe D, Choi PP, Li YJ, Kostka A, Sauvage X, Lecouturier F, et al. MRS Bull 2010;35:982.
[31] Ohsaki S, Raabe D, Hono K. Acta Mater 2009;57:5254.
[32] Choi P, da Silva M, Klement U, Al-Kassab T, Kirchheim R. Acta Mater 2005;53:4473.
[33] Thermo-Calc User's Guide, Version R. Stockholm: Thermo-Calc software AB and foundation of computational thermodynamics; 1995–2006.
[34] Thermodynamic database TCFE5-TCS steels/Fe-alloys database, version 5, Thermo-Calc software. <http://www.Thermocalc.com>.
[35] Sato H, Zaefferer S. Acta Mater 2009;57:1931.
[36] Jiménez JA, Carsí M, Frommeyer G, Knippscher S, Wittig J, Ruano OA. Intermetallics 2005;13:1021.
[37] Rühle M. Metallography and microstructures. In: Transmission electron microscopy. ASM Handbook, vol. 9. Materials Park (OH): ASM International; 1995.
[38] Shtansky DV, Nakai K, Ohmori Y. Acta Mater 2000;48:1679.
[39] Miyamoto G, Usuki H, Li ZD, Furuhara T. Acta Mater 2010;58:4492.
[40] Speer JG, Edmonds DV, Rizzo FC, Matlock DK. Curr Opin Solid State Mater Sci 2004;8:219.
[41] Streicher AM, Speer JG, Matlock DK, De Cooman BC. In: Proceedings of the international conference on advanced high strength sheet steels for automotive applications, vol. 51; 2004.
[42] Zhong N, Wang XD, Wang L, Rong YH. Mater Sci Eng 2009;A506:111.
[43] MCLellan RB, Wasz ML. J Phys Chem Solids 1993;54:583.
[44] Haasen P. Physikalische Metallkunde. Berlin: Springer-Verlag; 1974. p. 173.
[45] Zhu C, Xiong XY, Cerezo A, Hardwicke R, Krauss G, Smith GDW. Ultramicroscopy: IFES 2006, proceedings of the 50th international field emission symposium/19th IVNC 107; 2007. p. 808–12.
[46] Sarikaya M, Thomas G, Steeds JW, Barnard SJ, Smith GDW. Proc solid–solid phase transformations conf. Pittsburgh (PA), Warrendale (PA): The Metallurgical Society of the AIME; 1981.
[47] Barnard SJ, Smith GDW, Sarikaya M, Thomas G. Scripta Metall 1981;15:387.
[48] Bhadeshia HKDH. Met Sci 1983;17:151.
[49] Bhadeshia HKDH. Met Sci 1981;15:175.
[50] Thomas G, Sarikaya M, Smith GDW, Barnard SJ. Advances in the physical metallurgy and applications of steels. London: The Metals Society; 1983. p. 259–65
[51] Höring S, Abou-Ras D, Wanderka N, Leitner H, Clemens H, Banhart J. Steel Res Int 2009;80:84.
[52] Schnitzer R, Radis R, Nöhrer M, Schober M, Hochfellner R, Zinner S, et al. Mater Chem Phys 2010;122:138.
[53] Yan F, Shi H, Fan J, Xu Z. Mater Charact 2008;59:883.

Available online at www.sciencedirect.com
ScienceDirect
Acta Materialia 59 (2011) 364–374
Acta MATERIALIA
www.elsevier.com/locate/actamat

Chemical gradients across phase boundaries between martensite and austenite in steel studied by atom probe tomography and simulation

O. Dmitrieva [a], D. Ponge [a], G. Inden [a], J. Millán [a], P. Choi [a], J. Sietsma [b], D. Raabe [a,*]

[a] Max-Planck-Institut für Eisenforschung, Max-Planck-Str. 1, 40237 Düsseldorf, Germany
[b] Delft University of Technology, Faculty 3mE, Dept. MSE, 2628 CD Delft, The Netherlands

Received 14 June 2010; received in revised form 2 September 2010; accepted 22 September 2010
Available online 18 October 2010

Abstract

Partitioning at phase boundaries of complex steels is important for their properties. We present atom probe tomography results across martensite/austenite interfaces in a precipitation-hardened maraging-TRIP steel (12.2 Mn, 1.9 Ni, 0.6 Mo, 1.2 Ti, 0.3 Al; at.%). The system reveals compositional changes at the phase boundaries: Mn and Ni are enriched while Ti, Al, Mo and Fe are depleted. More specific, we observe up to 27 at.% Mn in a 20 nm layer at the phase boundary. This is explained by the large difference in diffusivity between martensite and austenite. The high diffusivity in martensite leads to a Mn flux towards the retained austenite. The low diffusivity in the austenite does not allow accommodation of this flux. Consequently, the austenite grows with a Mn composition given by local equilibrium. The interpretation is based on DICTRA and mixed-mode diffusion calculations (using a finite interface mobility).

Keywords: Precipitation hardening; High-strength steels; TRIP; Aging; Atom probe tomography

1. Introduction

Mn is among the most important alloying elements for the design of advanced high-strength steels, as it affects the stabilization of the austenite, the stacking fault energy and the transformation kinetics [1–11]. Besides these global mechanisms which are exploited particularly in designing steels with transformation-induced plasticity (TRIP) and twinning-induced plasticity (TWIP) effects, Mn has very low diffusion rates in the austenite and a high segregation or respectively partitioning tendency at interfaces. This context makes Mn (as well as the other elements discussed in this paper) a very interesting candidate for an atomic-scale study of compositional changes across austenite/martensite interfaces.

The specific material studied in this work is a precipitation-hardened alloy that we refer to as maraging-TRIP steel. It was developed by combining the TRIP mechanism with the maraging (i.e. martensite aging) effect [12,13]. The TRIP effect exploits the deformation-stimulated transformation of metastable retained austenite into martensite and the resulting plasticity required to accommodate the transformation misfit [1–7]. The maraging effect uses the hardening of the heavily strained martensite through the formation of nanosized intermetallic precipitates during aging heat treatment. The maraging-TRIP steels used in this work reveal the surprising property that both strength and total elongation increase upon aging, reaching an ultimate tensile strength of nearly 1.3 GPa at an elongation above 20% [12–14].

The studied alloy contains 12.2 at.% Mn, low carbon content (0.05 at.%) and minor additions of Ni, Ti, Al and Mo. Its microstructure after aging is characterized by the presence of up to 15–20 vol.% austenite, a fine martensite matrix, and dispersed nanoscaled Ni–Al–Mn-enriched zones [12–14]. Besides the increase in strength, a simultaneous increase of ductility was found upon aging. This effect is interpreted in terms of sluggish reaustenitization during aging and the effect of tempering of the as-quenched

* Corresponding author. Tel.: +49 2116792325; fax: +49 2116792333.
E-mail address: d.raabe@mpie.de (D. Raabe).

1359-6454/$36.00 © 2010 Acta Materialia Inc. Published by Elsevier Ltd. All rights reserved.
doi:10.1016/j.actamat.2010.09.042

martensite [14]. Partial retransformation into austenite (besides the existing retained austenite) by a reconstructive mechanism involving Mn partitioning might be responsible for this process.

In order to elucidate this transformation phenomenon, particularly the role of Mn, we focus in this work on the analysis of nanoscale elemental diffusion gradients across abutting martensite/retained austenite phase areas. Atom probe tomography (APT) is a characterization technique that provides three-dimensional elemental mapping with nearly atomic resolution and gives information on the topology of interfaces and local chemical gradients [15–27]. We conducted APT using an advanced local electrode atom probe device (Imago LEAP 3000X HR). Both the two phases (austenite, martensite) and the interfaces between them were chemically analyzed at the atomic scale. Additionally, statistical thermodynamic and kinetic calculations were conducted for the given initial and boundary values using Thermo-Calc [28,29] in conjunction with the kinetic simulation software DICTRA [30–32] and with a mixed-mode kinetic approach that considers finite interface mobility [33,34].

2. Experimental

The investigated maraging-TRIP steel with a composition of 12.2 Mn, 1.9 Ni, 0.6 Mo, 1.2 Ti, 0.1 Si, 0.3 Al and 0.05 C (at.%) was melted and cast in a vacuum induction furnace. Before final age hardening, a solution treatment was performed in Ar atmosphere at 1050 °C for 0.5 h followed by water quenching. This led to a microstructure consisting of martensite and retained austenite. Final aging was conducted for 48 h at 450 °C. After aging the sample was quenched in water. Details of the alloy preparation have been published elsewhere [12–14].

APT samples were prepared by electrochemical polishing and subsequent sharpening using a focused ion beam device. Pulsed-laser APT was performed using a local electrode atom probe (LEAP™ 3000X HR, Imago Scientific Instruments) tomograph at a specimen temperature of 54 K. An ultrafast pulsed laser of ~10 ps pulse width and 532 nm wavelength was applied at a frequency of 250 kHz. The laser pulse energy was set to 0.4 nJ. The detection rate (target evaporation rate) amounted to 5 atoms per 1000 pulses. Data analysis was performed using the IVAS® software from Imago Scientific Instruments. The specific APT data set analyzed in this work contains about 70 million ions. We used an evaporation field constant of 26 V nm^{-1} for the atomic reconstruction.

Phase fractions and the elemental compositions in thermodynamic equilibrium were calculated using the software Thermo-Calc [28]. The software DICTRA [30–32] and a mixed-mode kinetic approach including finite interface mobility [33,34] were applied to simulate diffusion-controlled phase transformations. The simulations were performed using the thermodynamic database TCFE6 [29] and the mobility database MOB2.

3. Results

3.1. Analysis of the 3-D atom probe reconstruction

3.1.1. Manganese distribution

Fig. 1a gives a microstructure overview of the maraging-TRIP steel after quenching and subsequent aging (48 h at 450 °C). The upper micrograph is an electron backscatter diffraction (EBSD) image where the cubic martensite is plotted green and the retained austenite red (the retained austenite was already present in the as-quenched state before aging [12–14]). The middle image shows a transmission electron microscopy (TEM) micrograph with precipitate-containing martensite and precipitate-free austenite. The bottom image shows an APT reproduction which includes both martensitic and austenitic zones. Ni atoms are shown in cyan and Mn atoms in blue. The yellow isosurfaces indicate 18 at.% Mn. Note that the three images reveal the hierarchy of the microstructure but the individual images were not taken at precisely the positions indicated. Fig. 1b gives a local overview of the distribution of the Ni and Mn atoms in the center of the APT data set presented in Fig. 1a. For clarity, only a longitudinal section of 20 nm thickness is shown, in which only 7.8% of all detected Ni (cyan) and 1.5% of all Mn (dark blue) atoms are displayed. The whole analysis volume is about 4×10^5 nm^3. Fig. 1a and b show three main zones that are separated by inclined plate-like Mn accumulations. Ni-rich nanoprecipitates are dispersed in the left- and right-hand areas. Besides the Ni atoms, higher amounts of Al, Mn, and Ti were also detected in these clusters (Table 1). In the center part between the Mn-enriched plates, no precipitates appear. This observation strongly suggests that this zone corresponds to austenite, whereas the abutting areas containing precipitates are martensitic. Correlative TEM investigations conducted on this alloy in the same aging state (48 h, 450 °C) support the suggestion that the nanoparticles that are enriched in Ni, Al and Mn formed in the martensitic microstructure while the retained austenite (total volume fraction about 15–20 vol.%) was precipitate-free [13,14] (Fig. 1a). From these observations we conclude that the present volume probed by APT contains an austenitic grain enclosed between two martensitic grains. Quantitative chemical analysis of the interfaces between austenite and martensite was performed using 1-D concentration profiles computed over the region of interest (transparent cylindrical units) (Fig. 2a). We calculated the Mn content averaged over the 0.5 nm thick cross-sections of the cylinders at a profile step size of 0.5 nm. For both interfaces, a strong increase in the Mn content up to 27 at.% was observed (Fig. 2b). Away from the interface, the content of Mn within the austenite amounts to about 12 at.% which is close to the average chemical composition of the alloy. Within the bulk martensite the Mn content amounts to about 10 at.%. Mn depletion in the martensite down to 6 at.% was observed close to the interface.

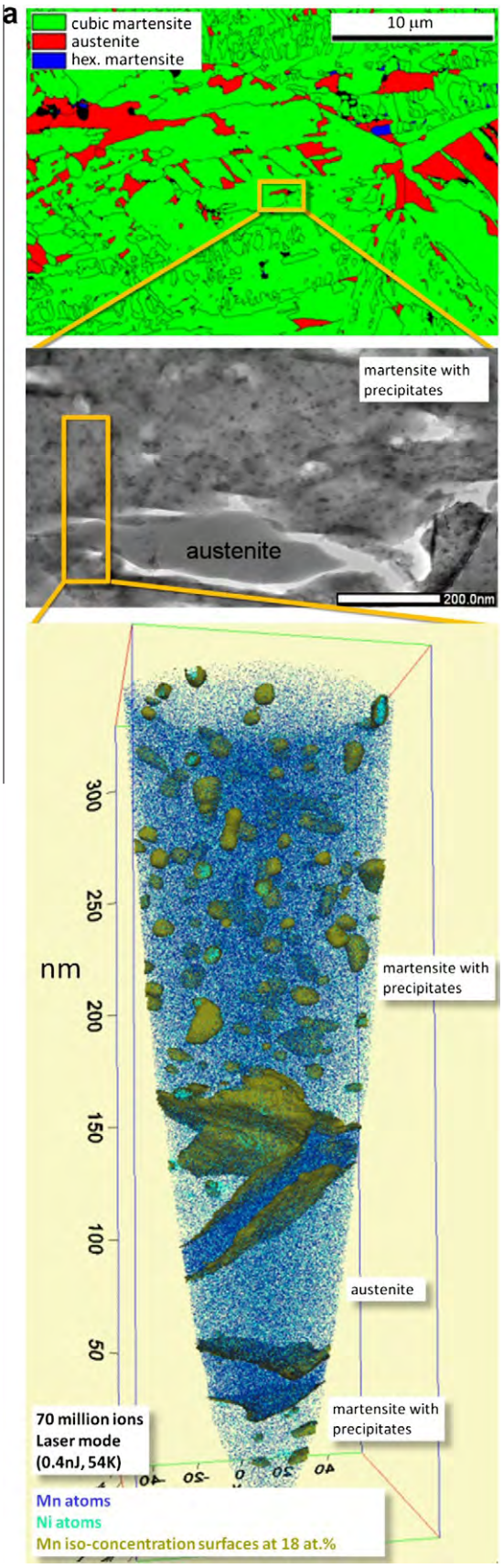

In order to exclude the contribution of the precipitates from the chemical profile within the martensitic area, we separately measured the 1-D concentration profiles within the martensitic matrix after removing the precipitate zones from the analysis volume (described in detail below). The reason for this procedure is that the martensitic area is in itself a two-phase region consisting of martensite and precipitates. Hence, we aim with this method at the separation of the martensite elemental composition and the precipitate elemental composition. These two corrected profiles, containing only the martensite composition, are included in Fig. 2b on the left-hand side in the martensitic area marked "M". The curves are separated from the profile across the interface and in the austenite ("A").

3.1.2. Distribution of other alloying elements

Fig. 3 shows the concentration profiles for the other alloying elements across one of the martensite/austenite phase boundary zones. The area selected is indicated by "Mn layer 2" in Fig. 2a. In addition to Mn (which is studied here in more detail owing to its relevance for high-strength steels), all other elements also reveal a strong partitioning between the two phases. While Mn is enriched by about 2.1 times within the interface boundary layer relative to its average content in the alloy, Ni is accumulated 1.2 times in the same zone. All other elements are depleted in the interface zone: Ti decays by a factor of about 6.9 times relative to the average content, Al by a factor of 6.6, Mo 2.0 and Fe 1.2. Another important observation is the large chemical width of the phase boundary zone: the enrichment zone associated with the austenite/martensite interface extends over a length of about 20 nm normal to the boundary segment studied.

3.1.3. Chemical analysis of the nanoparticles and of the alloy matrix

The nanoparticles detected in the martensite were analyzed using a cluster search algorithm implemented in the

Fig. 1. (a) Microstructure overview of the maraging-TRIP steel after quenching and subsequent aging (48 h at 450 °C). The upper micrograph is an EBSD image where the cubic martensite is plotted green and the retained austenite red (the retained austenite was already present in the as-quenched state before aging). The middle image shows a TEM micrograph with precipitate-containing martensite and precipitate-free austenite. The bottom image shows an APT reproduction which includes both martensitic and austenitic zones. Ni atoms are given in cyan and Mn atoms in blue. The yellow isosurfaces indicate 18 at.% Mn. Note that the three images correctly reveal the hierarchy of the microstructure but the individual images were not taken at precisely the positions indicated. (b) 20 nm thick middle layer slice through the APT reconstruction of the maraging-TRIP steel shown in (a). Ni atoms (cyan symbols) are accumulated in precipitates in the martensitic grains (left- and right-hand side). The precipitate-free austenite (right-hand center) is bordered by plate-like zones that are characterized by strong Mn enrichment (blue symbols). Red dotted lines illustrate the suggested crystallographic positions of the phase boundaries between martensite and austenite.

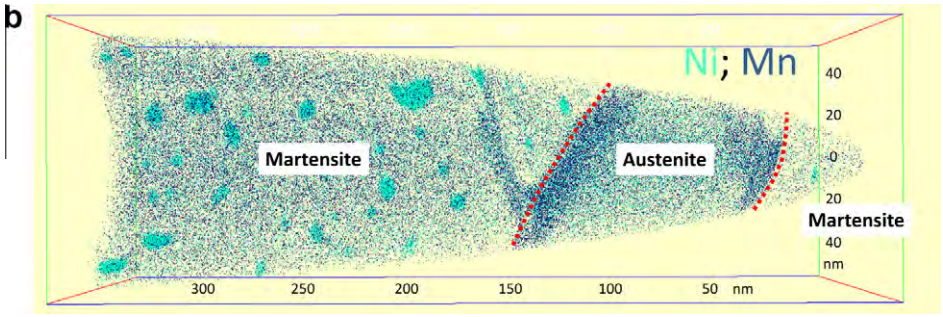

Fig. 1 (*continued*)

Table 1
(Experimental results) Elemental composition of the alloy measured globally on the as-cast sample using wet chemical analysis (total content melt) and obtained locally from the APT measurement on the specimen volume containing a martensite/austenite phase boundary of 450 °C/48 h aged steel (total content APT; martensite; austenite). Enrichment factors are calculated as the relation between the elemental content within the particles to the total content of element in the alloy.

Chemical content, at.%	Total content (melt)	Total content (in APT)	Martensite				Austenite
			Total	Matrix	Particles	Enrichment factor	
Fe	83.71	83.21	84.38	86.82	40.32	0.48	83.53
Mn	12.19	12.34	11.10	10.29	26.07	2.35	12.17
Ni	1.90	2.26	2.32	0.99	25.79	11.12	2.01
Ti	1.17	1.10	1.09	0.98	3.23	2.96	1.14
Mo	0.58	0.60	0.60	0.62	0.27	0.45	0.60
Al	0.31	0.33	0.34	0.14	4.08	12.0	0.38
Si	0.10	0.16	0.15	0.14	0.24	1.6	0.16
C	0.046	0.006	0.001	0.001	0		0.006

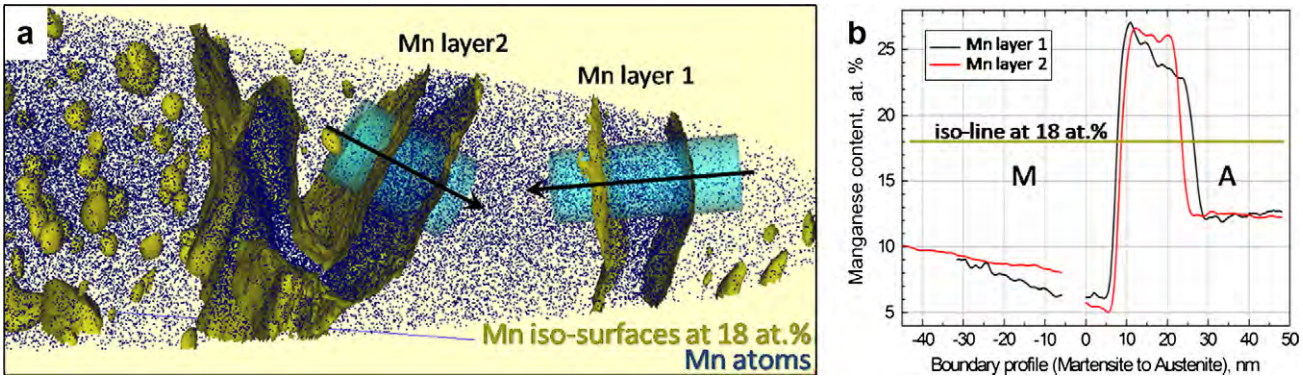

Fig. 2. Quantitative chemical analysis of the interface regions between martensite and austenite (APT results). (a) Atomic map section showing both phase boundaries. Isoconcentration surfaces for the chemical distribution of Mn atoms (blue) were plotted at 18 at.% (yellow). 1-D profiles along the cylindrical units (cyan) provide chemical gradients of elements across the phase boundaries. (b) Gradients in Mn content across the phase boundaries (martensite to austenite).

IVAS® software. For cluster identification, the following parameters as identified by the optimization procedure performed within the cluster search algorithm were used: $d_{max} = 0.6$ nm (maximal distance between the solute atoms belonging to a cluster), $N_{min} = 50$ (minimal number of solute atoms in the cluster), $L = 0.57$ nm (envelope distance: all non-solute ions within a distance L of solute ions are included in the cluster), $d_e = 0.55$ nm (erosion distance: all clustered non-solute ions within a spacing d_e of any ion outside of its assigned cluster are removed from the particle). The cluster search was conducted for the distribution of the Ni atoms that are enriched in the particles. The chemical composition of the clusters is summarized in Table 1. The calculation of the enrichment factors that were determined as a relation between the content within the particles relative to the total content of the same elements in the entire alloy reveals a strong precipitation character of Ni and Al atoms within the clusters. Enrichment in Mn and Ti was also detected in the particles. For estimating the chemical composition of the surrounding matrix (without the precipitates), the detected clusters were removed from the overall reconstruction, and the composition of the residual matrix volume was calculated again. For this purpose, different cluster search parameters were

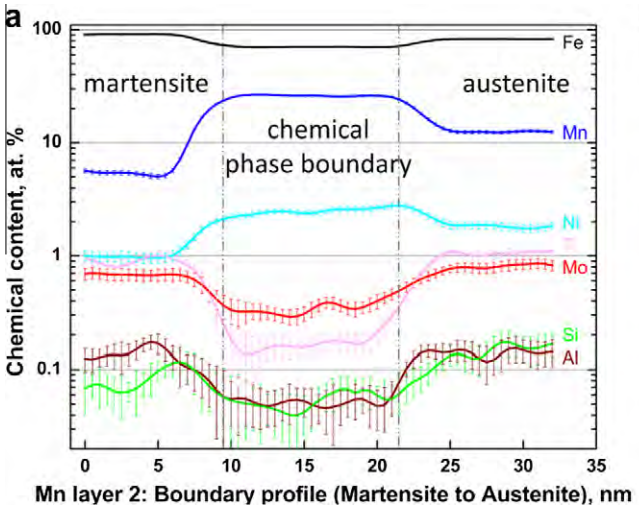

b

at. %	Mean content in the layer	Total content (APT)	Enrichment within the layer, times
Mn	26.5 ± 1.5	12.34	2.1
Ni	2.6 ± 0.3	2.26	1.2

at. %	Mean content in the layer	Total content (APT)	Depletion within the layer, times
Fe	70.4 ± 0.3	83.21	1.2
Ti	0.16 ± 0.02	1.10	6.9
Mo	0.30 ± 0.05	0.60	2.0
Al	0.05 ± 0.01	0.33	6.6
Si	0.04 ± 0.01	0.16	4

Fig. 3. Experimental APT results. (a) Concentration profiles for all elements across one of the martensite/austenite phase boundaries (see interface referred to as "Mn layer 2" in Fig. 2a). (b) Quantitative characterization of the enrichment or depletion of the elements within the chemical phase boundary.

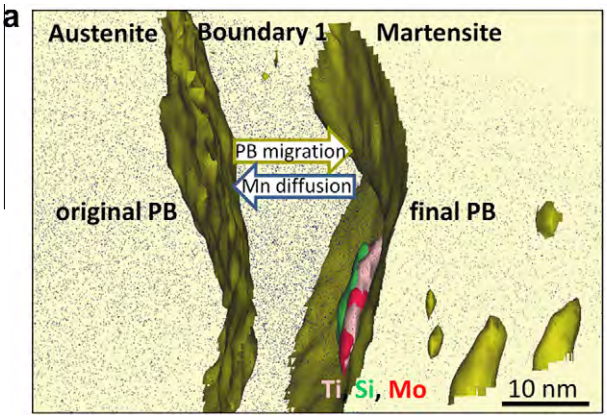

b

at. %	Segregation content	Total content (APT)	Enrichment factor
Fe	53.29	83.21	0.64
Mn	23.03	12.34	1.87
Ni	3.13	2.26	1.38
Ti	11.92	1.10	**10.83**
Mo	5.52	0.60	**9.20**
Al	0.08	0.33	0.24
Si	3.03	0.16	**18.95**

Fig. 4. Compositional changes in the austenite/martensite interface region (APT results). (a) Atomic map section showing a phase boundary between austenite (left) and martensite (right). Isoconcentration surfaces plotted at 18 at.% Mn (dark yellow) correspond to the highest Mn gradient and indicates the positions of the original and the final phase boundaries (PB) (see text). The compositional changes at the final PB are revealed by plotting isoconcentration surfaces for Ti (at 8 at.%), Mo (at 5 at.%), and Si (at 3 at.%). (b) Chemical composition of the Ti–Mo–Si-rich partitioning estimated from the APT data.

used ($d_{max} = 1.0$ nm, $N_{min} = 50$, $L = 0.97$ nm, $d_e = 0.95$ nm) which allow inclusion of more material in the clusters and ensure that after exclusion of the clusters no residual material remains. The composition of the matrix without the particles is presented in Table 1.

3.1.4. Observation of compositional changes within the martensite/austenite interface region

By computing the isoconcentration surfaces for all solute elements from the experimental data we detected changes in composition of Mo, Ti and Si in the martensite/austenite interface region. Fig. 4a shows isosurfaces for Mo, Ti and Si concentrations of 5, 8 and 3 at.%, respectively. The position of this region overlaps with the position of the isoconcentration surface plotted at 18 at.% Mn and, more specifically, corresponds to the range of the highest Mn gradient. A similar region with nearly the same content and element distribution was also observed at the other martensite/austenite interface (not shown in Fig. 4a). The average chemical composition within the region is summarized in the table in Fig. 4b. The enrichment factors reveal strong compositional increase of Ti, Mo and Si, and strong depletion of Al. The relative concentrations of Fe, Ti and Mo within that region are 75:17:8, suggesting the formation of a Laves phase, which according to Thermo-Calc should be formed at a composition of Fe 67 at.%, Ti 23 at.%, and Mo 10 at.%.

3.2. Thermodynamic calculations

3.2.1. Prediction of the phase equilibrium composition

Using Thermo-Calc, the equilibrium compositions of stable phases at 450 °C were calculated taking into account the total nominal composition of the alloy and all possible

Table 2
Equilibrium phases at 450 °C in the investigated maraging-TRIP steel as obtained by Thermo-Calc calculations quantified in terms of molar fractions (TCFE6 database).

Phase	Mole fraction	Fe	Mn	Ni	Ti	Mo	Al	Si	C
bcc	0.576	95.972	3.064	0.098	0.165	0.113	0.494	0.094	–
fcc	0.377	67.251	27.569	4.887	0.053	0.077	0.041	0.122	–
Laves	0.046	65.911	0.763	–	22.321	11.005	–	–	–
TiC	0.001	–	–	–	54.046	–	–	–	45.954

competing phases available in the database [28,29]. The results of the Gibbs energy minimization technique predicts four phases in thermodynamic equilibrium: body-centered cubic (bcc: ferrite/martensite), face-centered cubic (fcc: austenite), TiC and a Laves phase. The calculated molar fractions for each phase and their chemical compositions are listed in Table 2. It is important to point out that such calculation does not predict the presence of the nanosized particles due to the limited availability of thermodynamic data related to various other possible intermetallic phases in complex maraging steels. At a temperature of 450 °C, a Mn content of about 26.7 and 3.3 at.% is expected in the retained austenite and in the ferrite (martensite), respectively.

3.2.2. Diffusion simulations using DICTRA

For simulation of the kinetic behavior in the vicinity of the martensite/austenite interface, linear cell geometry is appropriate [30]. The kinetic effects to be studied are confined to very small spatial ranges. Within this scale the interfaces are planar in shape and their movement is vertical to the plane. The size of the cell was chosen as 20 μm (see Fig. 5a). The cell was divided into two regions, one corresponding to ferrite, the other to austenite. The space in each region is discretized as a linear grid. The distribution of the grid points is chosen with a high density close to the interface. The grid is defined in terms of geometric series. The compositions of ferrite and austenite were taken according to the values determined via the APT characterization for the austenitic and martensitic matrices, respectively. In the martensitic matrix we detected a slight Mn depletion down to 10.3 at.%. This can be attributed to the formation of nanoprecipitates. Within martensite, a large number of lattice defects, particularly dislocations, enhance the atomic diffusion in this phase. Our previous TEM-based studies on this material [12,13] revealed that most of the nanoprecipitates were indeed associated with dislocations, which supports the assumption that the pipe mechanism may strongly assist diffusion within the martensite. In order to take into account the variation of composition in the ferrite due to the precipitation of particles, an average composition was used for the ferrite phase (see Fig. 5b). Martensite is not included as a separate phase in the thermodynamic and kinetic databases as the thermodynamic properties of martensite are very much the same as those of ferrite. Therefore, in the thermodynamic calculations, martensite is represented as ferrite. The kinetic parameters, however, may deviate between the two phases owing to the defect structure and distortion of the martensite. To date, no detailed information is available on the effect of these conditions on possible changes in the kinetic parameters between ferrite and martensite.

The size of the cell is fixed during the simulation (20 μm), whereas the interface between the two regions is mobile. The conditions at the moving interface are determined by the local equilibrium assumption, i.e. the chemical potentials of all diffusing elements assume the same value in ferrite and austenite. The value of the potentials is controlled by the mass balance condition. Diffusion of Mn, Mo, Ni, Si and Ti atoms was considered in the calculation. The simulation was performed for an aging temperature 450 °C and stopped at 180,000 s (50 h).

The composition profile of Mn between ferrite and austenite after an annealing time of 50 h at 450 °C is presented in Fig. 6. The interface has moved towards the ferrite side, leaving behind an austenite layer with drastically changed composition. This result is in qualitative agreement with the experimental data presented in Fig. 2b. However, the width of the predicted Mn-rich interfacial layer is too small and, correspondingly, the extent of the Mn depletion zone in ferrite is also relatively small. This discrepancy indicates

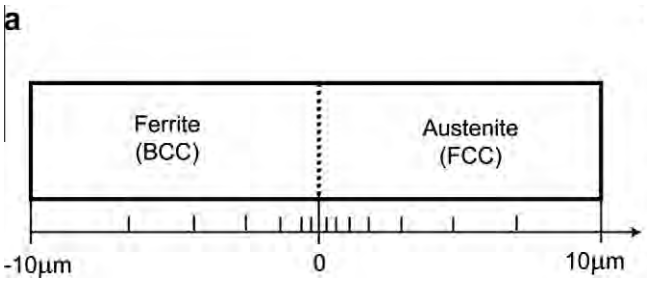

b

at. %	Ferrite	Austenite
Fe	85.79	83.88
Mn	10.7	12.2
Mo	0.6	0.6
Ni	1.66	2.0
Si	0.15	0.15
Ti	1.1	1.17

Fig. 5. (a) Linear cell model set-up with ferrite and austenite as used in the DICTRA simulation. The spatial grid is defined in terms of a geometric series with a high density of grid points close to the interface. (b) Composition of the austenite and ferrite phases used as input for the DICTRA simulation.

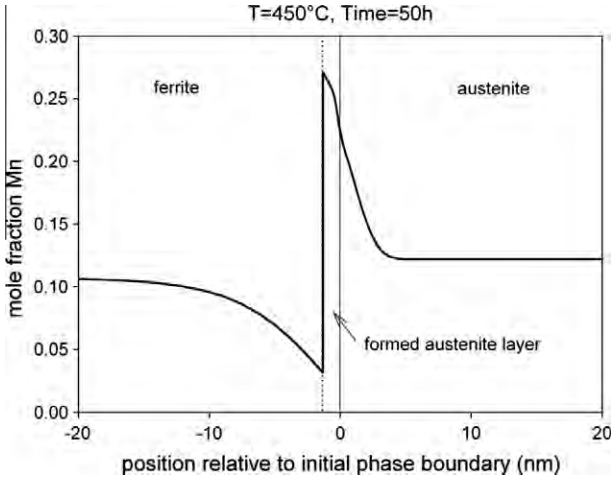

Fig. 6. DICTRA calculation of the Mn distribution at the martensite/austenite phase boundary. Martensite is thermodynamically and kinetically treated as ferrite. The calculation was done for 450 °C (aging temperature). The result is shown for the 180,000 s time step (50 h).

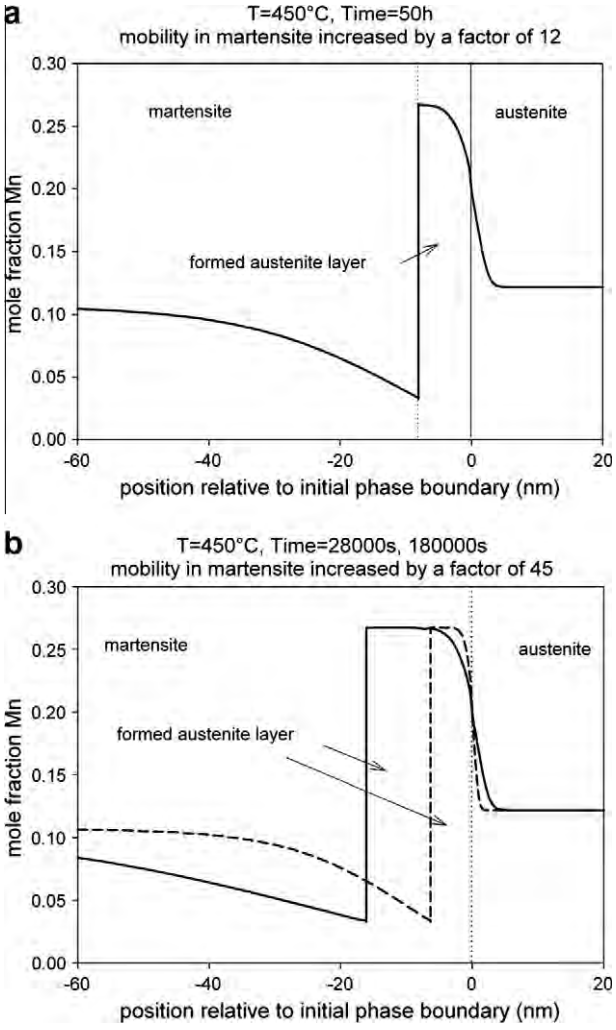

Fig. 7. DICTRA calculation of the Mn distribution at the martensite/austenite interface. Martensite is thermodynamically and kinetically treated as ferrite, but the mobility of the elements is increased by a factor of 12 (a) and 45 (b), respectively.

that the mobility of Mn in the martensitic matrix must be higher than it is in ferrite. Therefore, the simulations were repeated with increased mobilities of the elements in the ferrite. The results of the simulations with a factor 12 and 45, respectively, for the enhanced mobilities in martensite are shown in Fig. 7. The result in Fig. 7b (45 times enhanced Mn mobility in martensite) is in excellent agreement with the experimental results in Fig. 2b. This applies for the depletion profile of Mn in the martensite and also for the Mn-enriched interface zone.

In view of this good agreement, the profiles of the other elements should also be analyzed. Fig. 8a shows the composition profiles of some of the elements for a mobility factor of 45. Fig. 8b presents the predicted enrichment or depletion of the other elements, respectively, in the same way as for the experimental results. The partitioning tendencies of the elements are the same as observed in the experiment (compare Figs. 3a and b and 8a and b). The predicted enrichment of Mn and Ni and the depletion of Mo within the interfacial austenite layer are in good quantitative agreement with the experiments. For Ti and Si, the decrease is less pronounced in the simulation than in the experiment.

We estimated the mean diffusion paths of Mn atoms in both phases using the diffusion coefficients obtained for 450 °C using DICTRA (Mob2 database). The diffusion constant of Mn atoms in a bcc iron matrix (ferrite) was $D_{bcc} = 1.75 \times 10^{-22}\ m^2\ s^{-1}$ and in the fcc iron matrix $D_{fcc} = 5.86 \times 10^{-24}\ m^2\ s^{-1}$. The mean diffusion path λ of Mn atoms for an aging time of $t = 48$ h was calculated using the volume diffusion equation for cubic metals: $\lambda = (6tD)^{1/2}$. The mean diffusion path of Mn atoms in the bcc lattice was about 13 nm and in the fcc lattice only about 2.5 nm. Thus, the diffusion length of Mn in bcc is significantly larger than in the fcc lattice. When correcting the mobility of the atoms by a factor of 45, as explained above, the diffusion constant in ferrite (which can be then treated as martensite) is $7.56 \times 10^{-21}\ m^2\ s^{-1}$. For this case, the mean diffusion path of Mn in bcc increases from 13 to about 90 nm.

4. Discussion

4.1. Phase boundary motion with infinite interface mobility in the DICTRA approach

The global equilibrium calculated with Thermo-Calc (see Table 2) predicts a high amount of Mn in the retained austenite (27.6 at.%) and a low value (3 at.%) in ferrite. Hence, during aging a redistribution of Mn is expected. However, the global equilibrium only indicates the long term trends. The actual situation at the phase boundary is controlled by a local equilibrium.

It is not possible to visualize graphically equilibria in multicomponent systems. Therefore, the following discussion will be done considering only three components: Fe, Mn and Ni. Fig. 9 shows the ternary phase diagram at 450 °C. The initial compositions of martensite (filled

a

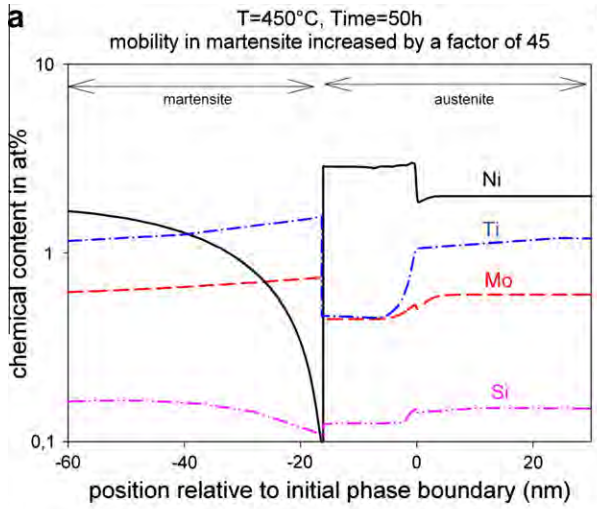

b

at. %	Interface layer	Global content	Enrichment within the layer, times
Mn	27.0	12.2	2.2
Ni	2.9	2.0	1.4

at. %	Interface layer	Global content	Depletion within the layer, times
Ti	0.4	1.17	2.9
Mo	0.4	0.60	1.5
Si	0.1	0.15	1.5

c

Element content (in at. %)	Mn	Ni	Ti	Mo	Si
at the new interface in martensite	3.13	0.11	1.56	0.68	0.17
at the new interface in austenite	27.7	5.2	0.49	0.46	0.12

Fig. 8. Results of DICTRA calculations. (a) Composition profiles of all elements included in the DICTRA simulation. (b) Quantitative characterization of the calculated profiles. (c) Element contents at the new interface between martensite and austenite at 450 °C for the given global composition.

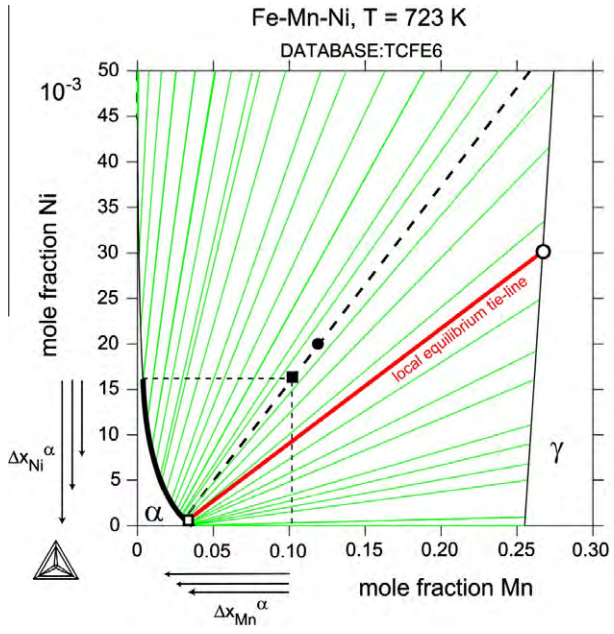

Fig. 9. Isothermal section of the Fe–Mn–Ni ternary system. The starting composition of austenite (filled circle) and martensite (filled square) are indicated. The global equilibrium tie-line is shown as a broken line. The bold part of the ferrite phase boundary indicates the range of possible local equilibrium tie-lines.

square) and austenite (filled circle) are within the two-phase region $\alpha + \gamma$. The global equilibrium tie-line is shown by a dotted line. The slope of the tie-lines indicates that at the austenite phase boundary the level of both Mn and Ni must be higher than in the matrix. Conversely, the level of Mn and Ni at the martensite boundary must be lower than in the matrix. The range of possible local equilibrium tie-lines is thus confined to those originating from Ni concentrations in martensite below the value in the α-matrix, i.e. $x_{\mathrm{Ni}}^{\alpha/\gamma} < x_{\mathrm{Ni}}^{\alpha}$. This composition range is marked in Fig. 9 by a bold phase boundary. The operating local equilibrium tie-line is defined by the fluxes of Ni and Mn. The interface displacement caused by these fluxes must be the same for every diffusing element. The resulting operating local tie-line is indicated in Fig. 9, showing the difference to that of global equilibrium.

Due to the low diffusivity in austenite, the fluxes lead to an interface displacement towards martensite. The layer of increased Mn is the result of the partitioning imposed by the local equilibrium tie-line during the formation of austenite. Epitaxial formation of this aging-induced austenite at the phase boundary of the existing austenite is likely.

The overall agreement between experiment and simulation is very good. There is a slight difference in the Mn composition at the martensite boundary though. The experiments yield a value of about 5–6 at.% Mn, while the simulation gives a value of 3 at.%. There are two possibilities to explain this difference. (i) It could be an effect of the resolution of the experiment. The transition from the low concentration at the martensite boundary to the very high concentration at the austenite interface occurs sharply. It is, therefore, plausible that close to this abrupt transition the Mn signal is slightly contaminated by the elevated Mn concentration, leading to a slightly increased composition close to the boundary. (ii) It could be due to the finite mobility of the interface. The local equilibrium approach implies that the interface can move freely. A finite mobility of the interface (see details in the next

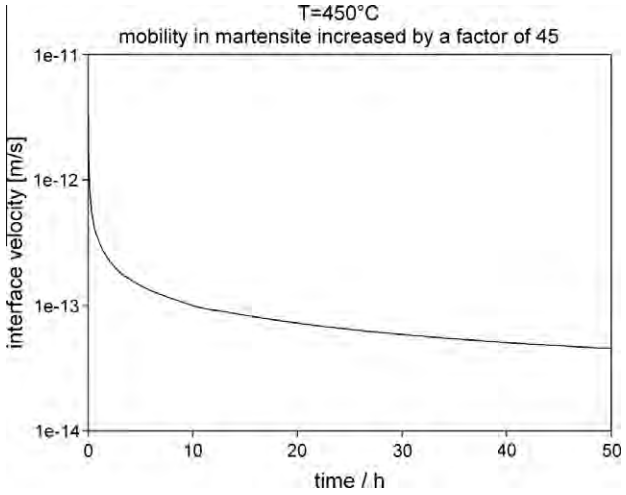

Fig. 10. Velocity of the interface α/γ as a function of time.

section) leads to a slower interface velocity than that given by the local equilibrium. Consequently, the boundary condition has to be adapted such that the mass balance is in accordance with the velocity. This effect, however, should become more relevant at rather high interface velocities. In the present case of low temperature the interface velocity is small (see Fig. 10). This velocity range is more than six orders of magnitude smaller than usual velocities occurring during the transition between austenite and ferrite at temperatures of about 700 °C or higher. We anticipate, therefore, that the finite interface mobility effect might play a second-order role in the current case as discussed in more detail in the next section.

4.2. Phase boundary motion with finite interface mobility in the mixed-mode approach

The simulation of a partitioning phase transformation with DICTRA as outlined above is based on the assumption that Mn diffusion is controlling the transformation kinetics. In a more generalized mixed-mode approach [33,34] the motion of the interface during the transformation is defined by its velocity, v, given by:

$$v = M\Delta G \tag{1}$$

where ΔG is the free-energy difference between the phases, acting as the driving force for transformation, and M is the interface mobility. In the purely diffusion-controlled transformation, such as discussed above, M is assumed to be infinite, which means that the interface instantaneously reacts to any deviation of the local concentration from equilibrium, thus restoring the local equilibrium. If M is finite, however, a certain balance is established between diffusion (in the case of Mn in α increasing the interface concentration, which increases the driving force) and interface motion (decreasing the Mn concentration at the interface, which decreases the driving force). For given values of M and the diffusivity D, the resulting value of the interface concentration, and thus of the driving force and the velocity, can be simulated for binary Fe–Mn on the basis of two assumptions [33]. The first one is that the driving force is proportional to the deviation from equilibrium:

$$\Delta G = \chi(x^{\alpha\gamma}_{\mathrm{Mn}}) - x^{\alpha}_{\mathrm{Mn}} \tag{2}$$

where the indices $\alpha\gamma$ denote the equilibrium concentration in the α-phase (martensite) in equilibrium with γ (austenite), and x^{α}_{Mn} is the Mn concentration in martensite at the interface. In the case of partitioning Mn, the proportionality factor χ is negative. The second assumption is that the diffusion in the parent martensitic α-phase leads to a concentration profile that can be described by an exponential function:

$$x_{\mathrm{Mn}} = x_0 + (x^{\alpha}_{\mathrm{Mn}} - x_0)\exp\left(-\frac{z}{z_0}\right) \tag{3}$$

with the spatial coordinate $z = 0$ at the interface. The width parameter z_0 follows from the values of M and D and the equilibrium and overall (x_0) concentrations [33]. Diffusion of Mn in the austenite is so slow that it can be neglected.

The experimental profile in Fig. 2b shows a Mn concentration in the α-phase at the interface of 5–6 at.%, which is slightly larger than the equilibrium value of 3.3 at.%. This would imply a deviation from local equilibrium. Using the value of the interface mobility M as an adaptable parameter and the same enhanced Mn diffusivity (factor 45) as used in the DICTRA simulations above, the Mn profile in the martensitic phase can be adequately reproduced (Fig. 11). The final profile ($t = 180{,}000$ s) is given, but also an intermediate stage, after 28,000 s. It is revealed that the deviation from equilibrium is larger in the earlier stages of the transformation. The calculations were conducted for a value of $\chi = -12.8$ kJ mol^{-1}, determined with Thermo-Calc, and a mobility of $M = 2 \times 10^{-21}$ m^4 J^{-1} s^{-1} at $T = 450$ °C. The simulated results reveal an excellent

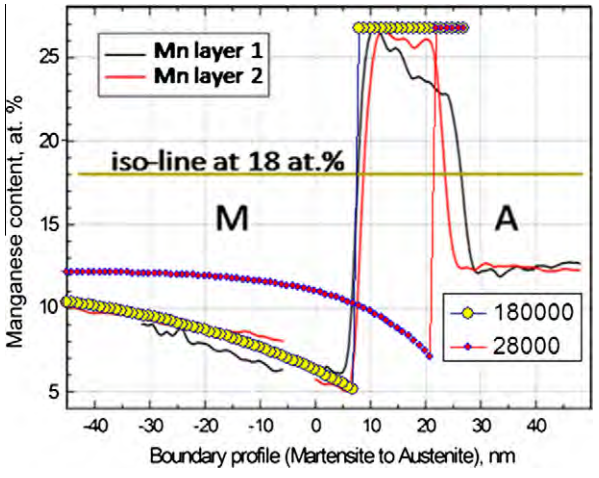

Fig. 11. Results of the mixed-mode predictions of the Mn profile across the austenite/martensite interfaces. In contrast to the DICTRA simulation, here the interface mobility is taken into account [33]. The mixed-mode simulation results for two aging times (red points: 28,000 s; yellow points: 180,000 s) are plotted together with the experimental data (red and black lines, see Fig. 2b).

agreement with the experiments (Fig. 11). The mobility value, however, is distinctly smaller than the mobility data for the standard $\gamma \rightarrow \alpha$ transformation around $T = 800\ ^{\circ}C$, when extrapolating with the commonly used activation energy for the mobility of 140 kJ mol^{-1}.

The mixed-mode approach uses the interface mobility as an adaptable parameter. This approach is particularly useful in cases where the transition is not fully controlled by diffusion. In such cases the local chemical equilibrium condition cannot be fulfilled. Instead, a difference in chemical potentials exists at the interface which provides the Gibbs energy required for the motion of the interface. If the interface mobility is known and does act as a limiting kinetic factor, it may play an essential role in the formation of the overall microstructure and hence should be included in the corresponding predictions.

4.3. Comparison and conclusions from the two simulation methods

The Mn distributions predicted by the calculations revealed diffusion of Mn from the ferritic phase towards the austenitic matrix and the accumulation of Mn at the interface between these two regions. The composition profiles obtained experimentally agree with the simulations provided that the mobilities of all alloying elements in martensite are increased compared to ferrite (by a factor of 45, Fig. 7b). This applies to both types of simulation approaches, i.e. DICTRA [30–32] and mixed-mode [33,34]. Such an enhanced diffusion in martensite can be attributed to a high defect concentration (e.g. misfit dislocations introduced through the transformation) in martensite. Pipe diffusion might therefore be one reason for this enhanced diffusion [12–14].

So far it is not clear whether the higher mobility is valid for martensite in general or if this holds only in the neighborhood of the phase boundary which may act as a source of vacancies and provides high local dislocation densities in its vicinity [35]. More experimental information is needed to elucidate this point.

5. Conclusions

We studied compositional variation phenomena on martensite/austenite interfaces in a maraging-TRIP steel. We placed particular attention on the partitioning of Mn at these interfaces using 3-D atom probe analysis in conjunction with Thermo-Calc, DICTRA and mixed-mode simulations (where the latter also includes the heterophase interface mobility). The local boundary condition at the interface leads to the diffusion of Mn in martensite towards austenite. The chemical gradients of Mn predicted by DICTRA at the phase boundary revealed a good quantitative correlation to the experimental findings. The diffusion behavior of other alloying elements such as Ni, Ti and Mo could also be reproduced in the dynamic simulation.

The partitioning at the martensite/austenite interface leads to the formation and growth of a new austenite layer on the existing retained austenite with drastically changed composition compared to the bulk. It is to be expected that such a layer will have an effect on the mechanical properties. In the present case, this layer is likely to be one of the microstructural changes during aging that might be responsible for the unexpected increase in ductility after the annealing treatment [12]. The other contribution for increasing the ductility stems from the tempering of the martensitic matrix during annealing and was reported elsewhere [36].

By using the advanced APT technique we gained deep insights into the chemical nature and dynamics of the martensite/austenite phase boundary during aging. The theory-assisted 3-D chemical analysis at the nanoscale provides significant enhancement of our understanding of partitioning affects and their relationship to phase transformation kinetics in multiphase steels.

Appendix A. Supplementary material

Supplementary data associated with this article can be found, in the online version, at doi:10.1016/j.actamat.2010.09.042.

References

[1] Patel JR, Cohen M. Acta Metall 1953;1:531.
[2] Bhadeshia HKDH, Edmonds DV. Metall Trans 1979;10A:895.
[3] Takahashi M, Bhadeshia HKDH. Mater Trans JIM 1991;32:689.
[4] Jacques PJ, Girault E, Catlin T, Geerlofs N, Kop T, van der Zwaag S, et al. Mater Sci Eng 1999;A273–275:475.
[5] De Meyer M, Vanderschueren D, De Cooman BC. ISIJ Int 1999;39:813.
[6] Traint S, Pichler A, Hauzenberger K, Stiaszny P, Werner E. Steel Res Int 2002;73:259.
[7] Zaefferer S, Ohlert J, Bleck W. Acta Mater 2004;52:2765.
[8] Brüx U, Frommeyer G, Grässel O, Meyer LW, Weise A. Steel Res 2002;73:294.
[9] Tomota Y, Strum M, Morris JW. Metall Mater Trans 1986;17A:537.
[10] Song R, Ponge D, Raabe D, Kaspar R. Acta Mater 2004;53:845.
[11] Song R, Ponge D, Raabe D. Acta Mater 2005;53:4881.
[12] Raabe D, Ponge D, Dmitrieva O, Sander B. Scripta Mater 2009;60:1141.
[13] Raabe D, Ponge D, Dmitrieva O, Sander B. Adv Eng Mater 2009;11(7):547.
[14] Ponge D, Millán J, Dmitrieva O, Sander B, Kostka A, Raabe D. In: Proc 2nd int symp steel sci (ISSS 2009). Kyoto: The Iron and Steel Institute of Japan; 2009. p. 121.
[15] Cerezo A, Godfrey TJ, Smith GDW. Rev Sci Instrum 1988;59:862.
[16] Blavette D, Deconihout B, Bostel A, Sarrau JM, Bouet M, Menand A. Rev Sci Instrum 1993;64:2911.
[17] Miller MK, Cerezo A, Hetherington MG, Smith GDW. Atom probe field ion microscopy. Oxford: Oxford University Press; 1996.
[18] Thuvander M, Miller MK, Stiller K. Mater Sci Eng A 1999;270:38.
[19] Miller MK. Atom probe tomography analysis at the atomic scale. New York: Kluwer Academic/Plenum; 2000.
[20] Kelly TF, Miller MK. Rev Sci Instrum 2007;78:031101.
[21] Seidman D. Annu Rev Mater Sci 2007;37:127.
[22] Miller MK, Forbes RG. Mater Charact 2009;60:461.
[23] Marquis EA, Miller MK, Blavette D, Ringer SP, Sudbrack CK, Smith GDW. MRS Bull 2009;34:725.

[24] Pereloma EV, Stohr RA, Miller MK, Ringer SP. Metall Mater Trans 2009;40A:3069.
[25] Sauvage X, Lefebvre W, Genevois C, Ohsaki S, Hono K. Scripta Mater 2009;60:1056.
[26] Al-Kassab T, Wollenberger H, Schmitz G, Kirchheim R. Tomography by atom probe. In: Rühle M, Ernst F, editors. High resolution imaging and spectroscopy of materials. Springer series in materials science, vol. 50. Berlin: Springer-Verlag; 2000.
[27] Choi P, da Silva M, Klement U, Al-Kassab T, Kirchheim R. Acta Mater 2005;53:4473.
[28] Thermo-Calc Users' Guide, Version R. Stockholm: Thermo-Calc Software AB and Foundation of Computational Thermodynamics; 1995–2006.
[29] Thermodynamic database TCFE6 – TCS Steels/Fe-Alloys Database, Version 6.2, Thermo-Calc Software, www.thermocalc.com.
[30] Borgenstam A, Engström A, Höglund L, Ågren J. J Phase Equilib 2000;21:269.
[31] Crusius S, Inden G, Knoop U, Höglund L, Ågren J. Z Metallk 1992;83:673.
[32] Franke P, Inden G. Z Metallk 1997;88:917.
[33] Bos C, Sietsma J. Scripta Mater 2007;57:1085.
[34] Sietsma J, van der Zwaag S. Acta Mater 2004;52:4143.
[35] Calcagnotto M, Ponge D, Raabe D. Mater Sci Eng A 2010;527:2738.
[36] Ponge D, Millán J, Dmitrieva O, Sander B, Kostka A, Raabe D. Proc 2nd int symp on steel science (ISSS 2009). Kyoto: The Iron and Steel Institute of Japan; 2009. p. 121.